

2016-01-01

Intrinsic And Metal-Doped Gallium Oxide Based High-Temperature Oxygen Sensors For Combustion Processes

Ernesto Javier Rubio

University of Texas at El Paso, ejrubio@miners.utep.edu

Follow this and additional works at: https://digitalcommons.utep.edu/open_etd

 Part of the [Materials Science and Engineering Commons](#), [Mechanics of Materials Commons](#), and the [Nanoscience and Nanotechnology Commons](#)

Recommended Citation

Rubio, Ernesto Javier, "Intrinsic And Metal-Doped Gallium Oxide Based High-Temperature Oxygen Sensors For Combustion Processes" (2016). *Open Access Theses & Dissertations*. 947.
https://digitalcommons.utep.edu/open_etd/947

This is brought to you for free and open access by DigitalCommons@UTEP. It has been accepted for inclusion in Open Access Theses & Dissertations by an authorized administrator of DigitalCommons@UTEP. For more information, please contact lweber@utep.edu.

INTRINSIC AND METAL-DOPED GALLIUM OXIDE BASED HIGH-
TEMPERATURE OXYGEN SENSORS FOR COMBUSTION
PROCESSES

ERNESTO JAVIER RUBIO

Doctoral Program in Environmental Science and Engineering

APPROVED:

Ramana V. Chintalapalle, Ph.D., Chair

Arturo Bronson, Ph.D.

Norman Love, Ph.D.

David Roberson, Ph.D.

Charles Ambler, Ph.D.
Dean of the Graduate School

Copyright ©

by

Ernesto Javier Rubio

2016

Dedicated to my Parents

INTRINSIC AND METAL-DOPED GALLIUM OXIDE BASED HIGH-
TEMPERATURE OXYGEN SENSORS FOR COMBUSTION
PROCESSES

by

ERNESTO JAVIER RUBIO, M.S.

DISSERTATION

Presented to the Faculty of the Graduate School of
The University of Texas at El Paso
in Partial Fulfillment
of the Requirements
for the Degree of
Doctor of Philosophy

Environmental Science and Engineering
THE UNIVERSITY OF TEXAS AT EL PASO

May 2016

Acknowledgements

I would like to thank my mentor, Dr. Ramana Chintalapalle, for his guidance, financial support, and his overall help throughout my academic years, especially during this doctoral research. He pushed me toward becoming better scholar, researcher, and person. I am very thankful for all his lessons and support that allowed me to complete this research.

I would like to thank Dr. Arturo Bronson (Mechanical Engineering), Dr. Norman Love (Mechanical Engineering), and Dr. David Roberson (Materials Science and Engineering), who agreed to be part of my doctoral committee and were willing to spend their valuable time to evaluate my dissertation research. Also, I am highly indebted to all of them for the feedback given from time to time.

I would like to thank my past and present team members at UTEP: Mr. Gustavo Martinez, Dr. Mirella Vargas, Mr. Sampath Kumar, Mr. Adbeel Moreno, Dr. Noor-A-Alam, Mr. Alejandro Miranda, and all others who have helped me in performing experiments and research insights.

I wish to express my sincere thanks to the Department of Energy (DoE) and National Science Foundation (NSF) for the financial support through research grants. Part of the research presented in this dissertation was supported by the DoE; however, the views and opinions expressed by the author(s) herein do not necessarily state or reflect those of the United States government or funding agency thereof.

Abstract

Currently, there is enormous interest in research, development and optimization of the combustion processes for energy harvesting. Recent statistical and economic analyses estimated that by improving the coal-based firing/combustion processes in the power plants, savings up to ~\$450-500 million yearly can be achieved. Advanced sensors and controls capable of withstanding extreme environments such as high temperatures, highly corrosive atmospheres, and high pressures are critical to such efficiency enhancement and cost savings. For instance, optimization of the combustion processes in power generation systems can be achieved by sensing, monitoring and control of oxygen, which is a measure of the completeness of the process and can lead to enhanced efficiency and reduced greenhouse gas emissions. However, despite the fact that there exists a very high demand for advanced sensors, the existing technologies suffer from poor ‘response and recovery times’ and ‘long-term stability.’

Motivated by the aforementioned technological challenges, the present work was focused on high-temperature (≥ 700 °C) oxygen sensors for application in power generation systems. The objective of the present work is to investigate nanostructured gallium oxide (Ga_2O_3) based sensors for oxygen sensing, where we propose to conduct in-depth exploration of the role of refractory metal (tungsten, W, in this case) doping into Ga_2O_3 to enhance the sensitivity, selectivity, stability (“3S” criteria) and reliability of such sensors while keeping cost economical. Tungsten (W) doped gallium oxide (Ga_2O_3) thin films were deposited via rf-magnetron co-sputtering of W-metal and Ga_2O_3 -ceramic targets. Films were produced by varying the sputtering power applied to the W-target in order to achieve variable W content into Ga_2O_3 films while substrate temperature was kept constant at 500 °C. Chemical composition, chemical valence states, microstructure and crystal structure of as-grown and post-annealed W-doped Ga_2O_3 films were evaluated as a function of W-content. The structural analyses indicate the formation of monoclinic β -phase Ga_2O_3 in as-grown W-doped Ga_2O_3 films for all W-content. Thermally induced secondary phase (W-oxide) formation was observed after the annealing process. Chemical analysis demonstrates the increasing W atomic

percentage in the films with increasing sputtering power, whereas the main metallic ionic species for the films are W^{6+} and Ga^{3+} . Evidence of W interdiffusion due to the annealing process is presented, and the mechanism of diffusion is discussed. Surface morphology of the films is also discussed, and the transition to mesoporous surface is observed after annealing. Finally, the oxygen sensor performance evaluation demonstrated that the W-incorporated Ga_2O_3 exhibits improved response time compared to intrinsic Ga_2O_3 based oxygen sensors.

Table of Contents

Acknowledgements.....	v
Abstract.....	vi
Table of Contents.....	viii
List of Tables	x
List of Figures.....	xi
Chapter 1: Introduction.....	1
1.1. Sensors and Principles	4
1.1.1. High Temperature Oxygen Sensors.....	6
1.1.2 Potentiometric Oxygen Sensors.....	7
1.1.3 Limiting Current Amperometric Oxygen Sensors.....	10
1.1.4 Metal Oxide Semiconductor (MOS) Oxygen Sensors.....	11
1.2 Gallium Oxide.....	16
Chapter 2: Motivation and Significance of the Proposed Project.....	21
2.1 Research Objectives and Statement of Proposed Work.....	21
2.1.1 Fabrication of Ga ₂ O ₃ Thin Films Based High Temperature Oxygen Sensors....	22
2.1.2 Optimization of Deposition Conditions.....	22
2.1.3 Develop a Structure-Electrical-Processing Conditions Relationship	23
2.1.4. Evaluate Ga ₂ O ₃ Based Thin Films for Oxygen Detection at High Temperatures.....	23
2.1.5 Investigate the Thermal Stability of Ga ₂ O ₃ Based Thin Films	24
Chapter 3: Literature Review.....	25
3.1 High Temperature YSZ Based Oxygen Sensors.....	25
3.2 High Temperature Metal Oxide Based Oxygen Sensors	26
3.3 Gallium Oxide High Temperature Oxygen Sensor Performance	32
Chapter 4: Materials and Methods.....	37
4.1 Materials	37
4.2 Substrates	38
4.3 RF- Sputtering Deposition System	39
4.4 Analytical Tools.....	42

4.4.1 Rutherford Backscattering Spectrometry (RBS)	42
4.4.2 X-Ray Photo Electron Spectroscopy (XPS)	44
4.4.3 X-Ray Diffraction (XRD)	45
4.4.4 Scanning Electron Microscopy	47
4.4.5. Nanoindentation	48
4.4.6. Spectrophotometer	50
4.4.7. Spectroscopy Ellipsometry	52
4.5 Thermal Stability.	54
4.6 High Temperature Oxygen Sensor Performance	55
Chapter 5: Results	58
5.1 Intrinsic Ga ₂ O ₃ Thin Films	58
5.2 Optical Properties W-doped Ga ₂ O ₃ films	66
5.3 Chemical Analysis W-doped Ga ₂ O ₃ films	70
5.4 Structural Analysis W-doped Ga ₂ O ₃ films	78
5.5 Thermal Stability W-doped Ga ₂ O ₃ films	81
5.6 Mechanical Properties.....	92
5.7 Oxygen Sensor Characteristic.....	94
Chapter 6: Discussion	102
Chapter 7: Conclusions	118
Chapter 8: Future Work and Outcomes	121
References.....	122
Curriculum Vitae	139

List of Tables

Table 3.1: List of samples and conditions of deposition	41
Table 5.1: Summary of the effect of growth temperature on the crystal structure, phase, grain size, and band gap of Ga ₂ O ₃ films.	66
Table 5.2: MSE values for Ellipsometry Spectroscopy simulated curves	69
Table 5.3: Atomic content of W-doped Ga ₂ O ₃ films obtained via RBS	73
Table 5.4: Comparison of atomic percentage of RBS and XPS results.....	84

List of Figures

Figure 1.1: Energy production by source in 2013: (a) worldwide (International Energy Agency 2015); (b) US generation (Administration 2015).....	1
Figure 1.2: Air to fuel ratio diagram for combustion processes	3
Figure 1.3: Schematic diagram showing the principle of a sensor	4
Figure 1.4: Schematic diagram of a potentiometric type oxygen sensor	9
Figure 1.5: Schematic diagram of a limiting current amperometric type oxygen sensor.	10
Figure 1.6: Schematic design of a MOS oxide semiconductor.....	14
Figure 1.7: Temperature range for MOS sensor mechanism of gas detection.....	15
Figure 1.8: β -Ga ₂ O ₃ monoclinic structure, constructed using CrystalMaker software	17
Figure 3.1: Nanocasting synthesis steps for mesoporous metal oxides sensors (Thorsten Wagner et al. 2013).	28
Figure 4.1: The Ga ₂ O ₃ (left) and W (right) targets employed in this project work.	37
Figure 4.2: Actual image of an employed pyrex glass substrate with integrated interdigital electrodes	38
Figure 4.3: RF-sputtering deposition system and sample holder with integrated heater and thermocouple.....	40
Figure 4.4: Co-sputtering deposition of W and Ga ₂ O ₃	42
Figure 4.5: RBS schematic diagram.	43
Figure 4.6: Kratos Axis Ultra X-ray Photoelectron Spectroscopy (XPS) from UCSB	45
Figure 4.7: Schematic diagram of X-ray-crystalline material interaction	46
Figure 4.8: Full view of the XRD system	47
Figure 4.9: Hitachi S-4800 SEM	48
Figure 4.10: Load vs Displacement curve representative for nanoindentation experiments (Tiwari 2012)	49
Figure 4.11: Cary 5000 UV–Vis–NIR double-beam spectrophotometer	51
Figure 4.12: The stack model of the Ga ₂ O ₃ based samples constructed for ellipsometry data analysis.....	53
Figure 4.13: Thermal-Cycling Furnace.....	55
Figure 4.14: Schematic diagram of functional MOS sensor and the oxygen interaction	56
Figure 4.15: Schematic diagram for the high temperature oxygen evaluation	57
Figure 5.1: XPS survey scans of representative Ga ₂ O ₃ films grown at different substrate temperatures. The survey scans obtained for films grown at RT (upper panel) and 500 C (lower panel) are shown (Ramana et al. 2014a).	59
Figure 5.2: XPS spectra of Ga 2p peaks, a) left image shows as-grown spectra, b) right figure shows the spectra after Ne sputtering was performed (Ramana et al. 2014a)	60
Figure 5.3: XPS spectra of O 1s peak, left image shows as-grown spectra, right figure shows the spectra after Ne sputtering was performed (Ramana et al. 2014a)	62
Figure 5.4: Peak fitting analysis of the O 1s core-level peak in as-grown Ga-oxide films fabricated at RT (Ramana et al. 2014a).	63
Figure 5.5: AFM images of sputter deposited Ga ₂ O ₃ films; (a) sample grown at 500 C, (b) sample grown at 600 C (Ramana et al. 2014a).	64
Figure 5.6: Electrical resistivity variation of Ga ₂ O ₃ films with Ts (Ramana et al. 2014a).	65
Figure 5.7: Transmittance spectra for Ga ₂ O ₃ based thin films.....	67

Figure 5.8: Band gap values of Ga ₂ O ₃ based thin films as a function of P _w ; insert figures shows (ahv) ² vs hv plots with integrated linear regression for band gap calculations.....	68
Figure 5.9: The spectral dependence of Ψ and Δ for Ga ₂ O ₃ films grown at various temperatures	69
Figure 5.10: Refractive index curves extracted from ellipsometry simulations	70
Figure 5.11: RBS spectra for as-grown Pure and W-doped Ga ₂ O ₃ films deposited via rf-sputtering, including SIMRA simulations curves	72
Figure 5.12: Thickness and W-concentration data as a function P _w use for rf-sputter deposition	73
Figure 5.13: XPS spectra for W-doped Ga ₂ O ₃ film deposited with P _w =50W at 500°C, as deposited.	74
Figure 5.14: a) (Top) Ga3d high resolution spectra; b) (bottom) W4f peaks from high resolution XPS spectra for W-doped Ga ₂ O ₃ films	76
Figure 5.15: O1s high resolution XPS spectra for W-doped Ga ₂ O ₃ films	78
Figure 5.16: GIXRD spectra for W-doped Ga ₂ O ₃ as-grown films	79
Figure 5.17: SEM micrographs for Pure and W-doped Ga ₂ O ₃ films as a function of P _w	80
Figure 5.18: SEM micrographs for Pure and W-doped Ga ₂ O ₃ films as a function of substrate temperature	81
Figure 5.19: RBS spectra and simulated curve for GWO films after annealing.....	83
Figure 5.20: Core XPS spectra from 600-5 eV for W-doped Ga ₂ O ₃ films as a function of P _w after annealing	85
Figure 5.21: a) High resolution Ga3d XPS peak after annealing; b) High resolution W4f XPS spectra after films annealing	86
Figure 5.22: High resolutions XPS scans for O1s peak for W-doped Ga ₂ O ₃ films as a function of P _w after the annealing process	87
Figure 5.23: GIXRD plot for after annealing Pure and W-incorporated Ga ₂ O ₃ films deposited via co-rf-sputtering	88
Figures 5.24: a) SEM micrographs for Pure and W-doped Ga ₂ O ₃ films as a function of P _w after annealing, b) AFM topography images for Pure and W-doped Ga ₂ O ₃ films after annealing	89
Figure 5.25: SEM micrographs of long period exposure to 900 °C for a) (top) Pure Ga ₂ O ₃ ; b) (middle) W-doped Ga ₂ O ₃ films deposited with P _w =50W at 500 °C; c) (bottom) W-doped Ga ₂ O ₃ films deposited with P _w =50W at 800 °C	92
Figure 5.26: Load and unload curve for Pure Ga ₂ O ₃ thin films versus indentation depth.	92
Figure 5.27: Hardness (left) and Elastic Modulus (right) values of Ga ₂ O ₃ based thin films as a function of tungsten sputtering power	93
Figure 5.28: Oxygen sensor response of in-line setup for Ga ₂ O ₃ based films deposited on Al ₂ O ₃	95
Figure 5.29: Arrhenius plot for Ga ₂ O ₃ based thin films as a function of W-sputtering power	96
Figure 5.30: Sensitivity and time response comparison of Ga ₂ O ₃ based sensors evaluated at 800 °C.	98
Figure 5.31: Oxygen sensor response for Ga ₂ O ₃ based sensor evaluated at cyclic inputs of P _{O2} at 800 °C	100
Figure 5.32: Log σ vs Log P _{O2} plots for m-value calculations for Ga ₂ O ₃ based films evaluated at a constant temperature of 800 °C	101

Figure 6.1: Behavioral diagram of intrinsic Ga ₂ O ₃ deposited as a function of substrate temperature (Kumar et al. 2013).....	105
Figure 6.2: Sputtering growth diagram presented by Thornton (Alfonso, Olaya, and Cubillos 2012)	111
Figure 6.3W-O phase diagram proposed by Schwenke (Schwenke 2001).....	114
Figure 6.4: XPS depth-profile of as-grown film vs annealed W-doped Ga ₂ O ₃ representative film.	116

Chapter 1: Introduction

Today's energy demand for industrial, commercial, transportation, and residential utilization has increased significantly in recent years. In this context, it should be recognized that a major part of the energy that the world consumes is derived from fossil fuels (see, Figure 1). However, utilization of fossil fuels for power generation involves a series of complex processes and phenomena. One of the most important things to mention relevant to the process of combustion, is the fact that it leads to different issues in terms of various pollutant byproducts (Figure 1.1) (International Energy Agency 2015). As illustrated in Figure 1, in the U.S. up to 2013, 82% of the total energy production was obtained through fossil fuels, where 27% corresponds to natural gas and 19% corresponds to the use of coal as the primary source. Using these fossil fuels for energy production is, however, of primary concern in the context of environmental pollution and health hazardous emissions. The combustion byproducts can be translated into harmful emissions to the environment, especially emissions such NO_x , CO , CO_2 , and SO_2 . These emissions can be controlled and reduced through, as well as the increment on the efficiency of the energy systems, the improvement of sensors and controls techniques in power plants (Spirig et al. 2007).

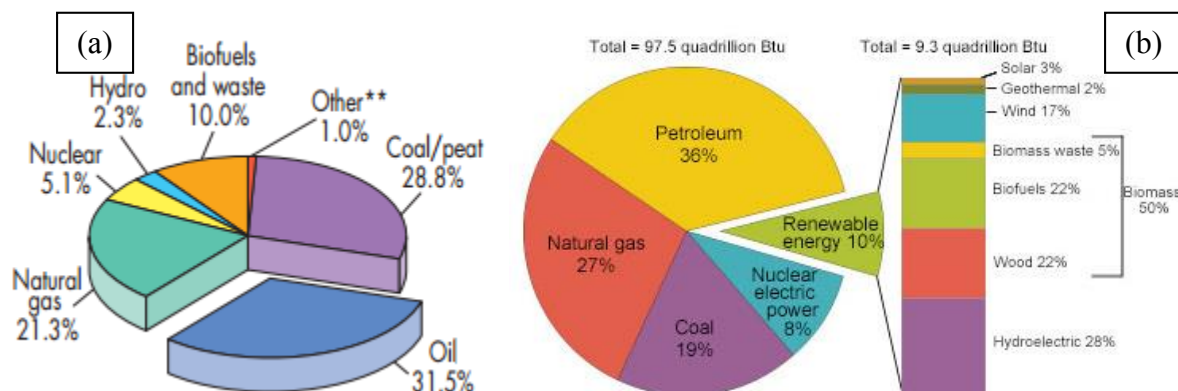


Figure 1.1: Energy production by source in 2013: (a) worldwide (International Energy Agency 2015); (b) US generation (Administration 2015).

Optimization of the combustion processes can enhance the efficiency, and significantly diminish the greenhouse gas emissions while reducing the ‘energy cost’ to the final user. For instance, recent statistical and economic analyses estimated that by improving the coal-based firing/combustion processes in the power plants, companies and manufacturers could achieve savings up to \$409 million yearly (Spirig et al. 2007), although the current estimates span the range of \$450-500 millions. However, in order to optimize the combustion process for energy harvesting, precise estimation, detection and monitoring of the byproducts must be achieved. From all the products emitted from a combustion process, the three main components that must be given a serious consideration for detection and monitoring are the following:

- O₂ & CO: The concentration of these gases provide a measure of the completeness of the combustion process
- NO_x: This gas concentration measures the main controllable pollutant from the combustion process (Romanosky, Dunst, and Dutta 2008).

Due to the need to detect each one of these gases accurately, energy science and engineering researchers have opted for using arrays of gas sensors to improve the performance of the energy systems. In the particular case of natural gas combustion, the values of CO at ideal combustion are reduced to tens of ppm, and detection of oxygen plays a very important role; however, when the excess of natural gas is introduced, the amount of CO rises, and its detection becomes important (Maximilian Fleischer 2008). Nevertheless, the detection of these gases for combustion processes require systems capable of withstanding extreme environments. According to the U.S. Department of energy, novel technologies based on coal-firing and combustion turbines work on thermal loads in the range of 1000 °C to 1600 °C (Romanosky and Maley 2013). In a similar fashion, the reduction of automotive emissions could be achieved by placing the

monitoring sensor closer to the exhaust manifold where temperatures are capable of reach 1000 °C (Candel and Docquier 2002).

Figure 1.2 shows a diagram where the different fuel to air ratio that can be presented in a combustion process, where we can see that under the optimum conditions, we could minimize the production of pollutants. When there is no sensor feedback is presented, we could be running our process in either fuel or air rich range. Running under fuel rich condition could cause not only environmental issues, but safety issues as well, due to the numerous amount of unburned fuel that could reignite inside the exhaust system. On the other hand, running the combustion process on the air rich range will generate higher amounts of NO_x (NO, NO₂) products that are the main contributors of acidic rain (Yokogawa 2008).

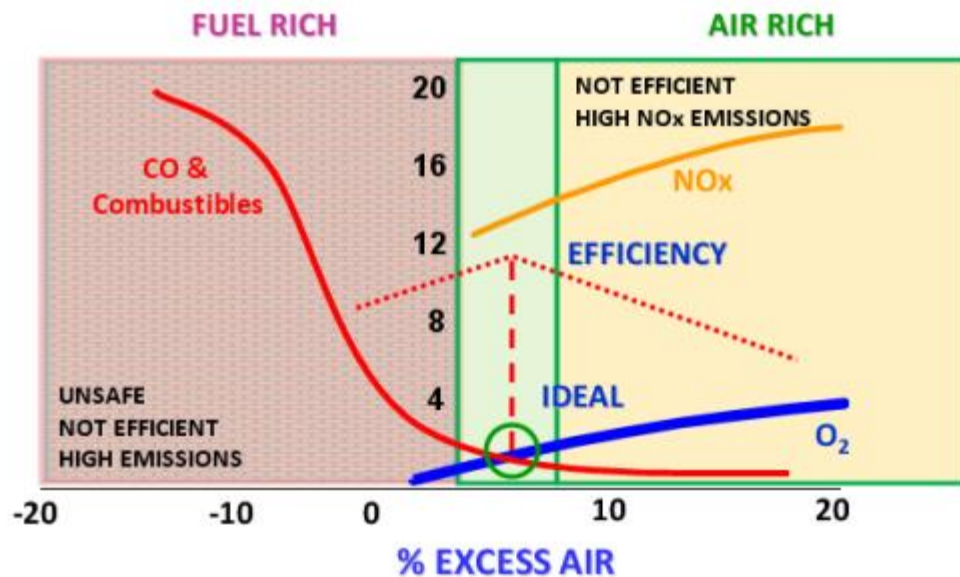


Figure 1.2: Air to fuel ratio diagram for combustion processes (Yokogawa 2008)

The ongoing research to improve the efficiency and to generate a more sustainable energy portfolio including fossil fuels, has moved researchers to not only work in physical sensor, but also on the placing of the sensing devices. Complex algorithms that allow a higher control of the

emissions presented in a combustion process, is one of the mechanisms that is under review (Han et al. 2013). Nevertheless, the main focus of this project is related to the physical improvement of the sensor; for that reason following sections are intended to provide some general background information on the sensors and their operation.

1.1. SENSORS AND PRINCIPLES

The word “sensor” has its origins in the Latin word “Sentire” which means to perceive or to be sensitive (Arregui 2009). A sensor is an electronic measurement device, which utilizes chemical or biological reactions (depending upon whether it is a chemical or biological sensor) to detect and quantify a specific analyte. The operational principle of a chemical/biological sensor is illustrated in Figure 1.3. The chemical detection is based on the principle that the changes in the atmosphere alter the material properties of sensor in a characteristic way. A sensor can be best defined or characterized in terms of the following:

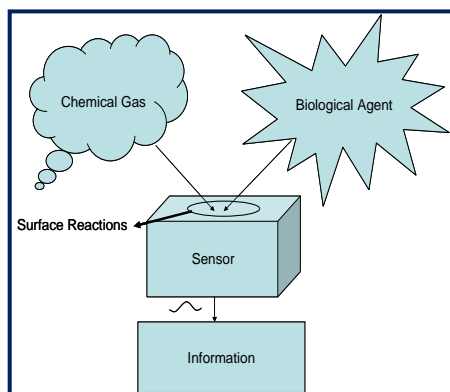


Figure 1.3: Schematic diagram showing the principle of a sensor

- **Mechanism:** which is responsible for detection or sensing ability,
- **Sensitivity:** is a change of measured reading when the analyte is introduced (Umar et al. 2010).

- **Selectivity:** refers to ability of a sensor to respond selectively to a group of analytes or even only to a single analyte (Umar et al. 2010).
- **Stability:** is the capacity of a sensor to show reproducibility in the results for a certain period of time (Umar et al. 2010).

Sensitivity, selectivity, stability of a sensor are usually called the “3S” criteria.

- **Response Time:** It is the transient response of the sensor when it experiences a change in the property measured (Umar et al. 2010).
- **Operating Temperature:** the specific temperature or range of temperature that the sensor can function effectively and safely.
- **Life Time:** is the period that a sensor can survive without failure or damage or degradation in functionality.

There are many more requirements that a sensor needs to fulfill, such as size, power consumption, and cost (Umar et al. 2010). Also, in the case of high temperature sensors, the material is required to tolerate elevated temperatures ($>700\text{ }^{\circ}\text{C}$), high pressure, and highly corrosive environments (Y. X. Liu et al. 2014). Furthermore, in order to mitigate the requirements of high temperature sensors, and more specific for power generation purposes, researchers have been working on different technologies, and manipulation of materials properties for a better understanding and control of the systems. Among new technologies: fiber optics, sensors arrays, 1D structures, and the integration of nanotechnology are under exploration (Romanosky and Maley 2013), especially for utilization in power generation systems.

The coupling of nano-scale science with existing sensorial techniques has open the doors to new scales in accuracy and improvements. Among the advantages of the junction with nanotechnology are the small device sizes, integration, miniaturization, low power consumption,

inexpensive, capability for high production volume at low cost; high efficiency, controlled transduction mechanisms at the nanoscale tightening up homogeneity and uniformity; long-term stability, material properties improved, improved sensor dynamic, and minimized time required for sensor response (Arregui 2009). Furthermore, the capabilities of nano-scale materials to be tuned by varying fabrication parameters and methodologies to achieve optimal functional properties of the material is one of the more prominent advantages that the sensor industry is exploiting to achieve higher efficiency on the sensed processes.

Our topic and particular work is towards designing and developing reliable nanostructured oxygen sensors for utilization under extreme environments. A brief introduction on high-temperature oxygen sensors is presented below.

1.1.1. High Temperature Oxygen Sensors

An oxygen sensor is an electronic device, which measures the oxygen concentration under certain conditions depending the specific or targeted application. Oxygen sensors capable of operating at harsh environments, which experience extreme conditions in terms of temperature, pressure and corrosive atmosphere, are needed in many industrial applications. Industrial oxygen sensors are used for combustion monitoring and control in a great variety of applications comprising energy consuming industries, such as iron and steel, electric power, oil and petrochemical, ceramics, pulp and paper, and textiles as well as various combustion requirements like boilers or incinerators. Most importantly, the oxygen sensor is the key component in oxy-fuel combustors and automobiles (Umar et al. 2010). The functionality and need for oxygen sensors for extreme environment applications can be best understood by considering the case of automobiles since various types of sensors initially developed for the combustion efficiency

control in the automotive industry have been adapted for industrial furnaces, boilers, gas turbines and oxy-fuel combustion based power generation systems technology.

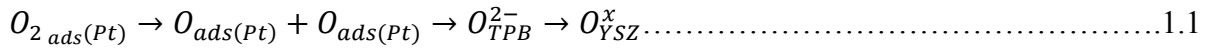
The first commercial oxygen sensor was introduced by Bosch in 1976 in order to control the air to fuel ratio of the exhaust of a car engine. These sensors did not incorporate any internal heater, and they depended on the temperature of the combustion products to reach operational conditions. From that point researchers have worked to improve materials to optimize the combustion processes and to have a better detection of the oxygen as encountered in many systems (Ramamoorthy, Dutta, and Akbar 2003). There are three main types of high-temperature oxygen sensors: (1) potentiometric, (2) limiting current amperometric, and (3) metal oxide based sensors. The first two require the use of solid electrolytes, whereas metal oxide semiconductors depend on the change in electrical properties of the active layer which can be a thin or thick film. The first written evidence that a semiconductor was used as an oxygen sensors was published in 1956, in the Diploma Thesis by Erlangen under the mentoring of Mollwo and Heiland, and the title of the thesis was “Oxygen detection in gases changes in the conductivity of a semiconductor (ZnO)” (Carpenter, Mathur, and Kolmakov 2003). The following subsections will explain the mechanism of oxygen sensing as well as the common materials for each of the main types of oxygen sensors.

1.1.2 Potentiometric Oxygen Sensors

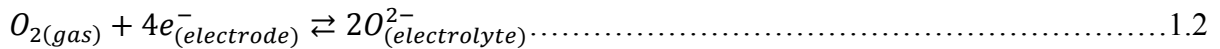
This type of sensor requires the use of oxygen ion conducting materials as solid electrolytes, and the most common material employed is Yttria-Stabilized Zirconia (YSZ) due to its high ion conductivity produced by the incorporation of yttrium into the zirconia lattice which causes oxygen vacancies. When 6 to 12 mol% of yttria is incorporated, zirconia cubic phase is stabilized which is the preferred phase for ionic conductivity at high temperatures (Ramamoorthy, Ramasamy, and Sundararaman 1999). YSZ is also preferred as the high temperature oxygen sensor due to its other

properties such as crystal structure, oxygen stoichiometry, and mechanical properties which are preserved up to 2500 °C (Ramamoorthy, Dutta, and Akbar 2003).

The sensing mechanism of potentiometric oxygen sensor depends on the chemical and electrical potential which is schematically presented in Figure 1.4. When YSZ sensor is exposed to the test gas, the oxygen molecules presented in the gas get adsorbed by the electrode, commonly made out of porous platinum (Pt), and dissociated into atomic oxygen. Afterwards, the adsorbed atoms diffuse into the boundary formed by the Pt electrode, the electrolyte (YSZ) and the gas which is known as the Triple Phase Boundary (TPB). It is at the TPB where the electron transfer takes place from the electrode to the adsorbed atomic oxygen forming O^{2-} ions. The process can be explained as follows using Kröger-Vink notation (Ramamoorthy, Dutta, and Akbar 2003):



The requirements in the designing of potentiometric sensors are the following: The electrode material must be a good catalyst for oxygen reduction and oxidation, and at the same time it should show high porosity to allow triple phase boundary. In the case of the electrolyte, it needs to show high ionic conductivity at the desired operational temperature. When oxygen is present at the electrode-electrolyte interface, it defines a value for the oxygen activity and the Fermi level (E_F) is controlled at the interface by the oxygen electron equilibrium as per the following equations (Ramamoorthy, Dutta, and Akbar 2003):



$$E_F = \frac{1}{4}(\mu_{O^2} - \mu_{O_2}) \dots \dots \dots 1.3$$

where μ is the chemical potential. In the particular case of YSZ electrolytes, which show high ion conductivity and high oxygen vacancies, the chemical potential for the oxygen ions inside the

electrolyte in the same. When different partial pressure of oxygen are presented, the Fermi level can be expressed as follows:

$$E_F = \frac{1}{4} (\mu'_{O_2} - \mu''_{O_2}) = \frac{kT}{4e} \ln\left(\frac{P'_{O_2}}{P''_{O_2}}\right) \dots\dots\dots 1.4$$

where k is the Boltzmann constant, T is the absolute temperature, and e is the electron charge.

Furthermore, the electrical potential produce between the two electrodes is obtained by Nernst equation of electrochemical cells, with the following equation:

$$emf = \frac{RT}{4F} \ln\left(\frac{P'_{O_2}}{P''_{O_2}}\right) \dots\dots\dots 1.5$$

where F is the Faraday constant, and R is the universal gas constant. The sensitivity of the sensors is given by the first part of the equation $RT/4F$, and depends only on the temperature (Ramamoorthy, Dutta, and Akbar 2003).

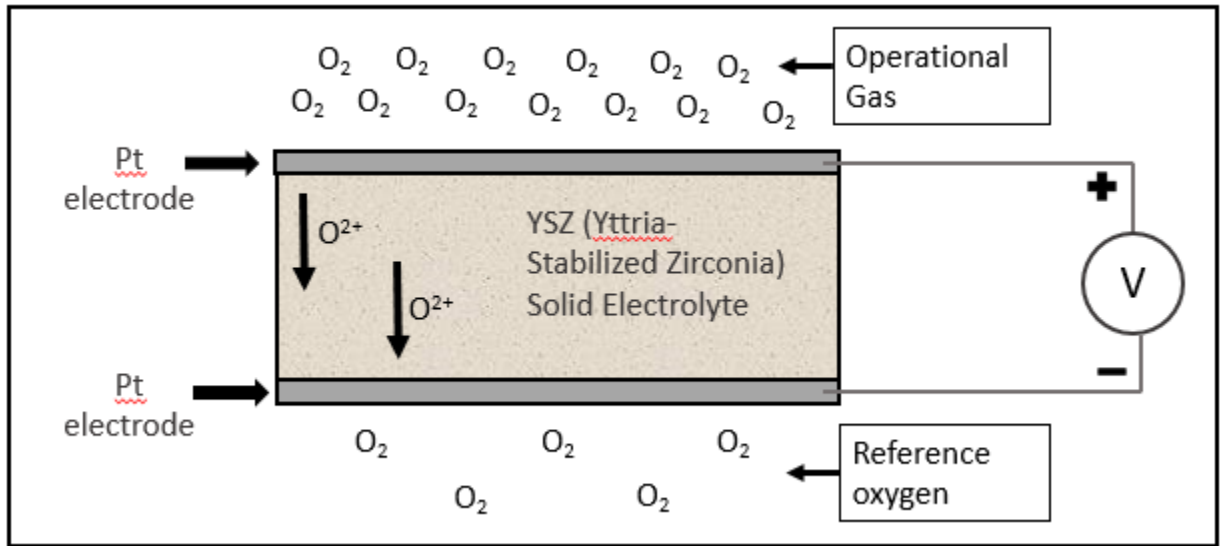


Figure 1.4: Schematic diagram of a potentiometric type oxygen sensor.

The main disadvantages of this type of sensors include a relatively weak dependence on partial pressure, and the necessity for a high-temperature seal to isolate the unknown from the reference gas (Kim, Rothschild, and Tuller 2013).

1.1.3 Limiting Current Amperometric Oxygen Sensors

For this type of sensor, oxygen is pumped from one side of the electrolyte to the other by applying an external voltage to the system. The resulting ionic current flowing through the electrolyte is proportional to the oxygen concentration. Due to the high magnitude of diffusion coefficient for oxygen in the gas state the ionic current is increased through the electrolyte with the applied voltage until breakdown occurs. In order to avoid breakdown occurring, a diffusion barrier is introduced to the head of the cathode, this diffusion barrier can be a small aperture or a porous material, all of the features included in amperometric sensors are shown in Figure 1.5 (Ramamoorthy, Dutta, and Akbar 2003).

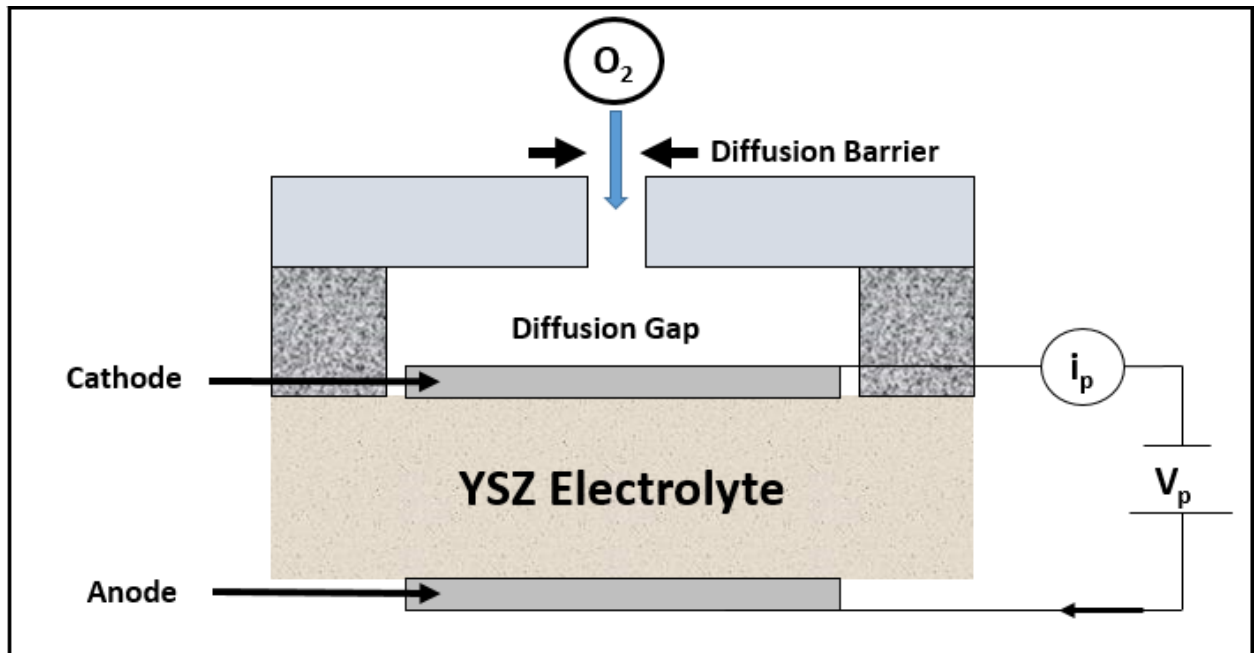


Figure 1.5: Schematic diagram of a limiting current amperometric type oxygen sensor.

The sensing mechanism of this system depends on the diffusion of oxygen that can be either bulk or Knudsen diffusion depending on the dimension of the aperture, but the I-V characteristics are different depending on the type of diffusion occurring, and hence the limiting current is a

function of the geometry of the diffusion barrier (Ramamoorthy, Dutta, and Akbar 2003). Previous studies have demonstrated that for bulk diffusion the limiting current depends on the oxygen concentration by $-\ln(1-C_{O_2})$, and linearly in the case of Knudsen diffusion (Usui 1989; Usui et al. 1987). For the linear dependency, the diffusion current of molecular oxygen dN_{O_2}/dt depends on the concentration gradient of oxygen dC_{O_2}/dx , the effective diffusion cross section Q , and the diffusion coefficient for oxygen D_{O_2} .

$$\frac{dN_{O_2}}{dt} = D_{O_2} Q \frac{dC_{O_2}}{dx} \dots\dots\dots 1.6$$

And the pumping ionic current flowing through the electrolyte follows Faraday's law:

$$i_p = 4F \frac{dN_{O_2}}{dt} \dots\dots\dots 1.7$$

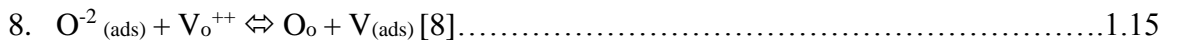
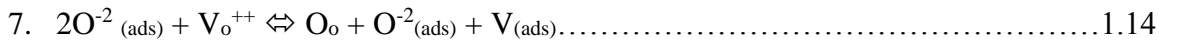
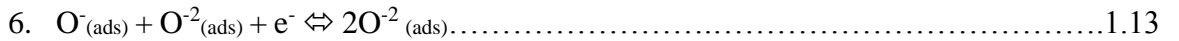
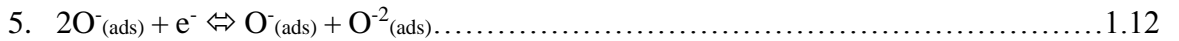
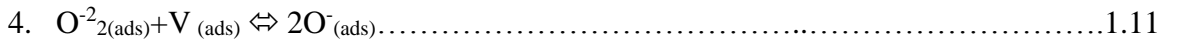
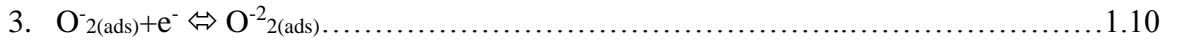
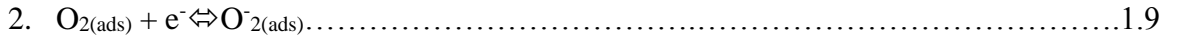
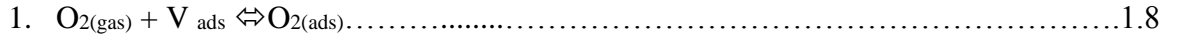
As the applied V_p is increased, the current also increases until the point where the oxygen pressure close to the cathode-electrolyte interface reaches a near zero value. After that, the current saturates depending on the molecular current of the oxygen flow along the diffusion barrier; once this happens, i_p is directly proportional to the oxygen concentration as a linear function (Ramamoorthy, Dutta, and Akbar 2003).

Some of the disadvantages encountered in these sensors is the limiting capabilities of working in environments where the air to fuel ratio (λ) has a value equal or smaller than 1, when the levels of fuel are higher than those for air in the called rich combustion (Ramamoorthy, Dutta, and Akbar 2003). Also, the limiting current depends on the morphology and catalytic activity of the electrodes, which changes after a certain period of operation (Kim, Rothschild, and Tuller 2013).

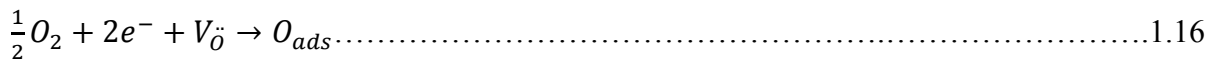
1.1.4 Metal Oxide Semiconductor (MOS) Oxygen Sensors

This type of sensor uses the metal oxide semiconductor to vary their electrical properties in the presence of a gas species in the atmosphere. MOS sensors can be miniaturized, and incorporated into MEM technologies which provides an advantage (Ramamoorthy, Dutta, and Akbar 2003).

The sensing mechanism of the MOS sensors relay on the non-stoichiometric nature of semiconductor metal oxides, where oxygen vacancies, metal interstitial, and metal vacancies are presented inside the material, producing oxygen defiance inside the lattice. When the materials are exposed to high temperatures $>700\text{ }^{\circ}\text{C}$, the already mentioned oxygen vacancies can suffer oxygen diffusion from inside the lattice towards the surface, or from the surrounding environment into the lattice, from here we can express basic equations between oxygen molecules at gas phase O_2^g , and the oxygen vacancies inside the material V_O (Kim, Rothschild, and Tuller 2013).



The 8 steps where 4 electrons are necessary to complete the process, can be summarized in the following half reaction using Kröger-Vink notation:



At the same time we need to consider that the behavior of the sensitivity for the shift in conductivity for a MOS materials is proportional to the oxygen partial pressure, and it is governed by the following equation:

$$\sigma = A * \exp[-E_A/kT] P_{\text{O}_2}^{1/m} \dots\dots\dots 1.17$$

where σ is conductivity, E_A represents the activation energy of the material, P_{O_2} is the partial pressure of oxygen, k is the Boltzmann coefficient, T is temperature, and $1/m$ represents the sensitivity of the material, and its value depends on the dominating defects involved in the reaction, and its sign depends on the type of semiconductor (n or p type) (Ramamoorthy, Dutta, and Akbar 2003). Figure 1.6 shows how a MOS sensor is composed, where the insulator substrate is used to avoid any leak current, the employment of interdigital electros, and the active MOS layer on top which enables the oxygen sensing properties that can be deposited as a thin or thick film. Most of the MOS sensors possess an integrated back heater to maintain steady temperature throughout the sensing process.

The list of materials investigated for oxygen sensing purposes is very lengthy; however, TiO_2 is the most studied semiconductor for oxygen sensing (Ramamoorthy, Dutta, and Akbar 2003; Xu, Zhou, and Sorensen 2000). Materials such ZnO , SnO_2 , WO_3 have being investigated, but their operational temperature reduce the capabilities of these materials (Bene et al. 2001). There are only a few simple binary metal oxides, Ga_2O_3 , CeO_2 and TiO_2 which are capable of maintaining their micro-morphology and chemical structure at temperatures higher than $800\text{ }^{\circ}C$ (Y. X. Liu et al. 2014). Furthermore, more complex oxide such $SrTiO_3$ perovskite type and $BaFe_{1-x}Ta_xO_{3-\delta}$ have shown capabilities to detect oxygen at low or high temperatures due to its near $\sim 0\text{ eV}$ activation energy (Y. X. Liu et al. 2014). Nevertheless, different parameters should be considered before choosing a Metal Oxide as sensing layer, among those properties the followings are important to mention: band gap, oxygen diffusion coefficient, catalytic activity, conductivity, thermodynamic stability, electronic structure, and chemical activity. In the case of high temperature metal oxide sensors, some of these properties should be considered; for example, in the case of the band gap, the temperature of operational should be proportional to band gap value (Korotcenkov 2007). In

terms of electronic structure, metal oxide with d^0 or d^{10} orbitals are preferred, in the case of d^n orbitals, they are not well suited due to the lower energy required to change to d^{n+1} or d^{n-1} (Wang et al. 2010). The thermal stability of the films is a very important aspect to consider, particularly if the sensors are going to be tested at high temperatures. Materials with high enthalpy of formation, and high melting point are characterized for their high thermal stability; however, the thermal program reduction (TPR) temperature, which indicated at what temperature metal oxide begin to reduce under a hydrogen rich environment, should be higher to avoid any interaction while sensor is operational (Korotcenkov 2007)

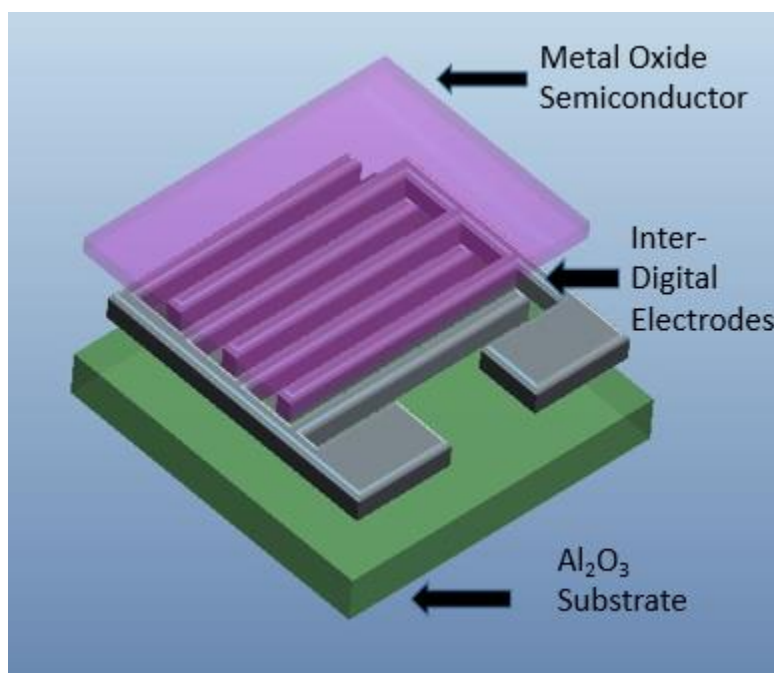


Figure 1.6: Schematic design of a MOS oxide semiconductor.

The mechanism of gas detection is highly dependent on the operational temperature and Figure 1.7 shows the schematic diagram where the different temperature ranges are identified. At low temperature (RT-200 °C), the dominant mechanism of gas detection is through surface reaction (Physisorption) of the metal oxide where there is no charge exchange involved. At intermediate temperature (300°C-500°C), chemisorption is the dominant phenomena where the incoming

oxygen ions interact with the surface of the sensing layer causing a band bending, and generating a depletion layer which in films with high surface to volume ratio causes an overall effect on the bulk conductivity of the material. The final range is considered the high temperature range (> 700 °C) where the balance between environmental oxygen and the bulk composition oxygen is achieved, in this case oxygen incorporation to the lattice is the main mechanism (Korotcenkov 2007; Kim, Rothschild, and Tuller 2013). At temperature > 700 °C the thermal energy is high enough to overcome kinetic barriers for oxygen exchange, oxygen interacts with bulk defects affecting the carrier concentration and changing the conductivity of the material (Kim, Rothschild, and Tuller 2013). It is important to mention that regardless the temperature, the borders on where each mechanism is controlling the process are not fixed, and they vary depending on the type of metal oxide that is employed (Korotcenkov 2007). Nevertheless, the time response of the sensors is dependent on two factors: surface reaction and diffusion (Gerblinger, Lampe, and Meixner 1995), but at elevated temperatures oxygen diffusion is the limiting step of the process (Korotcenkov 2007).

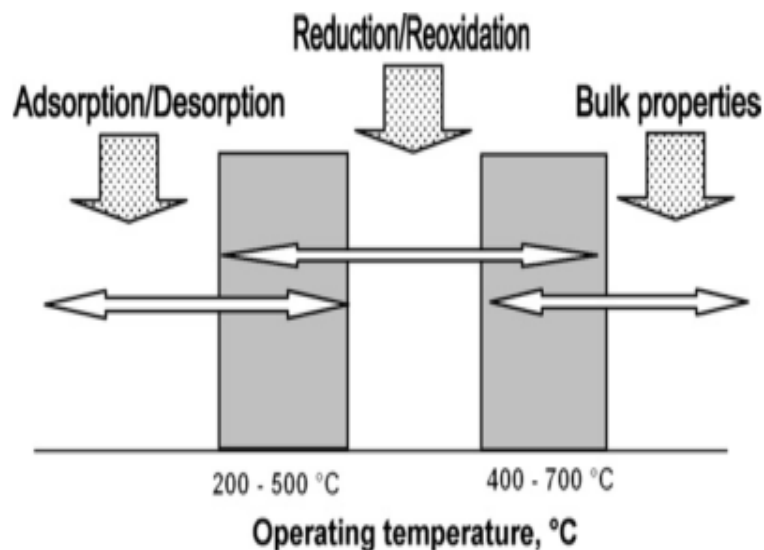


Figure 1.7: Temperature range for MOS sensor mechanism of gas detection.

In this particular work, the use of MOS sensors will be discussed, more specifically the use of Ga_2O_3 to use as an oxygen sensor working within the high temperature range. Nevertheless, it is important to develop on the diffusion process which dominated the time response of sensors at temperatures $>700^\circ\text{C}$. Once the surface reaction takes place, the adsorbed oxygen molecules will dissociate into O^- ions, which is the dominant ion specie at $>700^\circ\text{C}$ (Josepovits et al. 1998), and will interact with bulk defects of the material until balanced is achieved. Depending on the surface characteristics of the film the oxygen could diffuse via surface diffusion or Knudsen diffusion depending on the pore size. According to the IUPAC pore size classification, if the pore size is $>2\text{ nm}$ the material is considered microporous and surface diffusion is the ruling mechanism, and from 2 nm to 50 nm the material can be called mesoporous where Knudsen diffusion controls the process (Kärger, Ruthven, and Theodorou 2012; Roque-Malherbe 2007).

1.2 GALLIUM OXIDE

Gallium oxide (Ga_2O_3) is a wide band gap semiconductor. Ga_2O_3 is attractive for several different applications such as photoresistors, photo-diodes, UV-transparent conductive oxides, luminescent phosphors, electronic switches, and gas sensors (Onuma et al. 2013; X. Z. Liu et al. 2016; Petitmangin et al. 2013; Janowitz et al. 2011; Bene et al. 2001). Ga_2O_3 exhibits five polymorphs (Roy, Hill, and Osborn 1952); α , β , γ , δ , and ϵ , where β shows a monoclinic structure under normal conditions, α shows corundum structure, whereas δ is a bixbyite structure. The γ polymorph is not deeply investigated, but is known that it shows spinel structure with Ga-deficient defects; ϵ appears when δ - Ga_2O_3 is heated to 500°C , but the crystal structure was not determined (Yoshioka et al. 2007). From the five polymorphs, β -phase exhibits the highest thermal and chemical stability with crystal structure as presented in Figure 8. β -phase can be achieved by any of the different phases by heating the material up to 870°C (Maximilian Fleischer et al. 1997). Ga_2O_3

band gap value has been found to be $\sim 5\text{eV}$ (Fleischer and Meixner 1993; Hao and Cocivera 2002; Schubert et al. 2015), previous studies demonstrated that at 800°C Ga_2O_3 shows values of carrier concentration “ n ” = $8 \times 10^{13}/\text{cm}^3$, and a mobility of $\mu = 5 \text{ cm}^2/\text{Vs}$ (M. Fleischer and Meixner 1993).

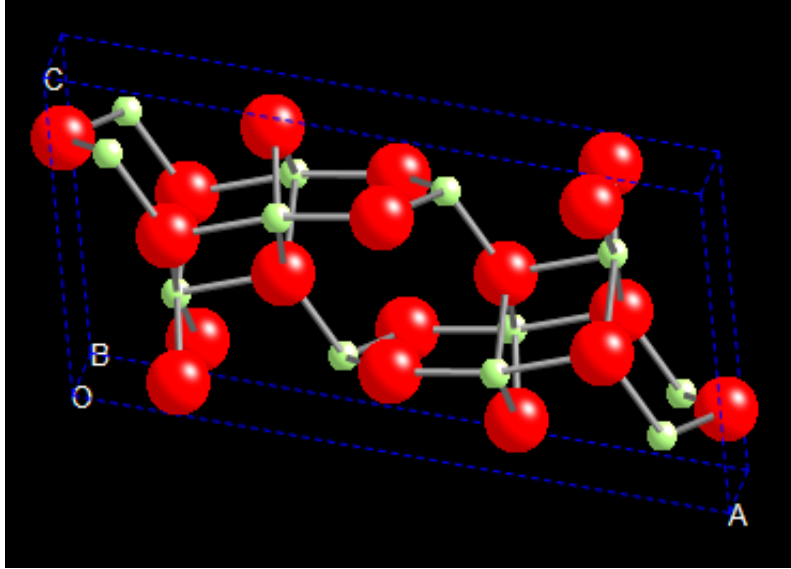


Figure 1.8: $\beta\text{-Ga}_2\text{O}_3$ monoclinic structure, constructed using CrystalMaker software

The $\beta\text{-Ga}_2\text{O}_3$ shows a base-centered monoclinic structure (space group $C_{2/m}$) with a melting temperature of 1780°C (Bartic, Baban, et al. 2007; Litimein et al. 2009; Kumar et al. 2013). The β -phase shows a distorted cubic packing arrangement for its oxygen ions, and a distorted octahedral and tetrahedral arrangement for the gallium ions. The lattice parameter for $\beta\text{-Ga}_2\text{O}_3$ are the following: $a=12.2140\text{\AA}$, $b=3.0371\text{\AA}$, $c=5.7981\text{\AA}$, $\beta=103.83^\circ$ (Kumar et al. 2013). $\beta\text{-Ga}_2\text{O}_3$ is a n-type semiconductor, where conductivity is very sensitive to partial pressures of oxygen in its surrounding atmosphere making it useful for oxygen sensor applications. This reduction in the electric conductivity due to the presence of oxygen can be caused by oxygen deficiency or by gallium excess. The mechanism of oxygen sensing is still under debate, where some authors state that the principal mechanism of conductivity reduction is by the interaction with the oxygen vacancies (Rubio and Ramana 2013a), others suggest that the principle defect type are Frenkel,

with interstitial gallium species (Zinkevich and Aldinger 2001). Furthermore, other researchers assure that the “n-type” conductivity of Ga_2O_3 arises from the Si and H impurities, and the oxygen deficiency will only act as a shallow donor the material (Lovejoy, Chen, Zheng, et al. 2012). It is important to mention that doping with appropriate metallic ions can provide shift in electronic properties to improve different practical applications like gas sensing and transparent conducting oxide (Dakhel 2013; Dakhel 2012).

Recently, $\beta\text{-Ga}_2\text{O}_3$ ceramics were deposited as thin films and nanostructures in order to maximize the surface to volume ratio. However, unfortunately, the properties of the material depend on the deposition method, as well as the processing condition for each deposition (deposition pressure, substrate temperature, and reactive pressure). For this reason, a deeper understanding of the deposition parameters’ influence on the structure and properties of the resulting materials is very important (Kumar et al. 2013). Sputtering is one of the most common deposition methods employed, due to its easy industrialization and repeatability of the process (Wasa, Kitabatake, and Adachi 2004). Nevertheless, other physical and chemical deposition methods were also employed to fabricate Ga_2O_3 thin films. Using Atomic Layer Deposition (ALD) high quality nanocrystalline $\beta\text{-Ga}_2\text{O}_3$ films were deposited achieving full crystallization at 700 C, with (400) texturing (Shan et al. 2005). Sasaki et al. demonstrated the growth of single crystal $\beta\text{-Ga}_2\text{O}_3$ thin films using Molecular Beam Epitaxy (MBE) (Sasaki et al. 2012). Metal Organic CVD (MOCVD) is a chemical vapor deposition commonly used to deposit $\beta\text{-Ga}_2\text{O}_3$ to analyze optical a structural quality of the films being deposited chemically (Mi et al. 2014; Mi et al. 2013). Among the Physical Vapor Deposition (PVD) techniques Electron Beam has demonstrated the capability of growing $\beta\text{-Ga}_2\text{O}_3$ with a morphological features of ~40 nm grain size (Cheng et al. 2013). Furthermore, not only nanostructured films have been realized, but two-dimensional structures

such nanowires based on β -Ga₂O₃ have been explored for transparent conductive oxide and gas sensors applications (López et al. 2014; Z. Y. Zhang et al. 2006).

As mentioned earlier the intrinsic properties of β -Ga₂O₃ can be tuned using different dopants, which can modify the electronic structure, optical properties or crystal structure of the material. Silicon doping into Ga₂O₃ has demonstrated an increment in the conductivity values with incremental concentration of silicon due to the increase in free carrier concentration (Encarnacion G. Villora et al. 2008). Suzuki et al. studied the incorporation of Sn into Gallium Oxide for TCO application, and their results demonstrated that the resistivity value of the films increases with Sn presence due to the direct influence in the carrier mobility of the material (Suzuki et al. 2007). Zhang et al. deposited Cu-doped Ga₂O₃ thin films via rf-sputtering deposition; they showed a narrowing of the band gap of Ga₂O₃ thin films while keeping β -Ga₂O₃ crystal structure (Yijun Zhang et al. 2011a). Titanium doping has been also considered, where the results showed a reduction in the band gap while the monoclinic β -phase was preserved (Dakhel 2013). Lovejoy et al. investigated the effect of the magnetic and electrical properties of doping Ga₂O₃ with Mn and Cr, where they proved that Mn reduces the capabilities of gallium oxide to crystalize, and that the value of the resistivity increases when Mn is presented (Lovejoy, Chen, Yitamben, Shutthanadan, Heald, Villora, Shimamura, Zheng, Dunham, and Ohuchi 2012). Tungsten doping into Ga₂O₃ was studied by different groups achieving a narrowing on the band gap when W-was incorporated, also their results demonstrated only the presence of β -phase crystal structure (Rubio and Ramana 2013a; Dakhel 2012). The correlation between doping of Ga₂O₃ and the actual final application of the material is still uncertain, due to the lack of understanding of the electronic-structural-defect relation for the specific ions used for doping. In this work, we focus our attention on intrinsic and metal-doped Ga₂O₃ thin films. We proposed to evaluate the intrinsic and metal-doped Ga₂O₃

nanostructured thin films for oxygen sensor applications. We will conduct in-depth exploration of metal doping to improve the oxygen sensing properties of Ga_2O_3 .

Chapter 2: Motivation and Significance of the Proposed Project

Sensors based on MOS are most promising for power generation systems due to their small dimensions, low cost, low power consumption, on-line operation, high compatibility with microelectronic processing, and ease of integration into nanotechnology and portable device technology. Therefore, in recent years, extensive studies have been directed towards the fundamental understanding, research, and development of oxygen sensors based on metal oxides. However, despite the fact that there exists a very high demand for advanced oxygen sensors for combustion, the existing technologies suffer from poor response and recovery times and long-term stability. The recent approaches to improve the response time, selectivity and prevent sulfur poisoning have not met with the desired success. Further research and development is needed to realize oxygen sensors that combine rapid response time, selectivity and long-term stability. *This is the impetus for the proposed project to investigate the intrinsic and metal-doped Ga_2O_3 to design oxygen sensors that combine a rapid response, enhanced “3S” criteria, reliability, and robustness at extreme environments for application in power generation systems.* The remainder of this section is devoted to highlight the importance of Ga_2O_3 and what is the intellectual and technical merit of our proposed effort.

2.1 RESEARCH OBJECTIVES AND STATEMENT OF PROPOSED WORK

The hypothesis that constitutes the pillar behind this dissertation work is: **“the refractory metal doping into gallium oxide can improve the 3S criteria combined with rapid response and robustness for utilization in oxygen sensing at extreme environments for power generation systems.”** The challenging goal of the proposed project is, therefore, to create a fundamental understanding of the intrinsic and metal doped gallium oxide sensors for detecting

oxygen in power generation systems. The following are the specific research tasks and objectives of the proposed research project.

2.1.1 Fabrication of Ga₂O₃ Thin Films Based High Temperature Oxygen Sensors

The first objective of this work is to fabricate high quality Ga₂O₃ based sensors by using RF magnetron sputtering, as well as doping Ga₂O₃ thin films with metals to improve the sensor response. The use of sputtering technique is justified by the repeatability of the process, the easiness of the integration with mass production systems and the non-equilibrium state that allow us to combine different materials without the necessity to follow Hume-Rothery rules for alloying (Wasa, Kitabatake, and Adachi 2004). We proposed to undertake the sensors' deposition onto Pyrex glass substrate substrates with integrated Pt interdigital electrodes. At the same time, films were also deposited on Si (100) and Sapphire to facilitate the characterization. The characterization from various analyses was used as a feedback to obtain films with desired structure, morphology, chemistry and dopant concentration.

2.1.2 Optimization of Deposition Conditions

Intrinsic and metal doped Ga₂O₃ films were deposited using RF magnetron sputtering, and the deposition condition were tuned in order to achieve the best structural, electrical, electronic, and morphological conditions to enhance sensor performance. Substrate temperature, sputtering pressure, and partial pressure of reactive gases were varied to obtain intrinsic Ga₂O₃ films. The effect of processing parameters on the crystal structure, grain size, band gap, resistivity, and other related parameters was studied in detail. In the case of metal ions doping, the already mentioned deposition parameter was varied for the film to achieve optimize properties for sensor application; however, sputtering power for doped material was varied to change doping concentration, maximum concentration will be determine by the maximum power allowed before secondary

phase formation starts. For our purpose and benefit of particular research, β -Ga₂O₃ films is the only desired phase. The first phase of the work will examine the metals: Tungsten (W) doping. Determination of the optimum deposition conditions will be achieved via iterative experimentation.

2.1.3 Develop a Structure-Electrical-Processing Conditions Relationship

After fabrication, the films were tested to characterize their properties. The goal was to derive a structure-property relationship, which be helpful to provide a deeper understanding of the Ga₂O₃ films for sensor application. Attempt was made to evaluate the effect of deposition parameters on the structural, optical, and electrical properties. Specific attention was directed towards metal doping, due to the importance of improving sensor performance of the Ga₂O₃ films, with special focus on time response. Time response is determined by the chemical reaction kinetics between the material surface and the oxygen molecules, and by consequence, by the diffusion process and surface reactions (Carpenter, Mathur, and Kolmakov 2003), for that reason the understanding of the defect chemistry for each one of the doping ions is essential. As sputtering deposition is a non-equilibrium technique, the oxidation state, and defect type was also determined experimentally.

2.1.4. Evaluate Ga₂O₃ Based Thin Films for Oxygen Detection at High Temperatures

Ga₂O₃ based films were exposed to test gas(es) under a temperature of 700 °C or higher, and evaluate their capabilities to detect oxygen under those conditions. In this case, samples produced under optimum conditions were introduced into a vacuum chamber and test their variation in electrical conductivity when oxygen is introduced. Sensitivity, time response, and selectivity were the three main properties that were considered when evaluating the sensor performance, also the comparison between pure Ga₂O₃ and metal-incorporated Ga₂O₃ films. Furthermore, the evaluation

of Ga₂O₃ based sensors detection range was evaluated, varying the partial pressure of oxygen introduced, in order to see the range of detection at the already mentioned temperatures.

2.1.5 Investigate the Thermal Stability of Ga₂O₃ Based Thin Films

High temperature oxygen sensors need to tolerate a minimum of 17,000 h of operation (Korotcenkov 2007), for that reason the exposure and analysis of the properties before, during and after exposure is essential. Intrinsic and metal doped Ga₂O₃ films were introduced into a high temperature furnace and exposed to temperature higher than 700 °C for several periods of time. Then, their structural, electrical, and sensor performance were evaluated. Furthermore, surface morphology was also be examined throughout the high temperature exposure.

Chapter 3: Literature Review

3.1 HIGH TEMPERATURE YSZ BASED OXYGEN SENSORS

The first commercial oxygen sensor was introduced by Bosch in 1976 (Ramamoorthy, Dutta, and Akbar 2003). Since then researchers made significant efforts to improve the capabilities for the oxygen sensors. In the case of potentiometric, a high number of articles dedicated towards the reduction of the failure due to reference air leakage. Fouletier et al. showed that a metal/metal oxide mixture encapsulated within a ceramic structure and located doing direct contact with a Pt electrode is capable of generate stable oxygen pressure based on thermodynamic equilibrium at a specific temperature (Fouletier, Vitter, and Kleitz 1975). Furthermore, Haaland suggested the incorporation of a hot press gastight chamber fabricated with Pt/ZrO₂ where O₂ known concentration could be pump (Haaland 1977). Maskell showed three main leak sources in potentiometric oxygen sensors at high temperature, physical leak due to lack of hermeticity, leak due to electronic conduction through the electrolyte, and leakage due to circulating currents in the metal used for sealing (Maskell 2000). In more recent years, several authors have tried to fabricate leak free potentiometric sensors, but they are not capable of avoid all three leak methods. For example, Zhuikov hot-presses a zirconia single crystal into a ceramic tube and caps the apparatus in stainless steel, the author do not indicate the method in which the stainless steel cap/sensor housing bond prevents O₂ leak, but the metal in the cap is in direct contact with the electrolyte which causes leakage through the bonding agent (Zhuiykov 2006). The Kaneko *et al.* model eliminates the leak due to bonding agent/electrolyte interactions by using a metal-free glass seal; however, the sensor still subject suffer leak failure due to hermeticity cause by cracks along the glass-joined circumference and electronic conduction (Kaneko et al. 2005). van Setten *et al.* enclosed a metal/metal oxide mixture below a pulsed laser deposition (PLD)- deposited layers of Ag, glass, and Au. The authors successfully isolated the metal/metal oxide, but the glass used

between the Ag and Au softens at 447 °C, limiting maximum sensor temperature (Van Setten et al. 2002). Spirig *et al.* fabricated a highly advanced potentiometric based sensor where they use a metal/metal oxide seal; seals created by directly fusing zirconia package component. Leak caused by thermal expansion mismatch when the sensor is exposed to temperature cycling and long periods of time are eradicated. When the sensor is exposed to temperature of 600–700 °C, oxygen leak through electronic conduction is the only detectable leak type encountered and can be eliminated by performing an electrochemical treatment. Unfortunately, the sensor fails after 40h of operation at 800 °C (Spirig et al. 2007).

3.2 HIGH TEMPERATURE METAL OXIDE BASED OXYGEN SENSORS

In the case of metal oxide semiconductors for high temperature oxygen sensors, the list of materials capable of detecting oxygen is wide, where the first metal oxide examined was SnO₂ (Jasinski, Suzuki, and Anderson 2003). Since then researches focused their attention into finding materials that best fulfill the requirements for a high temperature oxygen sensor but also to ‘create the proper model and the adequate mechanism of this type of sensor to work in a high oxidizing environments’ (Wang et al. 2010). A number of research groups are trying to improve the sensitivity of the sensors. For example, Chang, et al. demonstrated the effect of thickness in the sensitivity of metal oxide gas sensors, when they exposed Al doped Zinc Oxide sputtering thin films used to detect CO at various temperatures; the authors demonstrated that the reduction of the thickness value will generate higher sensitivity in the films (Chang et al. 2002). In the case of the controlling mechanism for oxygen sensing, authors have shown the effect of the grain size in the band bending caused by the presence of oxygen. In the particular case of SnO₂, researchers found that for high temperature oxygen sensors (> 700 C), in order to avoid band bending at the grain boundaries, the grains need to have a dimensions smaller than their Debye length, approximately

11 nanometers (Barsan and Weimar 2001). The work reported by Sakai et. al. is consistent with the understanding of thickness influence in the oxygen response of SnO_2 , and the effect that porosity has in the type of diffusion controlling the sensing process. The authors build a mathematical model for the sensitivity of the sensing layer as a function of the gas concentration diffused inside the film. At the same time, the set of equation provided by the authors take into consideration porosity level on the films, assuming diffusion takes place in the Knudsen region (Mesoporous film) due to the pore dimension range at which the films is grown, and the effect of temperature of operation (Sakai et al. 2001).

The improvement in the performance of MOS sensors by the modification of their structural formation by the integration of pores has been also studied. Wagner et al. presented a survey of the existing methods to manufacture mesoporous sensors, and the improvements that porosity can achieve. The two main synthesis methods are: “soft-templating” and nanocasting; the first method involves the use of templates or structure directors where the chemical synthesized material is deposited. However, this technique lacks of structural quality, and generally amorphous metal oxides are fabricated. Nanocasting, on the other hand, is capable of fabricating crystalline MOS sensors with high thermal stability, and a predefined surface morphology. The steps of synthesis by nanocasting are presented in figure 3.1; first we have a silica mesoporous based template, that is filled with a carbon precursor (step a), then the silicon oxide is removed by means of wet etch using HF (step b), followed by the deposition of the metal oxide film which forms around the precursor carbon (step c), finally the carbon will be removed and the mesoporous metal oxide is formed (step d) (Thorsten Wagner et al. 2013).

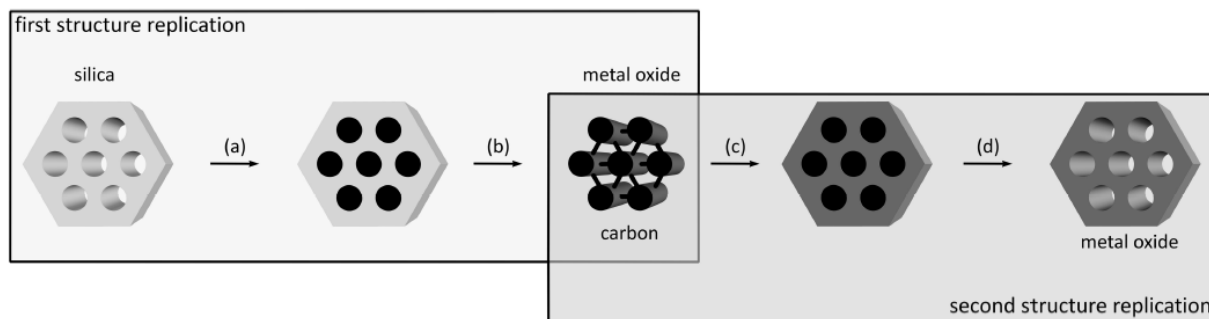


Figure 3.1: Nanocasting synthesis steps for mesoporous metal oxides sensors (Thorsten Wagner et al. 2013).

Numerous metal oxides had enhanced their sensing characteristics by the incorporation of mesoporous formations, i.e. nanocasted In_2O_3 was able to reduce their temperature of operation, and be sensitive to O_3 at room temperature when mesoporous formation was achieved (Th. Wagner et al. 2011). SnO_2 performance was improved by fabricating it via nanocasting, where the sensitivity of H_2 was increased and the CO sensitivity remain unchanged compared to the conventional SnO_2 sensors (Hyodo et al. 2002). Similarly, research performed on sol-gel deposited SnO_2 films vs a high porous SnO_2 demonstrated significant improvement in the response and recovery time of the material when the films contained high levels of porosity (H. Li et al. 2012). Materials such as WO_3 , ZnO , CeO_2 , and Co_3O_4 , also demonstrated improvement in their sensing responses when they were fabricated using mesoporous forming techniques (Thorsten Wagner et al. 2013).

The work on metal oxides has shown promising results when the material is presented as a quasi-one dimensional structure such nanowires, nanorods, nanotubes, nanobelts and so on, which have shown excellent crystallinity and clear facet. Researches expect that quasi-1D nanostructure will show less concentration of point defects as well as specific chemical adsorption and catalytic activities. Furthermore, according to Korotcenkov, quasi-1D nanostructures should provide higher

thermo-dynamical stability than nanograins, making them the preferred structures for high temperature processes. Nevertheless, Korotcenkov explains that the ongoing research is related towards the method of fabrication of these type of nanostructures, but not many investigations were dedicated to the actual application (Korotcenkov 2007). For example, Kolmakov et al. demonstrated the use of nanostructured SnO₂ nanowires for oxygen and CO detection, and at the same time achieving directional growth for all nanowires (Kolmakov et al. 2003). Li et al. showed the use of ZnO nanowires for oxygen sensor applications, where they use a single nanowire structure as a transistor, and the change in the source drain current and in the threshold voltage was used as the measurable properties (Q. H. Li et al. 2004). Similar work was performed by Fan et al. where the use of ZnO nanowires in a MOSFET structure for oxygen detection was studied, but their findings determined the effect that the nanowire diameter has in terms of the sensitivity of the material (Fan et al. 2004). However, this type of technology is not ready for industrialization, and many issues have been found as Choi and Jang presented, they defined certain limitation of quasi-1D nanostructures, especially the fact that real devices is still in a preliminary stage. Furthermore, the lack of integration with a low-cost and high-yield mass production system is the key challenge for the future application (Choi and Jang 2010).

Not only quasi-one dimensional nanostructures have been the focus of recent research towards a faster and more reliable high temperature oxygen sensors, several different structures and materials were also explored. Perovskite structured materials are also under consideration, such as the case of SrTiO₃ which shows both n and p type semiconducting behavior, and the incorporation of dopants do not produce any phase transformation, but enhance their oxygen detection capabilities (Ramamoorthy, Dutta, and Akbar 2003). Menesklou et al. evaluated the oxygen sensor performance of Fe doped SrTiO₃, which reduced the band gap of SrTiO₃ from 3.4 eV to 2.1 eV,

their results showed fast time response (~ 10 ms) at $900\text{ }^{\circ}\text{C}$. The authors also mentioned that with the adequate iron percentage the band gap can decrease to a near zero value (Menesklou et al. 1999). Similar work, was performed by Rothschild where they showed the temperature independency of Fe-doped SrTiO_3 oxygen sensors, this phenomena was attributed to the intrinsic electron-hole generation, which increases proportional to temperature increments, and the reduction reaction which increases resistivity when the partial pressure of oxygen increases (Rothschild et al. 2005). Nevertheless, SrTiO_3 based oxygen sensors present several drawbacks; Rettig and coworkers demonstrated the poisoning effect that SrTiO_3 sensors have in the presence of SO_2 which reduces the long term stability of the material (Rettig, Moos, and Plog 2004); furthermore, Gerblinger et. al. demonstrated the cross-sensitivity effect that several gases such CO , CH_4 , H_2 , CO_2 , and H_2O have in SrTiO_3 based films, and the behavior at different temperatures for each of these gases (Gerblinger et al. 1994).

In the case of simple binary oxides, CeO_2 has proved to be one of the best candidates for high temperature oxygen sensors; plenty of research has been performed into improving and explaining the sensor performance of this material. CeO_2 is capable of detecting partial pressure of oxygen at temperatures $>800\text{ }^{\circ}\text{C}$. Izu et al. demonstrated where they showed the fast time response of CeO_2 sensor which falls in the millisecond range (N Izu et al. 2004). Jasinski, fabricated spin coating thick films based on CeO_2 material, but the time response in their work was in the increased into the seconds range, explaining that the best range of functionality is at $700\text{ }^{\circ}\text{C}$ and $750\text{ }^{\circ}\text{C}$, with a >60 s response time (Jasinski, Suzuki, and Anderson 2003). After optimizing deposition condition for CeO_2 thick films using screen printing Izu and coworkers demonstrated again the fast response time of the sensor at elevated temperatures obtaining values in the range of 10 to 20 ms (Noriya Izu et al. 2004). Response time is one of the best qualities of CeO_2 based sensors, but the work of

Várhegyi et al. demonstrated that at 800 °C, the presence of CO and H₂ can cause CeO₂ to change their O:Ce ratio in the material chemical composition, which provides uncertainties to the oxygen signal (Varhegyi et al. 1994).

Korotcenkov and Cho explained a series of conditions that are capable of producing instability in the sensor response, similar they explain that MOS sensors are required to provide a stable signal from 17,000 to 26,000 hours of operation. The authors mentioned that one of the main disadvantages that MOS sensors have is the lack of information for long period of time analysis because most researches involve only short periods of time and 26,000 hours of operation is beyond the time scale for most of funded investigations; furthermore, the low selectivity is a common disadvantage on most MOS sensors. The authors continued to explain many sources of drift within the sensors response, and among them the following are consider as highly influencing: poisoning, sintering, coking, attrition, volatilization, erosion, thermal shock, and phase transformation. In the case of poisoning, especially in the case of sensor for combustion processes, carbon poisoning is a high influence because it reduces the ability of chemisorption and surface reaction of the sensing layer. No only phase transformation can cause drift in the signal, but secondary phase formation needs to be consider as well because at high temperature lattice diffusion could generate changes in the physical and chemical properties of the material. Continuing with the possible instability agents, the authors mention aging as an important factor, due to studies which demonstrated the change in gran size after several days of MOS sensor operation. Relative humidity is a recurrent issue because it can vary from 10% to 100%, and vapor acts as a donor for MOS sensor; similarly, formation of hydroxylation can cause performance modifications. Thermal stability is affected by the morphology of the sensing layer, and it is highly diminished in cases where grain size dimension is within 3-5 nm. Furthermore, not only intrinsic

properties of the films can influence the instability of the response, but the poor casing of the physical device can reduce the operational life of the sensor. The authors included a list of possible actions that may enhance the stability of the MOS sensors, including increasing the pore size of the films to minimize the humidity impact due to limitation on the vapor condensation inside the pore; similar carbon poisoning is reduced by increasing pore size. Post-deposition annealing reduced the possibility of physical-chemical changes occurring during initial operation, and periodic heat treatment may help in the self-cleaning process of the sensors. The authors suggest that appropriate doping may positively influence the stability of the MOS sensors (Korotcenkov and Cho 2011). In a similar fashion, Sharma et al. demonstrated the drift effect caused by crack formations on the sensing layer after several cycles of operation, these cracks changed the mechanical and electrical properties of the SnO₂ based film that they were examined. The crack formation was caused by the thermal stresses that the films suffered after extensive testing (Sharma et al. 2001)

3.3 GALLIUM OXIDE HIGH TEMPERATURE OXYGEN SENSOR PERFORMANCE

The original investigation of Ga₂O₃ as an high temperature oxygen sensor was performed in 1991 by Fleischer and Meixner, where they determine the gallium oxide films deposited using rf-sputtering depends on the partial pressure of oxygen by the power law of $m=1/4$, and that the response time as a function of temperature varied from ~12 to 3 s when the temperature was increase from 900 °C to 1000 °C (M. Fleischer and Meixner 2000). From that point several authors have tried to improve and optimize the sensor performance of Ga₂O₃ films by varying deposition condition, deposition techniques, electrode contact, and so on. For example, Ogita et al. deposited Ga₂O₃ thin films using rf-magnetron sputtering and investigated the time response and oxygen sensor performance of the films when they were grown at different sputtering pressures, achieving

a time response of 70 s for their best deposition conditions which was the film grew at 2Pa of pressure (Ogita et al. 2001). Bartic et al. used chemical solution deposition to grow Ga_2O_3 thin films, and to evaluate their high temperature oxygen sensor performance when the surface of the films is modified by the process of annealing, they achieved their best time response when the films were annealed for 14 hours at 1000 °C, obtaining 12 s to achieve the 90% of the conductance change (Bartic, Ogita, et al. 2007). Baban et al. employed different electrodes configuration to evaluate the response time of Ga_2O_3 films deposited using rf-magnetron sputtering, the authors used two types of electrodes setup interdigital and sandwich structure, obtaining best results when interdigital configuration was employed (Baban, Toyoda, and Ogita 2005). Ju and Ju, tested the used of surface etching on the Ga_2O_3 sensing layer, they created a V-groove pattern in the sensing layer by using photolithography, and obtained a response time of 12.5 seconds. (Long-Tsong Ju 2011). No only modification of the sensing layer or the electrodes configuration has being tested, also the type of measurement was analyzed in order to obtain more accurate readings. Fleischer et al. evaluated the performance of Ga_2O_3 based oxygen sensor when AC signal is used to measure the resistance shift in the presence of oxygen and compared to DC signal. It was evident that with AC the recorded resistance change showed higher stability, this is due to the fact that when DC reading are measured only electric conductivity is accounted, but when AC is employed the ionic conductivity that Ga_2O_3 films presents is also recorded (M Fleischer et al. 1995).

On the other hand, the use of dopants and different materials as surface modification has been studied in order to improve Ga_2O_3 sensor capabilities. SnO_2 incorporation into Ga_2O_3 semiconductor was considered by several authors. Frank et al. showed the effect of having a layer of SnO_2 deposited below the Ga_2O_3 films using screen printing to create both Ga_2O_3 and SnO_2 layers. The oxygen sensor performance was not altered, but the conductivity of the films was

improved (Frank, Fleischer, and Meixner 1998). Similar work was performed by Frank et al. by incorporating multilayer of SnO_2 into Ga_2O_3 films. They used sputter deposition to achieve the sandwich structure showing similar results as in their previous work, in which the resistivity of the films was reduced which allows the a reduction in the sensor size due to the possibility of the reduction in size of the interdigital electrodes (Frank et al. 1998). In 1996 Frank et al. evaluated the incorporation of different dopant layers into Ga_2O_3 films, in their work three different material were incorporated and analyzed: ZrO_2 , TiO_2 , and MgO , forming sandwich structures similar to the work with SnO_2 previously mentioned. In their findings, no effect on the sensor capabilities of Ga_2O_3 films to oxygen was obtained (Frank, Fleischer, and Meixner 1996). Li et al. also investigated the effect of different doping agents into gallium oxide. The authors did not presented any information about the defect equilibria, but it could be assumed that most of the defects are acting as interstitial due to the deposition method. They deposited the films using sol-gel technique, where they achieved different resistivity values for each film, successfully lowering the time response value, the best results when Ce was doped, but the working temperature was $<600^\circ\text{C}$ (Y. Li et al. 2003). It is important to mention that none of these Doped Gallium Oxide films presented nanostructured surface crystallization, only involving ‘some features of the sensors’ in order to reduce the response time. In the case of surface modification, catalytic active materials which, in the case of reaction involving oxygen, can change both the surface potential and concentration of point defects were also studied (Korotcenkov 2007), Schwebel et al. deposited CeO_2 , La_2O_3 , and Mn_2O_3 oxides on top of a sputter-deposited Ga_2O_3 film in order to reduce any possible cross-sensitivity to reducing gases at 600 to 900°C ; nevertheless the deeper understanding was towards La_2O_3 incorporation, which did not produced any effect on the sensitivity of the film. Also, it was shown a decrease in the sensitivity of the film when methane was presented, and the

modifying La_2O_3 layer was introduced (Schwebel, Fleischer, and Meixner 2000). Similar work was presented by Fleischer et al. in 1996, where they produced a surface modifier layer of WO_3 , NiO , and AlVO_4 on top of Ga_2O_3 sputtered films. The oxygen response for the doped films was not improved, and even reduced the oxygen sensing capabilities; however, Ga_2O_3 is not good for detecting NO_x or NH_3 , but when the layers are presented, Ga_2O_3 based sensor is capable of producing an electric resistance change in the presence of the mentioned gases. Nevertheless, an important finding of this work was when the WO_3 layer was deposited on top of the film; after exposing the material to temperatures higher than 800°C the WO_3 was lost, which could translate into diffusion toward Ga_2O_3 films or /and to the evaporation of the film (M Fleischer et al. 1996).

Not only has the improvement of Ga_2O_3 oxygen sensor capabilities been investigated, but also the interaction of O_2 and Ga_2O_3 at high temperatures, and the effect on the conduction mechanism was considered in the past. Kiss et al. presented a work on the impedance analysis of Ga_2O_3 films following the findings of Fleischer et al. where the resistance change was recorded using AC source. Their finding showed the importance of the frequency selected to perform the sensors test, saying that the sensitivity of Ga_2O_3 depends on the frequency applied, also they suggested that the oxygen ion adsorption is through the grain boundaries (Kiss et al. 1999). Kiss et al. continued their work performing impedance spectroscopy on Ga_2O_3 films in the range of 578 to 850°C , where they found the effect of the grain boundaries in the oxygen sensor performance, suggesting that after 700°C the Debye size of the grain reduces to less than 30 nm ; however, the conduction mechanism is the same for all the range which is through the grain mainly (Kiss et al. 2000). In the work of Várhegyi et al. the effect of corrosive gases in the surface of Ga_2O_3 films; their finding suggest that Ga_2O_3 shows no effect when exposed to SO_2 at high temperatures, but when the films were exposed to Cl_2 , Ga_2O_3 films started to be removed from the substrate (Varhegyi et al. 1994).

Finally, the work done in Ga_2O_3 for oxygen sensors application also includes researchers that have employed quasi 1D technology to improve the sensor characteristics of Ga_2O_3 material. Feng et al. reported the use of individual Ga_2O_3 nanowire to detect oxygen, the authors do not use standard resistivity shift technique, but the use of the change in current in the presence of oxygen when illumination is presented, this change is attributed to the presence of photo-generated carriers. Their finding suggests fast change when partial pressure of oxygen is introduced, and faster response than using conductometry evaluations (Feng et al. 2006). Liu et al. used multiple nanowires and recorded the shift in electrical conductance in the presence of 1% of O_2 at 300 °C, but the time response and sensitivity of the films was not specified (Z. Liu et al. 2008).

Chapter 4: Materials and Methods

4.1 MATERIALS

Targets: Materials for rf-sputter deposition were obtained from Plasmaterials and Kurt J. Lesker. The targets (99.99%) that were procured for this project are: (1) Ga_2O_3 and (2) W; nevertheless, a 99.95% W target was also employed to determine the modification caused to the sensor under different levels of purity. These targets were primarily used to test the key idea of the project. The dimensions of the target are 2 inch diameter and 0.125 inch thickness. The targets are shown in in Figure 4.1. For the case of Ga_2O_3 , a 0.125 inch thick Cu backing plate is required to protect the target.

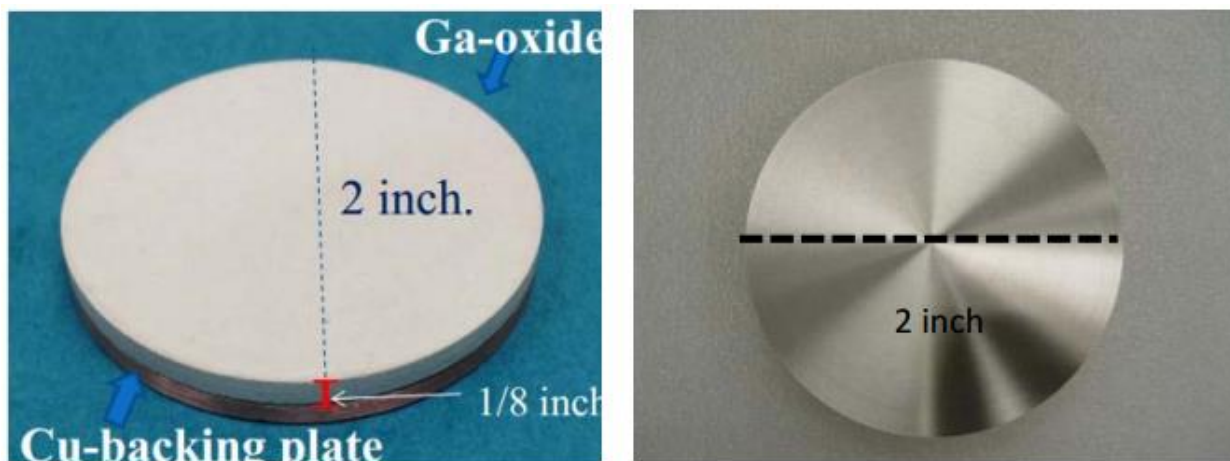


Figure 4.1: The Ga_2O_3 (left) and W (right) targets employed in this project work.

Substrates: Three different types of substrates were employed.

1. Sapphire ($\alpha\text{-Al}_2\text{O}_3$ (0001)): to evaluate high temperature performance of the films, as well as to evaluate the optical characteristics of Ga_2O_3 based films;
2. Silicon (Si (100)): to facilitate characterization of film's chemistry; and
3. Pyrex Glass (Figure 4.2) with integrated with Pt interdigital electrodes (200 nm thick with distance of $10\mu\text{m}$ between electrodes): to evaluate sensor performance.

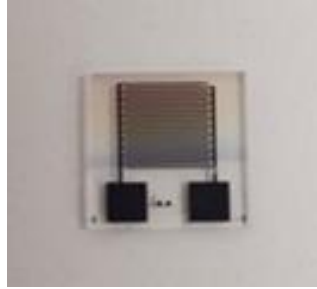


Figure 4.2: Actual image of an employed pyrex glass substrate with integrated interdigital electrodes

4.2 SUBSTRATES

Sapphire discs and silicon wafers were employed for depositing the Ga_2O_3 based thin films. The substrates were purchased from University Wafer Inc. The dimensions of the Sapphire substrates were 0.044 cm thick and 5.8 cm in diameter. These wafers were then cut into pieces using a glass cutter in order to obtain smaller size substrates with an average surface area of 1 cm^2 . The small pieces cut from the wafer are used as the substrates on which the films will be deposited. The sapphire samples were cleaned by a bath of 99.9% ethanol for 15 minutes, in order to remove oxides and impurities on the surface of the substrate. P-type, Si (100) was employed; these wafers were cleaned with standard RCA cleaning procedure to remove organic, inorganic and metal particulate contaminants. The following steps were performed:

- SC1- Removal of insoluble organic contaminants using 5:1:1 $\text{H}_2\text{O}/\text{H}_2\text{O}_2/\text{NH}_4\text{OH}$ mixture.
- SC2- Removal of ionic and heavy metal atomic components using a solution of 5:1:1 $\text{H}_2\text{O}/\text{H}_2\text{O}_2/\text{HCl}$ solution
- Removal of native oxide by buffered oxide etches solution ($\text{HF}/\text{H}_2\text{O}$; 1:100).

The SC1 solution was prepared by heating 50 ml of Deionized water (DI) water to a temperature of 100°C and then adding each 10 ml of NH_4OH and H_2O_2 to the DI water. SC2

solution was prepared by 10ml each of H_2O_2 and HCl to 50ml of water. The silicon substrates were soaked for 10 min in each solution and followed by 5 min of DI water rinse after each soak. Finally, the silicon substrates were treated with BOE to remove any native oxide on it (Louisville, n.d.).

4.3 RF- SPUTTERING DEPOSITION SYSTEM

Sputtering deposition is a process for depositing thin films that implicates the bombardment of a target with energetic particles (positive gas ions), which cause some surface atoms to be ejected from the target material, in this case Ga_2O_3 and W. These atoms are then deposited on substrates. Due to the fact that sputtering uses low substrates temperature, it is an ideal method to deposit contact metal for thin films. This technique is broadly used in semiconductor industries for fabricating thin films in IC processing application (Wasa, Kitabatake, and Adachi 2004).

Sputtering deposition system consists of a pair of electrodes, the cathode that is located at the target side, and the anode where substrate is placed. A target is made up of the material that will be used for thin film deposition onto substrates. The pair of electrode is located inside the low pressure vacuum chamber; the design of the vacuum chamber can change depending on the needs. This is a chamber filled with the sputtering gas, usually an inert gas such as Argon (Ar). Gas plasma is struck using an RF power source, causing the gas to become ionized. The ions are accelerated towards the surface of the target, causing atoms of the source material to break off from the target in vapor form and condense on all surfaces including the substrate.

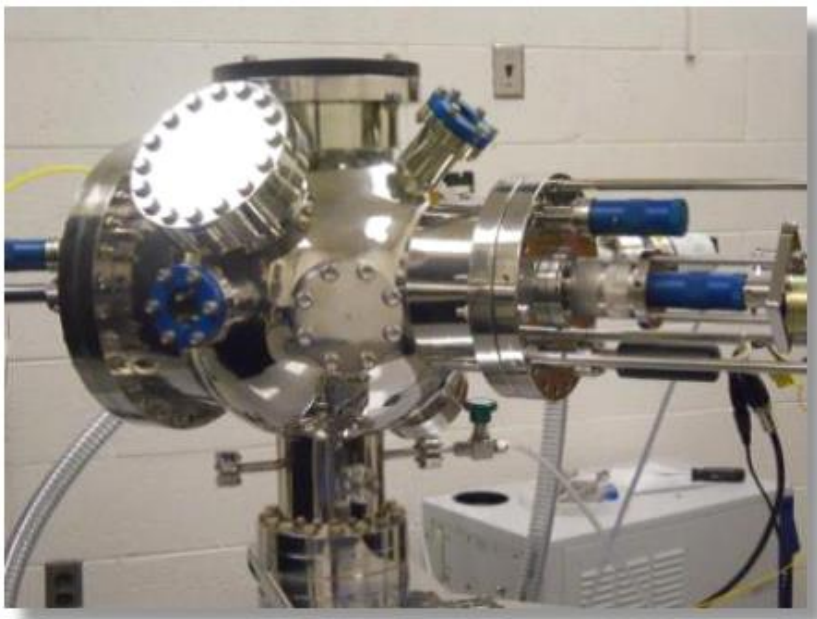


Figure 4.3: RF-sputtering deposition system and sample holder with integrated heater and thermocouple

After the samples were cleaned, the next step was introducing them inside the vacuum chamber of the sputtering machine. The sputtering machine used is the Excel instruments Model DCSS- 12, and the entire set-up is as shown in Fig. 4.3. The samples were collocated in the sample holder that is 8 cm away from the plasma gun. The chamber was initially evacuated to a base pressure of $\sim 0.21\text{mPa}$; however, the sputtering pressure was at $\sim 0.5\text{ Pa}$. The W and Ga_2O_3 targets was placed in a 8 cm sputtering gun, which was cooled down with water with the help of Polyscience recirculation chiller. An initial sputtering power of 20 W was applied to the target via the sputtering gun while introducing high purity argon (Ar) into the vacuum chamber causing plasma ignition. Once ignited, the power was increased to 100 W at the Ga_2O_3 gun and to the respective variable power for W gun to deposit the films. The flow of the Ar was controlled using MKS mass flow meter with the values from 10-40 sccm (standard cubic centimeter per minute). Before each deposition, the both targets were pre-sputtered for 20 minutes using argon keeping the shutter above the gun closed to prevent cluster formation caused by the plasma ignition. The

depositions were performed at variable temperatures, the substrates were heated using the sample holder which contains an integrated hot plate, and the temperature was registered using a K-type thermocouple located within the sample holder/heater. Different variety of samples were deposited using this technique, the deposition parameters which were modified to optimize the material features are the following: substrate temperature, oxygen partial pressure, time of deposition, and W-sputtering Power (P_w). Figure 4.4 shows the actual co-sputtering taking place inside the system described above, similarly table 1 presents the list of samples employed

Table 3.1: List of samples and conditions of deposition

Sample ID	W-Sputtering Power (Watts)	Temperature (°C)	Ar:O ₂ Flows (sccm)	Time (minutes)	Substrate
GA01	0	500	40:0	30	Si, Al ₂ O ₃ , Pyrex
GA02	0	500	40:0	60	Si, Pyrex
WGA01	50	500	35:5	30	Al ₂ O ₃
WGA02	50	500	30:10	60	Si, Al ₂ O ₃ , Pyrex
WGA03	20	500	30:10	60	Si, Al ₂ O ₃ , Pyrex
WGA04	40	500	30:10	60	Si, Al ₂ O ₃ , Pyrex
WGA05	60	500	30:10	60	Si, Al ₂ O ₃ , Pyrex
WGA06	75	500	30:10	30	Si, Al ₂ O ₃ , Pyrex
WGA07	100	500	30:10	30	Si, Al ₂ O ₃ , Pyrex
WGA08	100	500	30:10	60	Si, Pyrex
WGA09	50	600	30:10	30	Si
WGA10	50	700	30:10	30	Si

WGA11	50	800	30:10	30	Si
-------	----	-----	-------	----	----

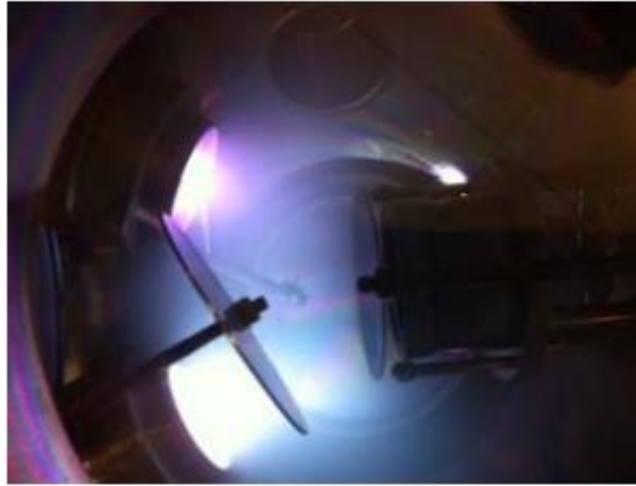


Figure 4.4: Co-sputtering deposition of W and Ga₂O₃

4.4 ANALYTICAL TOOLS

The analytical tools employed to characterize the physical and chemical properties of the films are the following. X-Ray diffraction (XRD), scanning electron microscope (SEM), Spectrophotometry, X-ray Photoelectron Spectroscopy (XPS), Rutherford BackScattering (RBS), Atomic Force Microscope (AFM), Nanoindentation, and Optical Ellipsometry. These techniques that allowed us to create the behavioral map needed to achieve this research goals, and to provide enough evidence of the effect of the variation of the deposition conditions on the intrinsic properties of the Ga₂O₃ films.

4.4.1 Rutherford Backscattering Spectrometry (RBS)

Ion beam analysis of the Ga₂O₃ based films was performed to understand elemental depth distribution, and thickness variation. Rutherford backscattering spectrometry (RBS) experiments

were carried out in the accelerator facility at the Environmental Molecular Sciences Laboratory (EMSL) within the Pacific Northwest National Laboratory (PNNL). The RBS experiments were performed at the National Electrostatic Corporation (NEC) RC43 end station. Rutherford Backscattering was performed using a 3.0-MV tandem electrostatic accelerator that provides two stages of acceleration (negative ion acceleration from the source end to the terminal in the middle and positive ion acceleration from the middle to the high-energy end). The final energy depends on the charge state of the ion. The accelerated ions are focused through the high-energy beam line using a magnetic quadrupole and a y-axis electrostatic steerer. The helium ion source used for this analysis was the radio frequency RF (Alphatross) plasma which accelerated helium ions to the sample to be analyzed in the end station where Ion-scattering measurements are performed in the second level using a fixed-position detector at a scattering angle of 150° for RBS spectrometry. The analysis was performed using a helium beam with an energy of 2000 KeV in an incident angle $\alpha = 7^\circ$, the exit angle $\beta = 15^\circ$, a scattering angle $\theta = 150^\circ$ and a detector resolution of 20 KeV. A schematic of the setup is depicted in Figure 4.5.

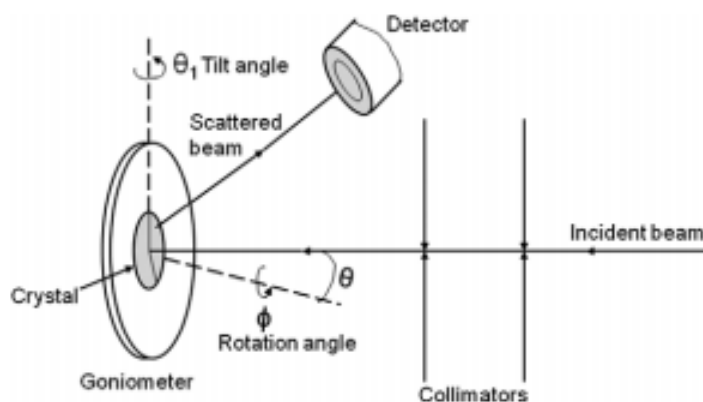


Figure 4.5: RBS schematic diagram.

The composition and thickness of the films were determined by simulating the experimental spectrum for the set of experimental conditions. The experimental curve along with the simulation curve calculated using SIMNRA code (M. Mayer 1999; Matej Mayer and Mayer 1997). The simulated curve was calculated using SIMNRA code for the fixed set of experimental parameters: (1) incident He⁺ ion energy, (2) integrated charge, (3) energy resolution of the detector, and (4) scattering geometry. This characterization tool enables the user to find a very accurate weight percent composition given in concentration or area density. The thickness of the thin film was also calculated using this technique.

4.4.2 X-Ray Photo Electron Spectroscopy (XPS)

X-ray photoemission spectroscopy (XPS) is a technique that uses x-ray inelastic scattering phenomena to quantify chemical data. For this experiment, the sample is bombarded with X-rays ($E < 10$ KeV) from a single source. The X-rays interact with the atoms on the surface of the material, causing the electron emission, this phenomenon is called the photoelectric effect. The emitted electrons will have the measured kinetic energies given by

$$KE = h\nu - BE - \phi \dots\dots\dots 4.1$$

where h is Planck's constant, KE is kinetic energy of the electrons, BE is binding energy of the electrons, and ϕ is the spectrometer work function (Alford, Feldman, and Mayer 2007).

The equipment use for this experiment is the Kratos Axis Ultra X-ray Photoelectron Spectroscopy (XPS) system located at the Materials Research Laboratory (MRL) at the University of California Santa Barbara (UCSB). An ultrahigh vacuum environment of 10^{-11} Torr is required for the machine to work. Core scans were performed on all samples from 20 eV to 600 eV of binding energy, and high resolution scans were performed at different energy level to obtain a clear

idea of the valence state of the chemical components. Figure 4.6 shows the equipment employed for these tests.



Figure 4.6: Kratos Axis Ultra X-ray Photoelectron Spectroscopy (XPS) from UCSB

4.4.3 X-Ray Diffraction (XRD)

X-Ray Diffraction is an analytical technique where x-ray are emitted and directed towards a material where atoms cause the x-ray to diffract. The diffracted X-rays allows us to collect information of the crystallinity nature of the material due to the following mechanism (Australian Microscopy and Microanalysis Research Facility 2014):

$$n\lambda = 2d\sin\theta \dots\dots\dots 4.2$$

Where n is an interger, λ is the X-ray wavelength, d is refer to the interplanar distance, and θ is the Bragg's angle. Figure 4.7 shows the graphic representation of the X-ray-Material interaction.

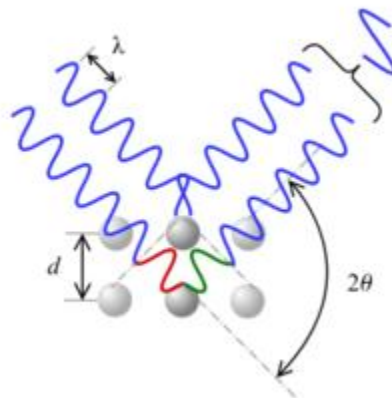


Figure 4.7: Schematic diagram of X-ray-crystalline material interaction

To avoid interference by the substrate and obtain diffraction pattern of the films, we performed grazing incidence X-ray diffraction (GIXRD) on the Ga_2O_3 thin films on Si substrates. Bruker D8 Advance X-ray diffractometer (Figure 4.8) was the device employed to obtain the GIXRD measurements and patterns. All the measurements were made ex-situ as a function of films deposition parameters. GIXRD patterns were recorded using $\text{Cu K}\alpha$ radiation ($\lambda = 1.54056 \text{ \AA}$) at room temperature. A high voltage of 40 kV was used to generate the X-rays. The GIXRD patterns were recorded employing the X-ray beam fixed at a grazing incidence of 1° . The scanning was performed in a 2θ range of $20\text{--}65^\circ$ using the “detector scan” mode, where the detector was independently moved in the plane of incidence to collect the diffraction pattern. The step size and the scan speed were 0.01° (2θ) and $2^\circ/\text{min}$, respectively. For these set of conditions, the X-ray beam passes sufficiently long distances through the coating to provide the observed diffraction patterns. The data was acquired and analyzed using EVA software in order to compare the XRD peaks, and check for the crystal structure and lattice parameters. The XRD measurements were performed systematically after each and every step of the characterization procedure i.e., deposition, heat treatment, and long term stability test.



Figure 4.8: Full view of the XRD system

4.4.4 Scanning Electron Microscopy

Scanning electron microscope is a technique that employs a focused beam of electron to reveal the superficial features of the analyzed samples. The high energy electron are emitted from an electron gun, then the electron are focused towards the specimen and systematically scan the surface. The image is created by a rastering process where the beam illuminate one point at the time (Australian Microscopy and Microanalysis Research Facility 2013). The samples were mounted on top of a small circular stage of 1 inch diameter and carbon tape was used to avoid any kind of electrical disturbance from the circular metallic stage; however, a piece of copper tape was added to each sample in order to make electron flow easier. The SEM provided images from different magnifications of the samples, with the intention of providing a better image of the grain size, as well as the morphology of the thin films. Similarly any pore formation or crystallization

was recorded as a function of sputtering power or the dependent deposition variable analyzed. The electron incident current and voltage was varied depending in the quality of the samples to obtain the best resolution image. The machine allows you to take several pictures of the image that the user is observing at different magnifications. After the picture is saved, it is open in the software Quartz PCI, which allows you to measure the grain size of the films. The machine used for this experiment is the Hitachi S-4800 electron microscope (Figure 4.9).



Figure 4.9: Hitachi S-4800 SEM

4.4.5. Nanoindentation

The nano-mechanical properties of the films were evaluated using nano-indentation technique. Indentation requires some parameters to allow the estimations correctly, among them: Young's modulus, Poisson's effect, yield strength, strain-hardening exponent, hardness, fracture toughness, and areas. The areas are calculated at different stages of the process, during loading, holding and unloading. Figure 4.10 shows a representative curve for the loading and unloading sections which

are highly affected by a combination of elastic, plastic and fracture response, whereas the hold portion is more influenced by viscoelastic (Oliver and Pharr 1992).

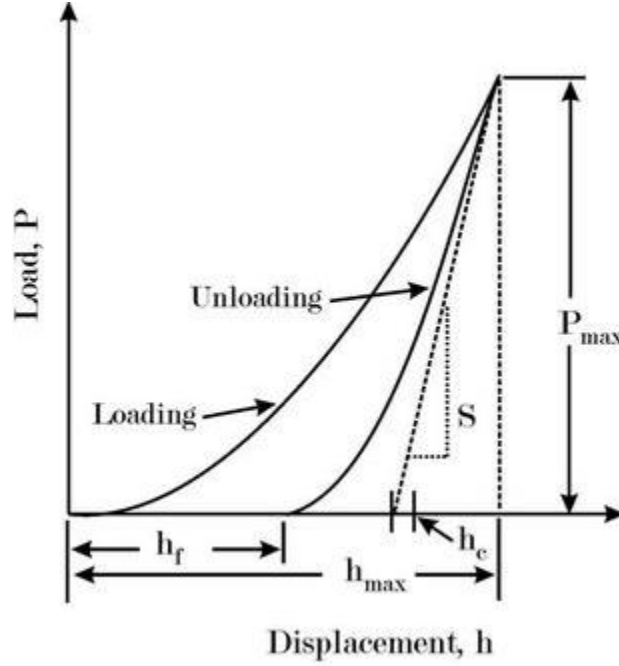


Figure 4.10: Load vs Displacement curve representative for nanoindentation experiments (Tiwari 2012)

The mechanical properties of the indented sample can be obtained by the initial unloading response using the following equation:

$$\frac{dP}{dh} = \frac{2}{\sqrt{\pi}} \sqrt{A_c} E_r \dots \dots \dots 4.3$$

where P is contact force, h indentation depth, E_r is the reduce modulus and A_c is the contact area; the latter two are calculated with equation 4.3:

$$A(h_c) = C_0 h_c^2 + C_1 h_c + C_2 h_c^{1/2} + C_3 h_c^{1/4} + \dots + C_8 h_c^{1/128} \dots \dots \dots 4.4$$

$$\frac{1}{E_r} = \frac{1-v_i^2}{E_i} + \frac{1-v^2}{E} \dots \dots \dots 4.5$$

In equation 4.5 the subscript i corresponds to the indenter, v is the Poisson's ratio, and E corresponds to the Young Modulus. In the case of equation 7, h_c is contact indentation depth, and

C_0 - C_8 are constants calculated through calibration of a indenter contact area that can be obtained by a manipulation of Sneddon analysis for the indentation of an elastic half space by a flat, cylindrical punch, using the basic assumption that during the initial withdrawal of the indenter, the contact area between the indenter and the specimen remains constant (Pharr, Oliver, and Brotzen 1992). Nevertheless, the value for h_c need to be carefully calculated using the following formula:

$$h_c = h_{max} - \varepsilon \frac{P_{max}}{S} \dots\dots\dots 4.6$$

Where P_{max} and h_{max} are first point during unloading, and S is contact stiffness dP/dh . All the tests were performed using a Hysitron TI 750 TriboIndenter where indentation was used to derive a relation between the tungsten quantities and the mechanical properties of the films. Load-controlled indentation tests were performed on each sample to determine the maximum load that could be applied in the film without penetrating more than 10% of the total film thickness. Indentations were done using a diamond Berkovich tip with a radius of curvature 396 nm to obtain values for hardness and reduced modulus of each sample. Ten indents were performed for each film evaluated

4.4.6. Spectrophotometer

Transmittance and reflectivity of the films were recorded using spectrophotometer, in particular the model Cary 5000 UV–Vis–NIR double-beam spectrophotometer. The films deposited on sapphire were used for measurements in a wavelength range of 190 nm to 2000 nm; transmittance and reflectance values will help us to calculate the band gap value of the films, and determine the effect of metal ions in the electronic structure of Ga_2O_3 films. Furthermore, the evaluation of the optical properties will provide valuable information for future research dedicate to Ga_2O_3 for transparent conductive oxide applications. Spectrophotometry possess a light source

which has to cover the entire measured range, so it uses a combination of deuterium emitter for the UV region, and tungsten or halogen lamp for the visible region.



Figure 4.11: Cary 5000 UV–Vis–NIR double-beam spectrophotometer

The transmittance obtained from the samples is used to calculate the band gap of the films. The absorption coefficient (α) is determined using the thickness (t) of the film and value of the transmittance spectra (T) using the following formula

$$\alpha = \frac{-\ln T}{t} \dots\dots\dots 4.7$$

Then we can calculate the photon energy ($h\nu$) by using the wavelength (λ) in the next equation:

$$h\nu = \frac{1240}{\lambda} \dots\dots\dots 4.8$$

The band gap value is calculating by using the following equation:

$$ah\nu = B(h\nu - E_g)^{1/2} \dots\dots\dots 4.9$$

where B is a proportionality constant and E_g is the band energy, the band gap of the films are calculated by plotting a graph between $(\alpha h\nu)^2$ and $h\nu$ (Sinha, Adhikary, and Chaudhuri 2005; Gullapalli, Vemuri, and Ramana 2010; Kumar et al. 2013).

4.4.7. Spectroscopy Ellipsometry

Spectroscopic ellipsometry (SE) is a technique that measures the relative changes in the amplitude and phase of the linearly polarized monochromatic incident light upon oblique reflection from the surface of the evaluated films. The experimental parameters obtained by ellipsometry are the angles Ψ (azimuth) and Δ (phase change), which relate to microstructural-optical properties, defined by:

$$\rho = \frac{R_p}{R_s} = \tan \Psi \exp(i\Delta) \dots \dots \dots 4.10$$

In this case, R_p and R_s are the complex reflection coefficients of the light polarized parallel and perpendicular to the plane of incidence, respectively (Fujiwara 2007; Vargas et al. 2014; *Guide to Using WVASE32 Spectroscopic Ellipsometry Data Acquisition and Analysis Software* 2008; Auciello and Krauss, n.d.). The mechanism which ellipsometry uses to relate the measurable with the accessible optical parameters is the following equation:

$$\rho = \tan \Psi \exp(i\Delta) = \rho(N_0, N_1, N_2, L_1, \Phi_0, \lambda) \dots \dots \dots 4.11$$

where $\tan \psi \exp(i\Delta)$ terms are the parameter that are measurable, and the terms on the right hand side are the parameters that can be calculated from the measurements such: film thicknesses, optical properties, the wavelength of light, and the angle of incidence (Khoshman, Khan, and Kordesch 2008). The dependence of the parameters Ψ (azimuth) and Δ (phase change) of the light spectra can be fitted to obtain film thickness and the optical constants, based on the best fit between experimental and simulated spectra using the correct fitting model (Fujiwara 2007; Vargas et al.

2014; Auciello and Krauss, n.d.). In the present case, the Levenberg-Marquardt regression algorithm was used for minimizing the mean-squared error

(MSE):

$$MSE = \frac{1}{2N-M} \sum_{i=1}^n \left[\left\{ \frac{(\Psi_{exp} - \Psi_{calc})}{\sigma_{\Psi_i}^{exp}} \right\}^2 + \left\{ \frac{(\Delta_{exp} - \Delta_{calc})}{\sigma_{\Delta_i}^{exp}} \right\}^2 \right] \dots\dots\dots 4.12$$

where Ψ_{exp} , Ψ_{calc} and Δ_{exp} , Δ_{calc} are the measured experimentally and calculated functions of from the spectroscopy, N is the number of measured Ψ and Δ pairs; M is the number of fitted variables in the model and σ is standard deviations for Ψ and Δ (Fujiwara 2007).

The construction of a multilayer optical model is essential to successfully simulation of the experimental data to extract the desired parameters. The model representation is showed in Figure 4.12 which accounts a set of different layers such roughness, substrate, thin film and SiO₂ formation. Each one of these layer have a distinct optical dispersions and the interfaces between them act as optical boundaries where light is refracted and reflected, according to the Fresnel relations. The experimental data is fitted using the appropriate dispersion model.

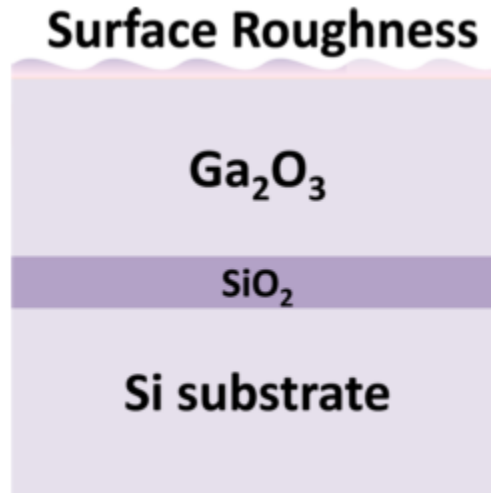


Figure 4.12: The stack model of the Ga₂O₃ based samples constructed for ellipsometry data analysis

In the case of Ga₂O₃ based films the data was fitted with the conventional Cauchy dispersion model which is the ideal model for transparent materials (*Guide to Using WVASE32 Spectroscopic Ellipsometry Data Acquisition and Analysis Software* 2008). The Cauchy equation can be expressed approximately as a refractive index n as a function of wavelength λ :

$$n(\lambda) = a + \frac{b}{\lambda^2} + \frac{c}{\lambda^4} \dots\dots\dots 4.13$$

where a , b , and c are the Cauchy coefficients and particular to the material. a , b and c control $n(\lambda)$ at different ranges of the light spectra, A is the long wavelength, B controls the curvature in the middle of the visible-spectrum, and C in shorter wavelengths (Vargas et al. 2014; Fujiwara 2007; Auciello and Krauss, n.d.). It is important to consider that the principle behind Cauchy's polynomial is also used for in the dispersion function $k(\lambda)$:

$$k(\lambda) = d + \frac{e}{\lambda^2} + \frac{f}{\lambda^4} \dots\dots\dots 4.14$$

where d , e , and f are parameters specific to the material (Fujiwara 2007; *Guide to Using WVASE32 Spectroscopic Ellipsometry Data Acquisition and Analysis Software* 2008; Auciello and Krauss, n.d.).

SE measurements were performed ex-situ from the deposition chamber on the films deposited on the Si substrates by using a J. A. Woollam V-VASE instrument (Fig. 3.10). Measurements were done in the range of 300 to 1350 nm with a step size of 2 nm and at angles of incidence of 65°, 70°, and 75°, near the Brewster's angle of silicon. The experimental data was simulated and the parameter were obtain by utilizing WVASE32 software.

4.5 THERMAL STABILITY.

The evaluation of the long term stability of the sensors when they are exposed to high temperature (>700 °C) cycles of operation, the sensors deposited on sapphire (after optical

evaluation) were subjected to several time lapses of exposure, starting by 1 hours and finishing after 15 hours, with different exposure times. The films were introduced to CM Rapid Temp Furnace, and examined after each cycle and the temperature ramping rate was kept constant to 10 °C/minute. The structural stability and morphology was evaluated using the previous mentioned analytical tools. Furthermore, the evaluation of the thermal shock resistance of the films is examined using this instrument, when the samples are exposed to the already mentioned temperature, and expose them to a rapid temperature gradient by exposing them to room temperature.



Figure 4.13: Thermal-Cycling Furnace

4.6 HIGH TEMPERATURE OXYGEN SENSOR PERFORMANCE

The oxygen sensing characteristics of the materials were evaluated using the Pyrex glass substrate with interdigital electrodes deposited on the surface, and the films deposited on alumina substrate by attaching two electrodes at the surface of the films (line set-up). Both set-ups were

annealed to 700 °C for 1 hours before performing the sensor testing. Figure 4.14 shows a schematic diagram of the sensing process of the films. In both cases, two wires are attached to each electrode by using a high temperature silver paste (Ted Pella), and curing it at 93 °C for two hours to achieve minimum resistivity and maximum mechanical properties. As mention before, the MOS sensors works by changing the conductivity values when different partial pressures of oxygen are introduced, and in our case we measure the conductivity values by means of Ohm's Law, which express as follows:

$$V = IR \dots\dots\dots 4.15$$

Where V is Voltage, I is the inputted current, and R is the resistance value of the film. The resistivity was later calculated using the following equation:

$$\rho = R \frac{A}{l} \dots\dots\dots 4.16$$

Where ρ is the resistivity, A is the cross-sectional area of the electrodes, and l is the distance between the interdigital electrodes, and finally conductivity is obtained by obtaining the reciprocal of the resistivity:

$$\sigma = 1/\rho \dots\dots\dots 4.17$$

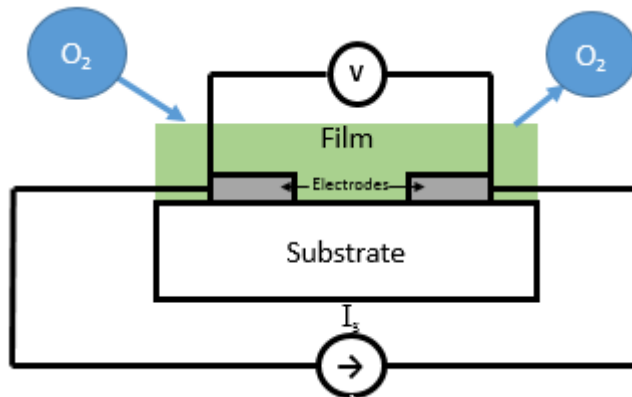


Figure 4.14: Schematic diagram of functional MOS sensor and the oxygen interaction

Figure 4.15 shows the schematic diagram of the experimental set up used for the sensor testing. In our setting, we used a stainless steel chamber with a sample holder with an integrated heater and thermocouple to maintain steady state temperature during the experiments. The chamber has access for 4 electrical terminals, two for the current input and two for the voltage measurements. The current source employed is a Keithley 220 Programmable current source, and the voltage was measure with a Keithley 6514 system electrometer with GPIB connection to computer interface and data acquisition. LabView software was used to create a data acquisition program that recorded the voltage values from the electrometer.

The chamber contained a gas outlet and a gas inlet, and the pressure was obtained by varying the partial pressures of the inputting gases. The gas flow was controlled by MKS mass controllers, where the partial pressure of oxygen was varied to determine the different sensing characteristics of the films. Argon was used as a baseline for oxygen-free environment and a mixture of Ar/O₂ was employed for all test. The sensor testing was performed at a temperature of 800 °C, and a maximum volume flow rate of Ar was 200 sccms.

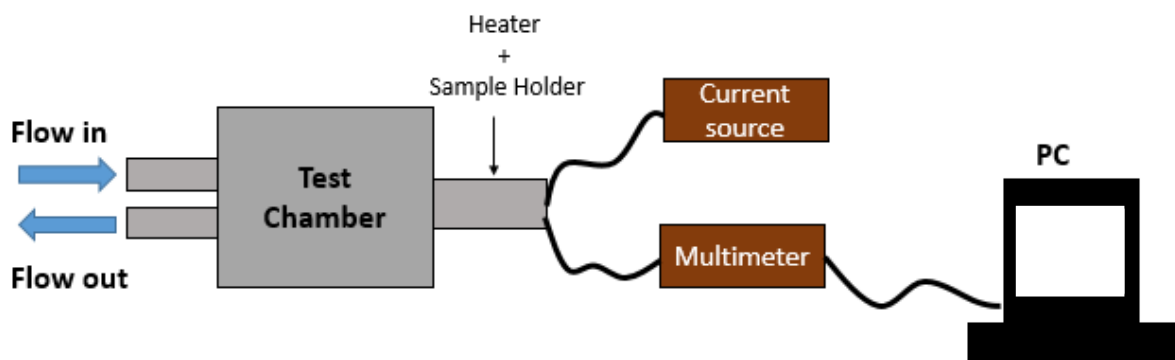


Figure 4.15: Schematic diagram for the high temperature oxygen evaluation

Chapter 5: Results

5.1 INTRINSIC Ga₂O₃ THIN FILMS

The primary goal of the work focused on the intrinsic Ga₂O₃ films was to study the surface chemical composition and valence state, crystal structure, morphology, grain size and electronic properties as a function of deposition temperature. The chemical valence state and surface chemistry of the Ga₂O₃ films deposited under variable substrate temperature were analyzed by XPS. Samples were evaluated as-deposit and after performing Ne⁺ sputtering for 5 minutes to eliminate surface contamination. The XPS survey spectra recorded for as-grown and Ne⁺ sputtered Ga-oxide films are shown in Fig. 5. 1. The data are shown in the binding energy (BE) range of 0-1200 eV for two representative samples grown at RT and 500 °C presented in the upper and lower panels, respectively (Fig. 5.1). For the as-grown Ga-oxide films, all the spectral features, except the C 1s level, are attributed to the constituent element core levels or Auger lines. The C 1s signal is due to hydrocarbons adsorbed on the film surface during air exposure during transfer from the growth chamber to the XPS instrument. It should be noted that the C 1s signal is completely absent in the XPS spectra of Ne⁺ bombarded films for both the samples shown. This observation confirms the removal of hydrocarbon contamination from the surface. It is clear from the XPS data that the spectral components related to constituent elements become more intense as a result of ion-bombardment of the film surfaces. The absence of a Si substrate peak is due to the fact that the deposited Ga-oxide films cover the Si surface and are sufficiently thick to prevent detection of photoelectrons from the substrate.

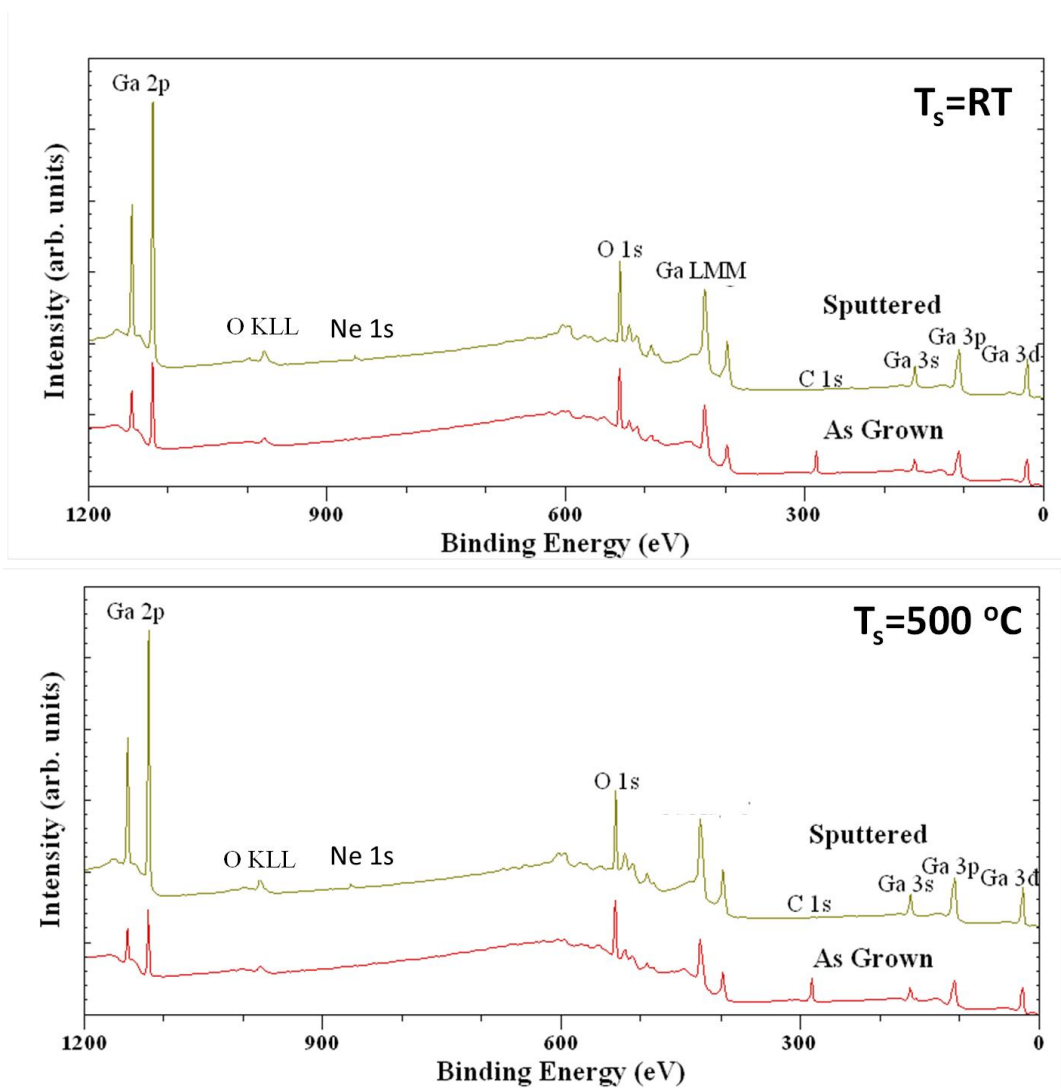


Figure 5.1: XPS survey scans of representative Ga_2O_3 films grown at different substrate temperatures. The survey scans obtained for films grown at RT (upper panel) and 500 C (lower panel) are shown (Ramana et al. 2014a).

The core level photoelectron spectra of the Ga 2p doublet are shown in Fig. 5. 2. The high resolution XPS spectra are shown for as-grown (left panel) and Ne^+ sputtered (right panel) samples. The binding energy (BE) values of these Ga $2p_{3/2}$ and Ga $2p_{1/2}$ peaks are 1118.0 and 1145.0 eV, respectively; they are almost constant and do not exhibit any change or shift as a function of substrate temperature during growth. Furthermore, no appreciable change is noted in

the BE values of these peaks in as-grown and Ne^+ sputtered samples. However, a very small variation in full-width at half-maximum is noted for these peaks in Ne^+ sputtered samples compared to as-grown samples. The BE values of Ga 2p levels for metallic Ga are: 1117.0 and 1144.0 eV for Ga 2p_{3/2} and Ga 2p_{1/2}, respectively, and are indicated by the dashed lines in Fig. 5.2. Compared to metallic gallium, the grown Ga-oxide films show a positive shift in the BE (1.0 eV). It should be noted that the BE shift occurs due to the redistribution of electronic charge around the constituent atoms. Therefore the differences in Ga chemical bonding cause a BE shift that can be used to extract information about the oxidation state of Ga in the grown films. Based on these considerations, it can be concluded that the chemical state of Ga in the films is in the highest valence state (Ga^{3+}) without any of the reported intermediate valence states.

(Ramana et al. 2014a).

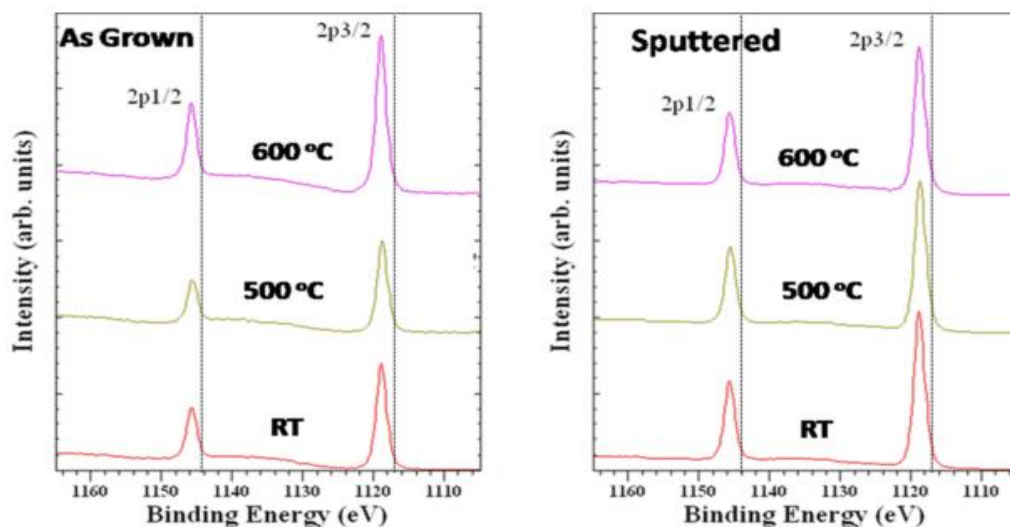


Figure 5.2: XPS spectra of Ga 2p peaks, a) left image shows as-grown spectra, b) right figure shows the spectra after Ne sputtering was performed (Ramana et al. 2014a)

The core level photoelectron spectra of O 1s also revealed interesting features about the surface chemistry of the grown Ga-oxide films. The high resolution XPS spectra of O 1s core levels are shown for as-grown (left panel) and Ne^+ sputtered (right panel) samples in Fig. 5.3. The

O 1s peak is asymmetric in as-grown samples. While the main peak is centered at a BE ~ 531 eV, there is a small shoulder at a BE ~ 532 eV. As shown in Fig. 5. 4 for a representative samples grown at RT, the O 1s peak for as-grown Ga-oxide films can be resolved into two components. The most intense peak is located at 531.0 eV and the less intense peak is at 532.3 eV, representing the different chemistries of oxygen. The less intense contribution at a BE of 532.3 eV disappears in all the samples upon Ne^+ sputtering of the surface. With Ne^+ sputtering of the surface, the O 1s peak changes into a single, sharp peak centered at a BE of 531.0 eV. These features can be understood as follows. It has been reported that the O 1s peak in Ga-oxide occurs at a BE ~ 531 eV, which characterizes Ga-O bonding with the highest oxidation state of Ga (Ga^{3+}). The less intense contribution at a BE ~ 532.3 eV can be attributed to either carbonyl (oxygen bonded to carbon) or hydroxyl (oxygen bonded to hydrogen) groups, which are adsorbed onto the surface.^{34,35} However, it was noted in the survey XPS spectra (not shown) that the C 1s signal was present on all of the as-grown Ga-oxide samples. The presence of C 1s disappeared upon Ne^+ sputtering of the surface. Based on these observations, it is clear that the minor contribution that appears in O 1s spectra is due to the surface C-O or hydroxide bonds, which disappeared on sputtering away the few top-most surface layers.

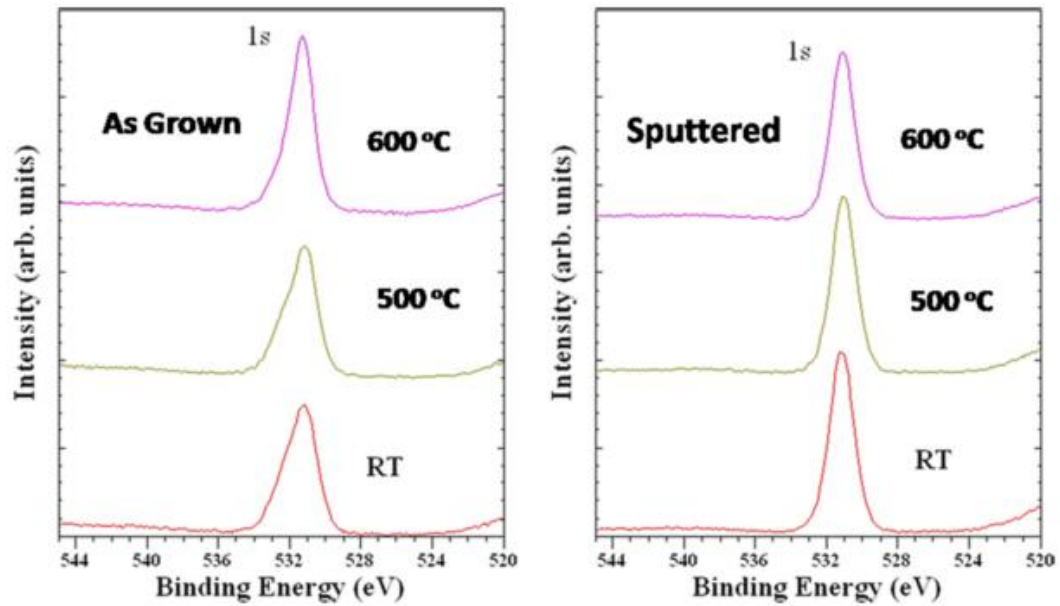


Figure 5.3: XPS spectra of O 1s peak, left image shows as-grown spectra, right figure shows the spectra after Ne sputtering was performed (Ramana et al. 2014a)

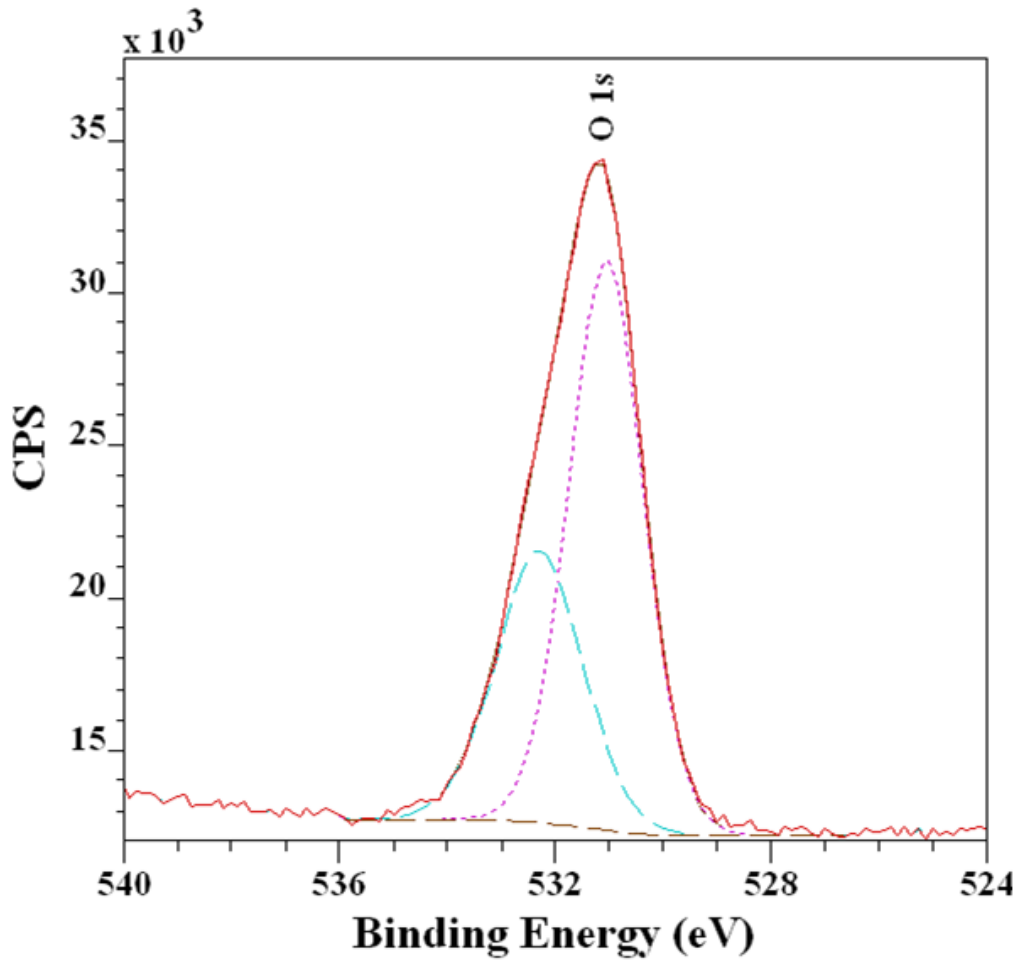


Figure 5.4: Peak fitting analysis of the O 1s core-level peak in as-grown Ga-oxide films fabricated at RT (Ramana et al. 2014a).

The AFM results for the Ga_2O_3 samples deposited at temperatures $\geq 500^\circ\text{C}$ are shown in Fig. 5.5. The topographic images are shown along with the corresponding 3D surface images. It is remarkable to note the evident nano-particulate morphology the film surfaces, where the conically shaped grains are distributed uniformly all over the film surface. Samples deposited at temperatures $< 500^\circ\text{C}$ (not shown) are mostly amorphous in nature and no crystalline grains are presented on the film surfaces. This observation is in agreement with the XRD data, which indicate that Ga_2O_3 films deposited at temperatures $< 500^\circ\text{C}$ were amorphous in nature while those at $\geq 500^\circ\text{C}$ are nano-crystalline. It is evident from Fig. 5.5 that the grain-size increases with increasing

growth temperature. The size increases from ~ 20 nm to ~ 32 nm with increasing growth temperature from 500°C to 600°C . The effect of growth temperature is also reflected in the case of root-mean-square surface roughness values, which increased from 1 nm to ~ 3 nm with increasing temperature from 500 to 600°C . The surface roughness values of the amorphous films were not significant. For instance, the set of films deposited at $<500^\circ\text{C}$ exhibit a surface roughness of <1 nm.

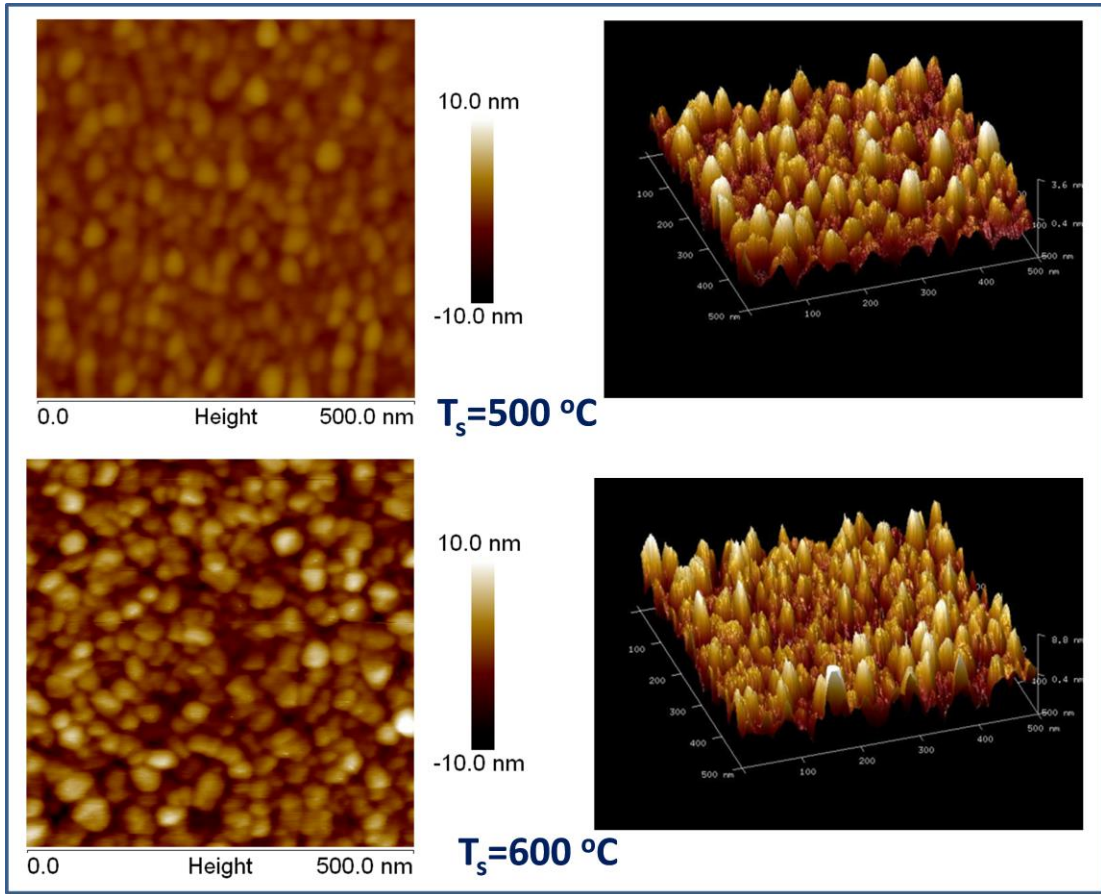


Figure 5.5: AFM images of sputter deposited Ga_2O_3 films; (a) sample grown at 500°C , (b) sample grown at 600°C (Ramana et al. 2014a).

Figure 5.6 shows the room temperature electrical resistivity of the Ga_2O_3 films fabricated at various deposition temperatures. Films grown at lower temperatures are seen to exhibit higher resistivity, the values being approximately $200\text{--}210\ \Omega\text{-cm}$ for films grown up to 300°C . A sharp

decrease in resistivity is observed for samples prepared at 400 °C. As the growth temperature increases, the resistivity is seen to decrease further. The sample deposited at 600 °C exhibits the lowest resistivity of 1 Ω -cm.

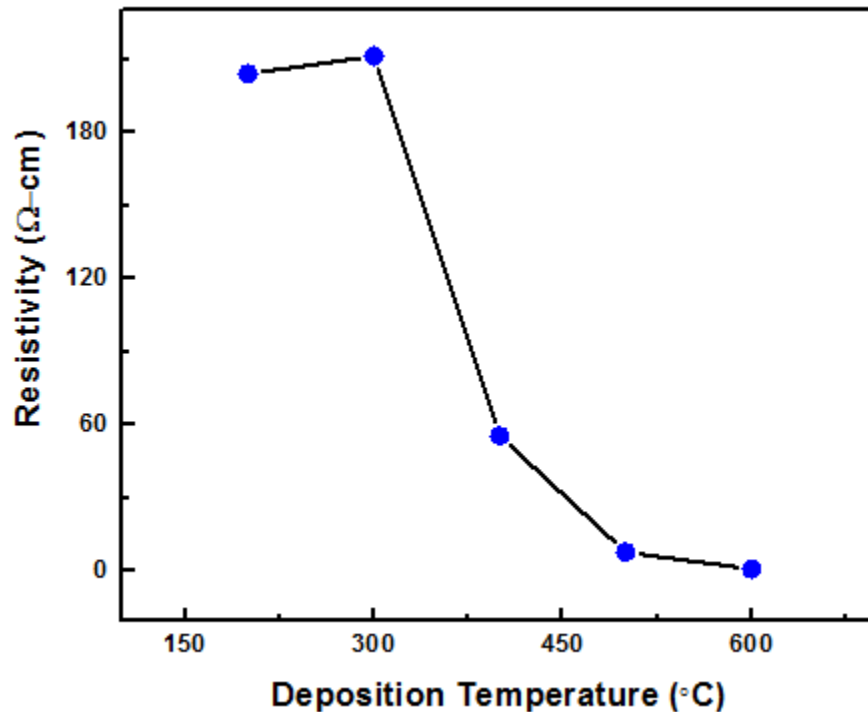


Figure 5.6: Electrical resistivity variation of Ga₂O₃ films with Ts (Ramana et al. 2014a).

Finally, while a detailed account of observed results and underlying mechanism are discussed in the next chapter, it will be helpful to summarize the data so that it will be beneficial to understand what the conditions employed to fabricate samples with W-incorporation into Ga₂O₃. Thus, the effect of deposition or growth temperature on the crystal structure, phase, grain size, and band gap of Ga₂O₃ films is summarized in Table 5.1. To describe briefly, Ga₂O₃ films deposited at RT-400 °C were amorphous (a-Ga₂O₃). A substrate temperature of 500 °C is critical to the onset of film crystallization with the β -Ga₂O₃ phase formation. Therefore, films deposited at ≥ 500 °C crystallize in the β -Ga₂O₃ phase. The grain size determined varied from 15 to 35 nm with increasing substrate temperature.

Table 5.1: Summary of the effect of growth temperature on the crystal structure, phase, grain size, and band gap of Ga₂O₃ films.

Substrate Temp. (°C)	Crystal Structure and Phase	Ga/O Ratio	Band Gap (eV)	Grain Size (nm)
25	Amorphous	1.6	5.17	-
200	Amorphous	1.6	5.02	-
300	Amorphous	1.5	5.01	14
400	Amorphous	1.5	4.98	16
500	Monoclinic (β -Phase)	1.5	4.99	20
600	Monoclinic (β -Phase)	1.5	4.96	35

5.2 OPTICAL PROPERTIES W-DOPED Ga₂O₃ FILMS

For the case of W-incorporated Ga₂O₃ films, the results obtained on the electronic properties, more specifically the optical characteristics, will be presented as there is a strong evidence for the significant changes due to W-incorporation. The structural and chemical analysis will be presented in subsequent sections. The optical transmittance spectra for the W-doped is presented in Figure 5.7 obtained by using UV-Vis-NIR spectrophotometry. Pure Ga₂O₃ and W-doped films deposited with 10 sccm of oxygen content showed to be highly transparent (~80%) for the evaluated light wavelength spectra, whereas the W-doped film deposited with 4 sccm of oxygen stills shows metallic behavior due to the lack of transmittance. When we

compare the transmittance spectra of Pure Ga_2O_3 vs W-doped films we can see that the absorbance edge moves towards the largest wavelengths, and that the overall transparency of the films is reduced, being the film deposited with the highest tungsten power ($P_w=100$ W) the least transparent film after 500 nm wavelength; nevertheless, still showing transmittance values higher than 80%.

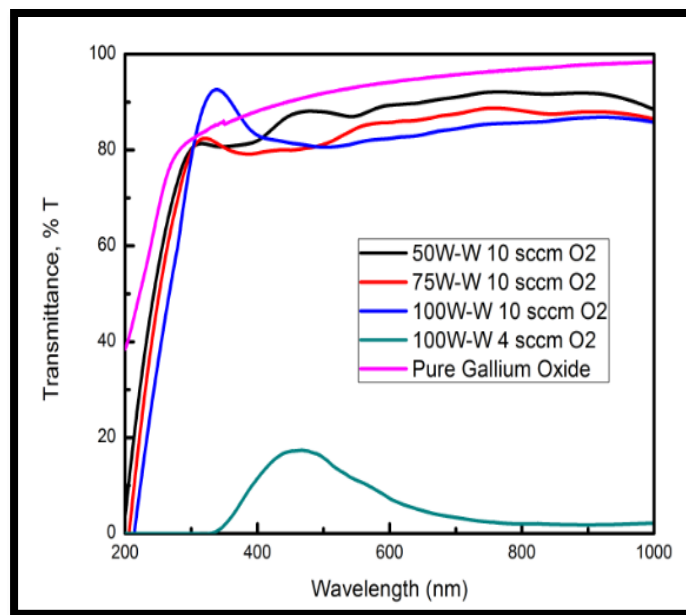


Figure 5.7: Transmittance spectra for Ga_2O_3 based thin films

The band gap of the films was calculated by using equations 4.7, 4.8, and 4.9. The $(ah\nu)^2$ vs $h\nu$ curves are showed as an insert in figure 5.5, a regression analysis and extrapolation of the high adsorption region, where the spectra behaves linearly, allowed us to determine the band gap at the point where $h\nu=0$. In this case Ga_2O_3 based films band gap can be calculated using direct band gap equations, and the E_g value for Pure Ga_2O_3 is $5.00 (\pm 0.03)$ eV. The E_g values were found decrease with increasing sputtering power to W target, and from chemical composition analysis (presented in the next section) the higher sputtering power corresponds to higher tungsten concentration of ~13%. The change in band gap values with increasing W-sputtering

power is shown in Fig. 5.8, which can be used to explain the effect of W-incorporation on the band gap. It can be noted that the E_g value decreases continuously with increasing doping of W-ions into the Ga_2O_3 based films. For the highest sputter-power used for this deposition ($P_w=100\text{W}$) to the W-metal target, the E_g value reduced significantly to $4.30 (\pm 0.05)$ eV. The shift in the bandgap of ~ 0.7 eV represents a substantial decrement in the band energy values of Ga_2O_3 when W is introduced.

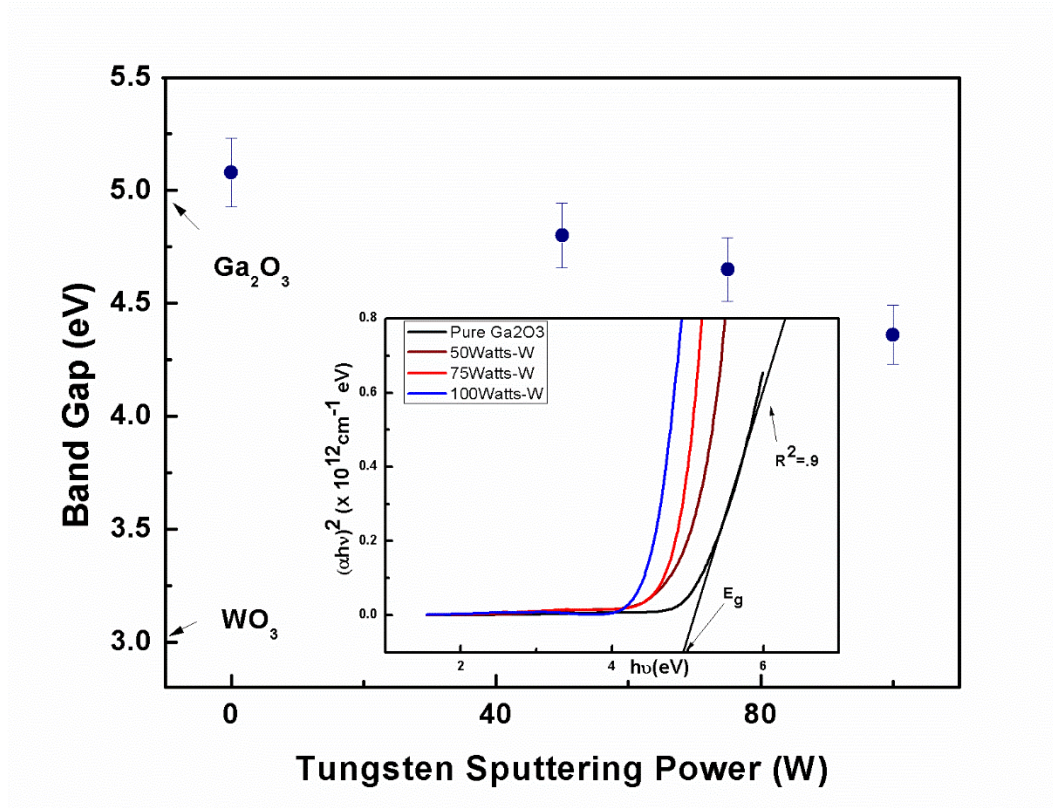


Figure 5.8: Band gap values of Ga_2O_3 based thin films as a function of P_w ; insert figures shows $(\alpha h\nu)^2$ vs $h\nu$ plots with integrated linear regression for band gap calculations

The refractive index values were evaluated using SE technique. The spectral dependencies of the experimental parameters obtained from SE measurements, Ψ and Δ , are plotted in Figure 5.9 for the Power dependent W-doped Ga_2O_3 films deposited on Si(100) substrates. The curves obtained

for Ga₂O₃ based films indicate good agreement between experimental and simulated data; the MSE values are presented in Table 5.2. The behavior of the curves is highly influenced by the variable W-sputtering power.

Table 5.2: MSE values for Ellipsometry Spectroscopy simulated curves

W-Power (Watts)	0	50	75	100
MSE	2.924	2.924	2.924	2.924

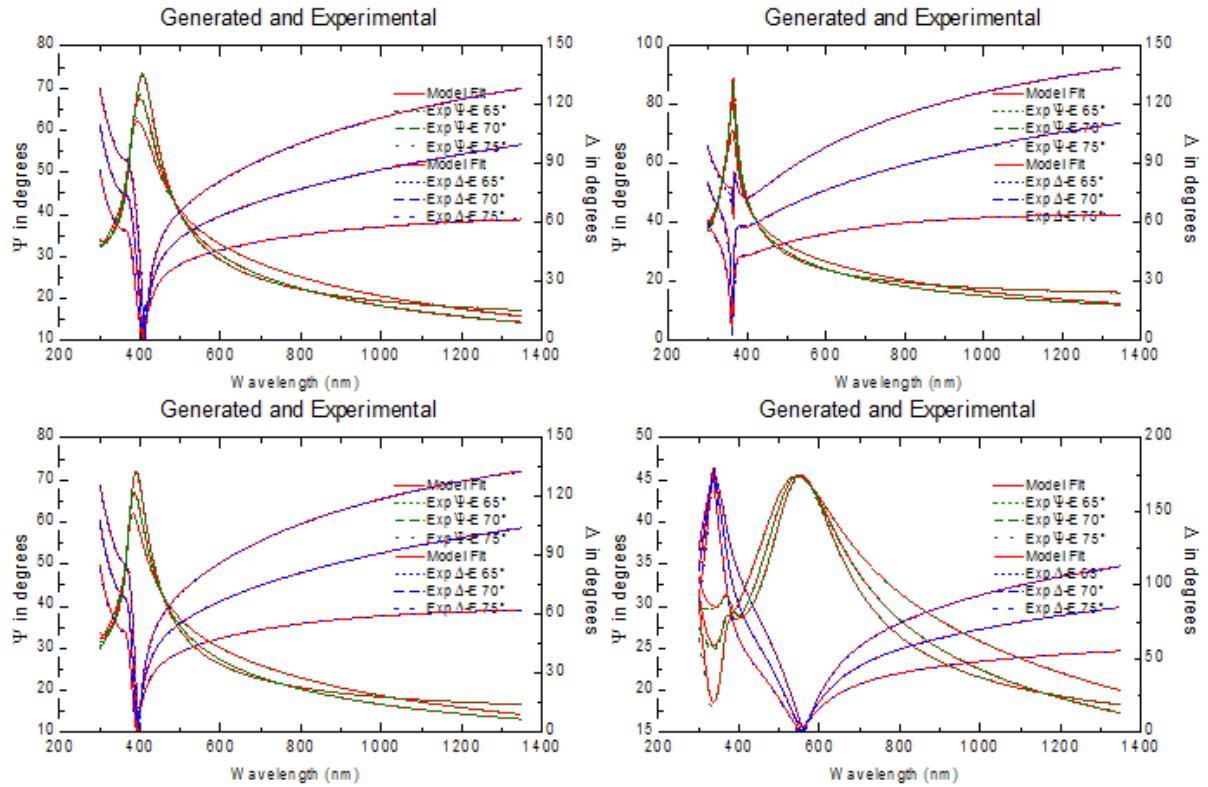


Figure 5.9: The spectral dependence of Ψ and Δ for Ga₂O₃ films grown at various temperatures.

The experimental data obtained and modeling curves are shown

The dispersion profiles of $n(\lambda)$ determined from SE data for the Ga₂O₃ based films are shown in Figure 5.10. At short wavelengths (>500 nm) the dispersion curve shows a sharp decrement

corresponding to fundamental absorption of energy across the band gap. However, the effect of tungsten incorporation is clear in the dispersion curves, where there is an increment in overall “n” values with increasing W-sputtering power. In order to further study the effect of W-incorporation on the optical constants of the Ga_2O_3 films, the values of the refractive index at $\lambda = 550$ are discussed, and the variation on the “n” values at this regain is clearer. At a $\lambda = 550$ nm, the ‘n’ values increase from 1.9 to 2.0 with increasing W-sputtering power, being 1.9 the value for Pure Ga_2O_3 films and matching the values presented in the literature (Rebien et al. 2002). 1.93, 1.97, and 2.00 are the values of 50W, 75W and 100W of W doping, respectively.

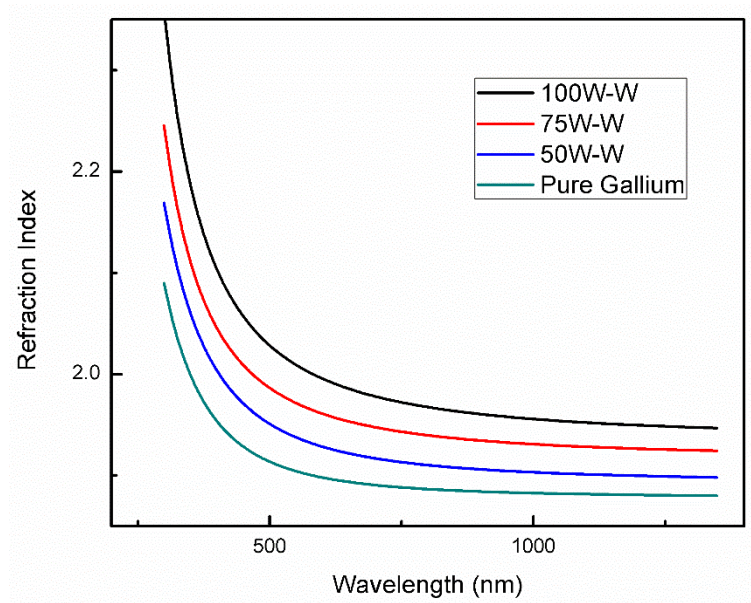


Figure 5.10: Refractive index curves extracted from ellipsometry simulations

5.3 CHEMICAL ANALYSIS W-DOPED Ga_2O_3 FILMS

Chemical composition analysis of the GWO co-sputtered samples made using Rutherford backscattering (RBS) confirmed the presence of W in all the samples. The RBS spectra of GWO films are shown in Figure 5.11. The data showed is for GWO films grown under variable W-sputtering power. The experimental and simulation data are shown. The backscattered ions observed were due to various elements in the films (Ga, W, O, Si) and their respective energy

positions are as indicated by arrows for the experimental spectrum. The scattering from W, the heaviest among the elements present in either the film or substrate, occurs at higher backscattered energy (1780 keV). Similarly, for Ga, the peak is located at the backscatter energy of 1580 keV as shown in the RBS spectra of GWO films (Figure 5.11). The measured height and width of the respective peaks are related to the concentration and thickness distribution of Ga and W ions in the oxide film and serves as a calibration check for composition and thickness since known Rutherford scattering cross section and experimental parameters can be used to calculate this height and width (Mudavakkat et al. 2012). As indicated in Fig. 1, the step edge and peaks due to ion backscattering from Si (substrate) and O atoms (film) are observed at 1100 and 660 keV, respectively.

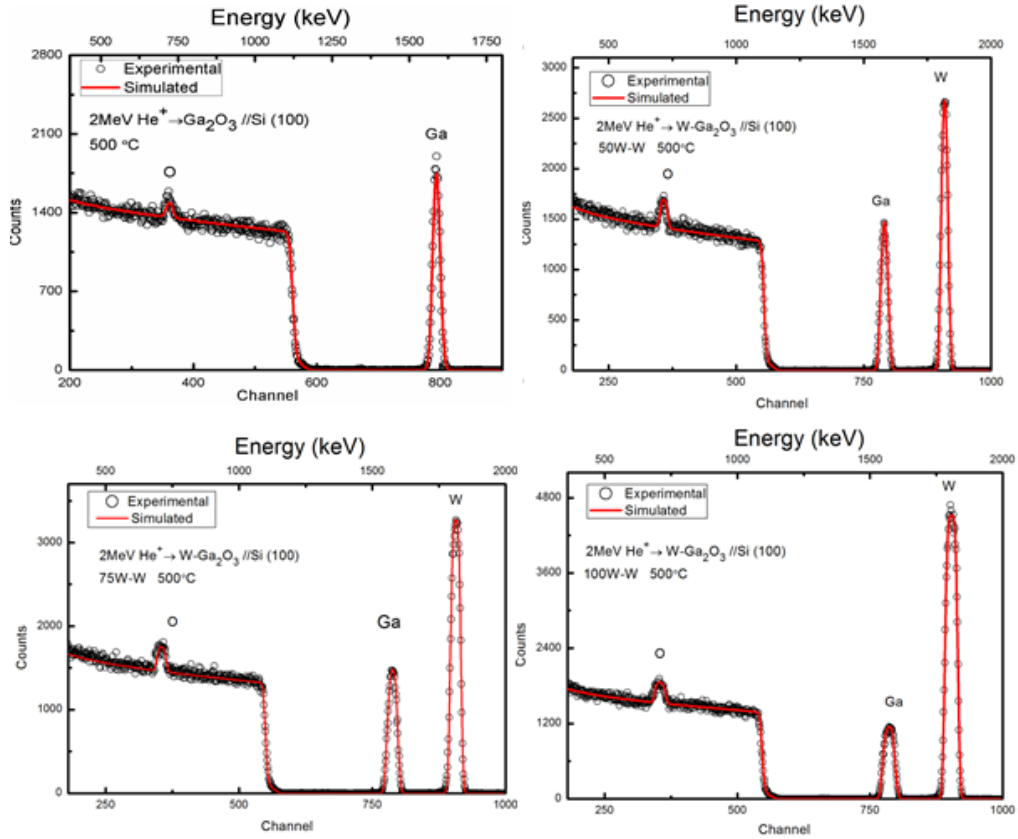


Figure 5.11: RBS spectra for as-grown Pure and W-doped Ga_2O_3 films deposited via rf-sputtering, including SIMRA simulations curves

The results obtained from the simulation of the RBS data indicate the increasing percentage of W in the films with increasing sputtering power, and are presented in Table 5.3. Variation of W-content in the films is shown in Figure 5.12, where film thickness variation with sputtering power is also presented. Since the time of deposition is constant, film thickness increases with increasing W-content. It is reasonable to expect such film thickness due to co-sputtering process under a set of fixed deposition conditions.

Table 5.3: Atomic content of W-doped Ga_2O_3 films obtained via RBS

Tungsten Sputtering Power (Watts)	Ga-Atomic Percentage (%)	W-Atomic Percentage (%)	O-Atomic Percentage (%)
50	26	8.4	66.6
75	24.1	9.5	66.4
100	17.1	12.5	70.5

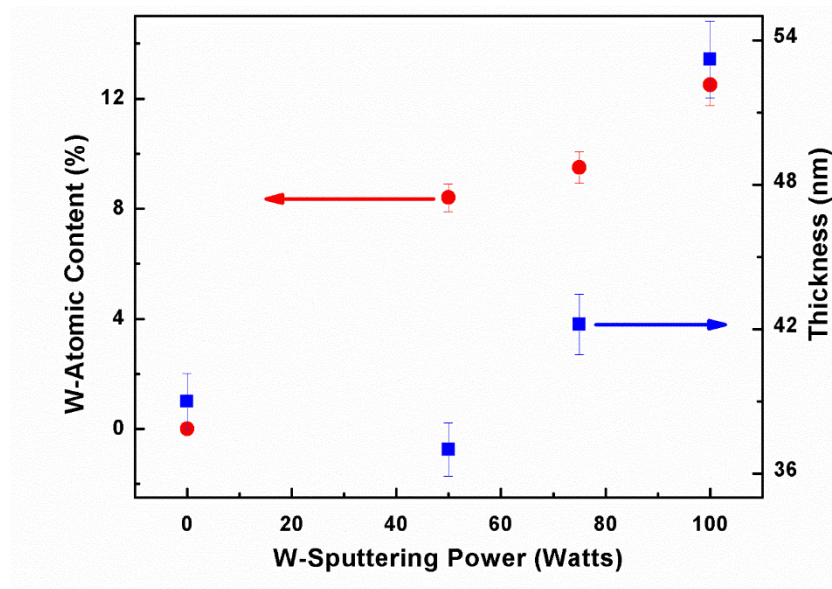


Figure 5.12: Thickness and W-concentration data as a function P_w use for rf-sputter deposition

X-ray photoelectron spectroscopy (XPS) measurements also allowed us to quantify the chemical composition of tungsten, gallium, and oxygen present in the films, as well as the chemical valence states of the constituent ions present in the GWO samples. The XPS survey spectra of representative GWO films are presented in Figure 5.13. The XPS spectra indicate that Ga, W, and O are the main constituents of the deposited films. The presence of C1s is evident in the survey spectra; the carbon peak in the XPS spectra is due to adventitious carbon from

exposure to air following fabrication, before being placed in the XPS system. Therefore, the spectra are calibrated to the C 1s peak at a binding energy (BE) of 284.6 eV. However, sputtering with Ar^+ ions fully eliminated the C 1s peak in the survey scans (not shown) which is a clear indication that the carbon is a result of adsorbed species on the film surface due to air exposure. The absence of a Si substrate peak is due to the fact that the deposited Ga-oxide films cover the Si surface and are sufficiently thick to prevent detection of photoelectrons from the substrate.

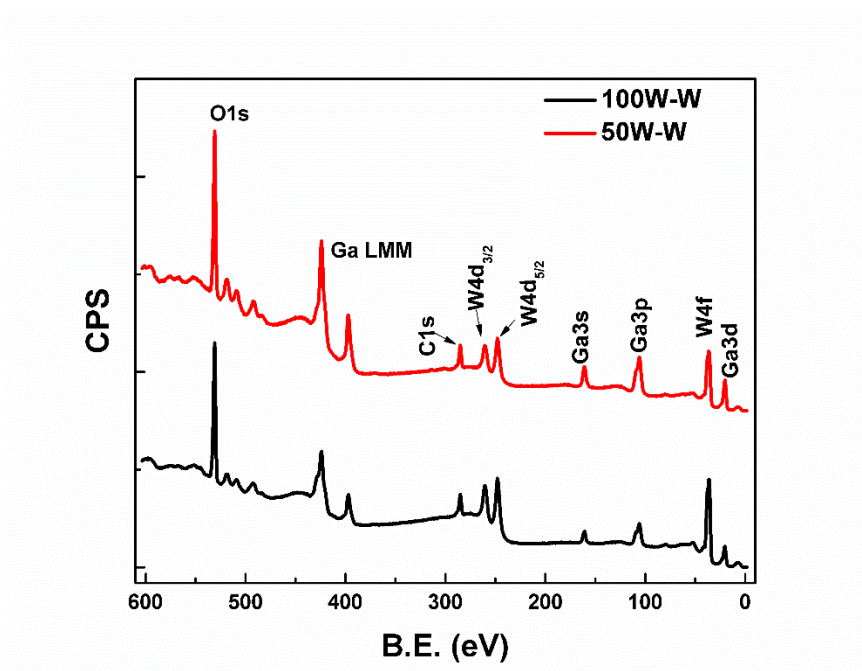


Figure 5.13: XPS spectra for W-doped Ga_2O_3 film deposited with $P_w=50\text{W}$ at 500°C , as deposited.

In order to determine the chemical states of the metal ions (W and Ga) present in the films, detailed analysis of the core level spectra of the main constituents was performed. Specifically, the high resolution scans of Ga $3d$, W $4f$ and O $1s$ were recorded and analyzed to obtain their chemical states and the interaction between respective metal ions and oxygen. The core-level XPS spectra of Ga $3d$ region are shown in Figure 5.14a. The data shown are for samples with variable W-content. It can be seen that the Ga $3d$ peak is located at a binding energy (B.E.) of ~ 20.5 eV. In

addition, Ga $3d$ XPS curve can only be fitted with a single and symmetric peak. Thus, the BE location of Ga $3d$ peak at ~ 20.5 eV accounts for the Ga-O bonds, where Ga ions exist in their highest oxidation state i.e., Ga^{3+} . It is also interesting to note that the Gd $3d$ peak is constant without any appreciable change in either peak shape or BE position, regardless the percentage of W-incorporation. This is an indication that the W-ions incorporated into gallium oxide matrix do not induce any appreciable changes in the chemical state of gallium ions, which exists in their highest oxidation state (Ga^{3+}). Compared to metallic gallium, the grown Ga-oxide films show a positive shift in the BE (1.0 eV). It should be noted that the BE shift occurs due to the redistribution of electronic charge around the constituent atoms (Ramana et al. 2014a).

The detailed core-level spectra of W $4f$ for GWO films are shown in Figure 5.14b. For GWO films without any incorporation of W-content i.e., intrinsic Ga-oxide films, no W $4f$ levels were seen (not shown). The XPS W $4f$ core-level peak exhibits a well-resolved doublet corresponding to W $4f_{5/2}$ and W $4f_{7/2}$ at the BE values of 37.8 eV and 35.7 eV, respectively. The W $4f_{7/2}$ peak at 35.7 eV in this work is in perfect agreement with the literature value of 35.7 eV characterizing the W^{6+} state in WO_3 (Yuzhi Zhang et al. 2009; Bertus et al. 2013). The BE location of W $4f$ along with W $4d$ indicates the W-O interaction in the matrix with W^{6+} chemical state as the dominant species for tungsten ions. However, the peak intensity of W $4f$ core-level is low for GWO films deposited with tungsten sputtering power of 50 W due to the fact that the concentration of W is low. It is noted that the peak intensity increases with increasing sputtering power to the W-target and, thus, increasing W-content in the GWO films. Similar to Ga $3d$ peak, no shift in the BE of W $4f$ peaks is noted with increasing atomic percentage of W incorporated in Ga_2O_3 matrix. However, it is noted that W $4f$ doublet exhibits broadening, which is an indicative of the fact that some of the W ions are not completely oxidized but exists in their lower valence

states such W^{4+} (Khyzhun 2000). The height of W $5d$ and W $4f$ peaks increase with incremental sputtering power for the W-target indication and increment on the atomic percentage of tungsten inside the films as showed in the RBS section.

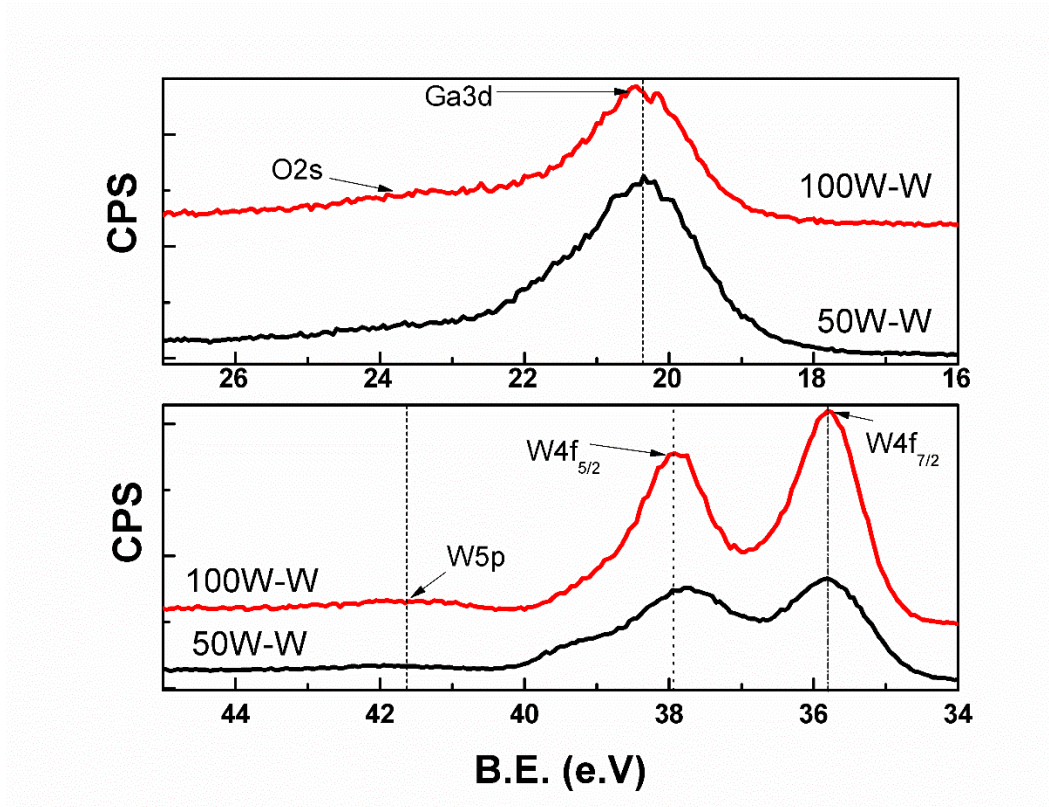


Figure 5.14: a) (Top) Ga3d high resolution spectra; b) (bottom) W4f peaks from high resolution XPS spectra for W-doped Ga₂O₃ films

The high resolution core-level XPS spectra of O $1s$ are presented in Figure 5.15. The data shown are as a function of variable W-sputtering power. The peak position for low concentration of W is located at BE~530.8 eV, which corresponds to the position of O $1s$ for Ga₂O₃ when gallium is present in its highest chemical valence state (Ga^{+3})(Ramana et al. 2005; Mudavakkat et al. 2012; Trinchì et al. 2004). The O $1s$ is observed to shift peak towards slightly lower BE side with increasing W-atomic concentration in the Ga₂O₃ matrix. Higher content of W shifts the peak to BE~530.6 eV, which is reported to be the characteristic of tungsten bonded with oxygen(BATHE

and PATIL 2008; Vemuri, Engelhard, and Ramana 2012). The core level photoelectron spectra of O 1s also reveals interesting features about the surface chemistry of the grown GWO films. Note that the O 1s peak is broader in the as-grown samples. In addition to the main contributions that can be attributed oxygen bonded to Ga and W, there is a small shoulder at higher BE side; the less intense peak located at 532.3 eV could be a representation of the different chemistry of oxygen. The less intense contribution at a BE ~532.3 eV can be attributed to either carbonyl (oxygen bonded to carbon) or hydroxyl (oxygen bonded to hydrogen) groups, which are adsorbed onto the surface (Riech et al. 2010; Shim et al. 2009). However, it was noted in the survey XPS spectra (Fig. 13) that the C 1s signal was present on all of the as-grown Ga-oxide samples. The presence of C 1s disappeared upon Ar⁺ sputtering of the surface. Based on these observations, it is clear that the minor contribution that appears in O 1s spectra is due to the surface C-O or hydroxide bonds, which disappear on sputtering away the few top-most surface layers. Thus, XPS analysis also allowed us to determine and corroborate the quantified tungsten content presented in the GWO films, as well as the chemical valence states of the constituents ions deposited. The overall concentration determined using RBS is in good agreement with the concentration of tungsten at the surface of the films probed using XPS. The overall concentration determined using RBS is in good agreement with the concentration of tungsten at the surface of the films probed using XPS.

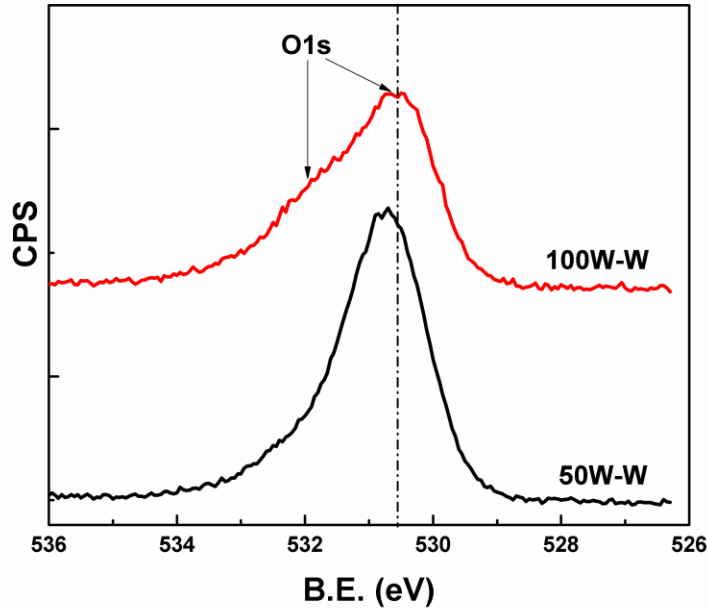


Figure 5.15: O1s high resolution XPS spectra for W-doped Ga₂O₃ films

5.4 STRUCTURAL ANALYSIS W-DOPED Ga₂O₃ FILMS

The GIXRD patterns of the GWO films are presented in Figure 5.16. The data are shown as a function of W-content in the films. It is evident that, with increasing W-content, the GWO films become amorphous. Intrinsic Ga₂O₃ films are nanocrystalline as seen in the XRD patterns. Also, our from regular XRD scans (not shown) results demonstrated the formation of crystalline GWO films under the variable W-content incorporation into Ga₂O₃ matrix; such films were all crystallize in the corresponding β -Ga₂O₃ phase. Furthermore, the GWO films exhibit the preferred (120) texture (Rubio and Ramana 2013a). However, in this case of GWO films, the surface structure was probed using GIXRD measurements. For intrinsic Ga₂O₃ films, peaks appeared in the GIXRD pattern indicating the crystalline nature of the GWO surface layers and the peaks identified still corresponds to monoclinic β -phase. However, no (120) preferred orientation is noted; however, the (512) peak located at $\sim 64.5^\circ$ was found to be the most intense peak. The other peaks noted are

(40-1) and (111) at $\sim 40^\circ$ and $\sim 36.5^\circ$, respectively (Goyal et al. 2014). This observation suggests that structure of the surface layers exhibit a different texturing compared to the overall structure of the bulk of the films (as previously reported(Vemuri, Engelhard, and Ramana 2012)) deposited on Si substrates. While W-incorporation maintains the overall crystalline nature of the bulk of the samples, the surface layers become amorphous as is evident in GIXRD patterns, where the patterns become diffuse with increasing W-content. We propose the following hypothesis to explain the behavior: the orientation preference in the bulk portion of the films is influenced by the interaction with the Si substrate and the surface free energy of it, which after certain thickness is eliminated, allowing crystal orientation to shifts as the films thickness is increased. In the case of W-doped the difference in surface free energies of WO_3 and Ga_2O_3 which inhibits their respective molecules to interconnect to each other, causing surface to show amorphous nature

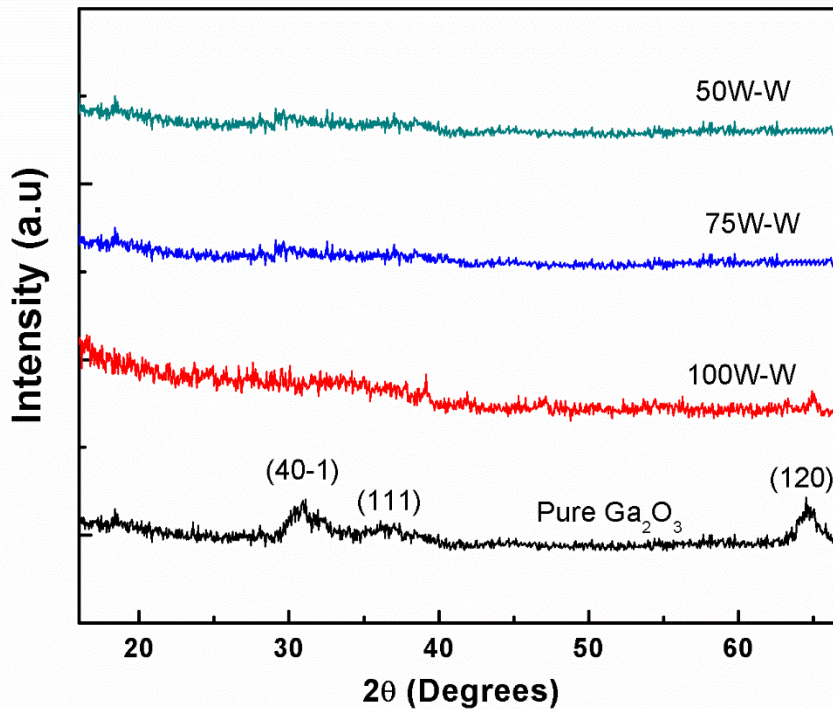


Figure 5.16: GIXRD spectra for W-doped Ga_2O_3 as-grown films

The SEM images indicating the surface morphology of intrinsic and W-doped Ga_2O_3 are presented in Figure 5.17. SEM images demonstrate the characteristic feature of granular morphology for intrinsic Ga_2O_3 films with an average grain size of ~ 25 nm. This observation is in good agreement with previous studies, where crystallization of Ga_2O_3 films is noted at a deposition temperature of 500°C (Kumar et al. 2013). The change in the surface morphology of the GWO films as a result of tungsten incorporation is evident in Figure 17. The film surfaces does not present agglomeration of grains and grain boundaries with increasing W-content. The surface of the W-doped films become smooth without any presence of granular morphology that is seen for intrinsic Ga_2O_3 films, with segregated or occasional grains on the surface suggesting lack of thermal energy to achieve full crystallization. This observation corroborates with the GIXRD results, where W-doped films showed the formation of amorphous surface layers.

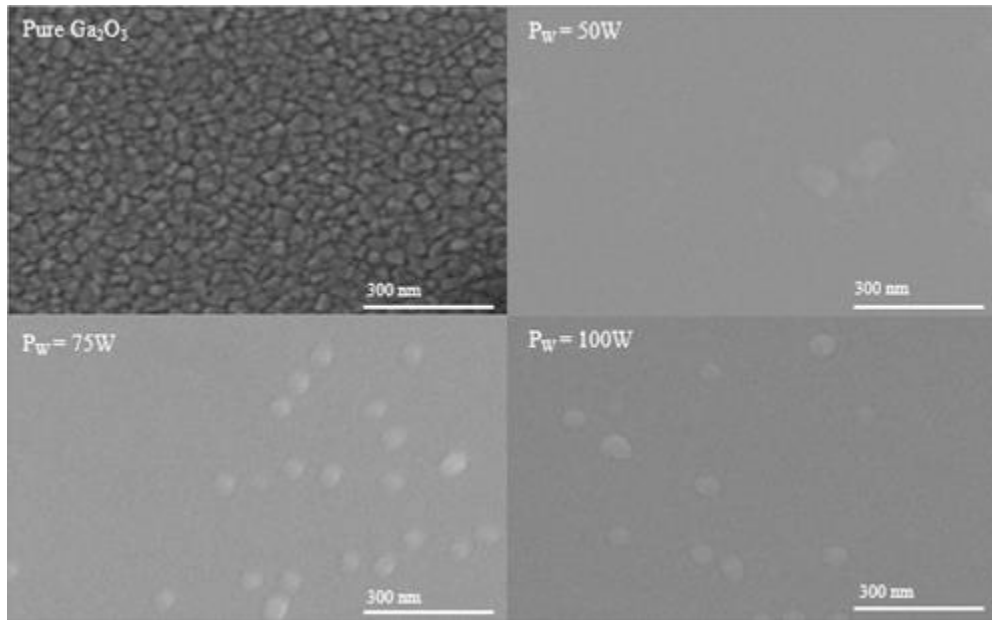


Figure 5.17: SEM micrographs for Pure and W-doped Ga_2O_3 films as a function of P_w

In the case of pure gallium oxide films the nanostructures were achieved at temperature of 500°C ; however, this temperature was not enough to achieve complete crystallization in the case

of W-doped films. Scanning electron microscope (SEM) revealed a small presence of localized grains at 500 °C without any order or patron to follow. Nevertheless when the temperature is increase the surface started transitioning towards fully granular. Figure 5.18 shows the SEM images for the samples grown with different substrate temperature and constant W-sputtering Power ($P_w=50W$). It was already mention the effect of tungsten into the surface morphology, retarding the crystallite growing, and allowing only localized grains. At the temperature of 600 °C the number of grains is increased, and evidence for the start of the grain agglomeration; however, isolated grains behavior is predominating. At 700 °C the grain size is increased, and the behavior starts to move towards formation of side-to-side grains, with less number of isolated nanocrystallites, and higher number of grains per surface area. 800 °C represents the final triggering temperature to achieve complete surface crystallization of the W-doped Ga-oxide films, at this point the entire surface is fully granular with an average dimension of ~30-40 nm, and shape resembling Ga_2O_3 grains, but the range of the grains dimensions varied from 10 nm to 80 nm.

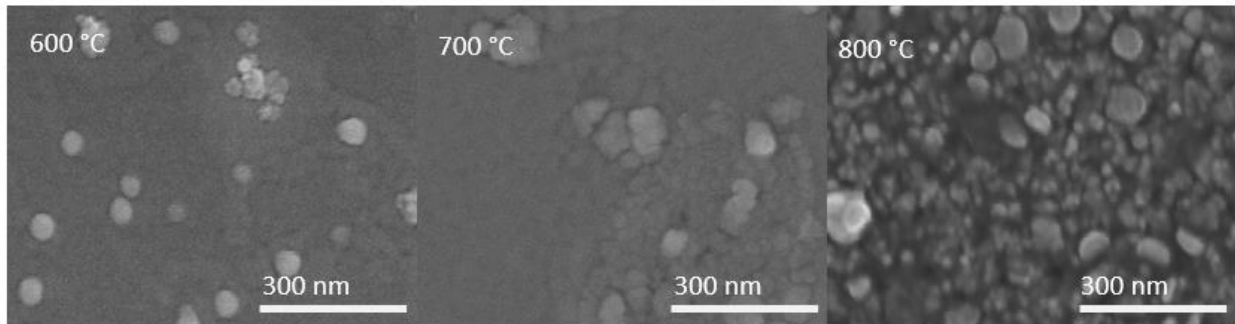


Figure 5.18: SEM micrographs for Pure and W-doped Ga_2O_3 films as a function of substrate temperature

5.5 THERMAL STABILITY W-DOPED Ga_2O_3 FILMS

Thermal stability of the GWO films was probed by a combined analytical and physical measurements of the samples subjected to thermal annealing. The RBS data of annealed GWO

films are shown in Figure 5.19. The data shown are for a variable W-content. It can be seen in the RBS spectra that the samples with higher W-content experience some changes in the peak shape and height of Ga and W. However, there are no changes observed for intrinsic Ga-oxide and GWO samples deposited with a W-sputtering power of 50-75 W. The most significant changes are noted for the samples deposited with 100 W sputtering power to the W-target i.e., the highest content of W in the Ga-oxide matrix. It can be seen in the RBS spectra of GWO samples that there is some degree tailing or shouldering effect at the left of the peaks Ga and W peaks; W-peak changes are most dominant. Such tailing or shouldering of the peak towards higher energy indicates the diffusion occurring at the interfacial region of the GWO film and Si substrate. As seen in Figure 19, this effect is much clear and dominant in W peak of GWO-100 samples. The interdiffusion of W is evident by tailing of the W peak at the interface coupled with some degree of Ga diffusion. In order to account for the observed changes and simulate the chemical structure changes, the RBS spectra were then fitted using SIMNRA by creating multiple layers with different composition of W, Ga, Si and O until the experimental data and SIMNRA calculated data match with each other inters of the tailing at the interface. In other words, the depth profile fitting has been adopted to verify the chemical composition changes across the interface by fitting the data. Clearly, intrinsic Ga₂O₃ and GWO-50 samples had sharp interface between film and the substrate with no varied concentration of W at varying depth of the film. The GWO-75 film shows very small or almost negligible intermixing layer as shown by the depth profile compared to GWO-100 film, which exhibits significant intermixing layer. The depth of W diffusion depends upon the concentration of total W-content in the GWO film. For instance, for GWO-75, the depth profile indicates that the W atoms diffused <1% in the Si substrate. But for GWO-100 sample, gradient of W in the intermixing layer is seen as it diffuses deeper in the Si substrate. Based on the

reasonable fit between experimental and calculated curves, the intermixing layer exhibits a W-gradient of 8.3% in the near interface, then 11.5% in between, slowly reaches 6%, and finally 2-3% before the Si substrate starts showing up without any indication of W.

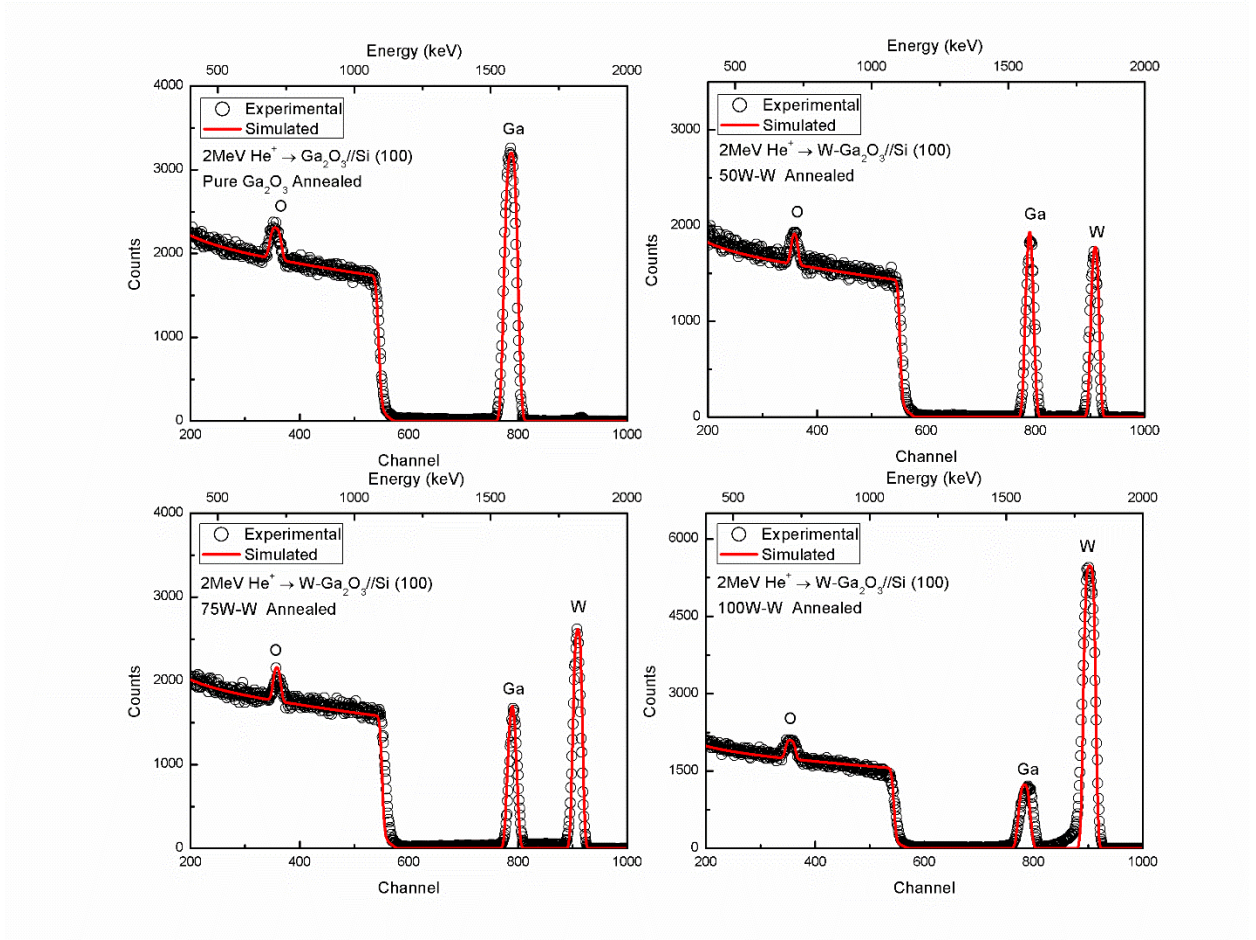


Figure 5.19: RBS spectra and simulated curve for GWO films after annealing

The surface chemistry analysis using XPS studies coupled with RBS provided additional information on the surface and interfacial chemical changes upon thermal annealing. The XPS analysis of the GWO samples was performed after annealing. The data are presented in Table 5.4. As seen from the XPS data in Table 5.4, the atomic percentage of W in all of the GWO films did not exceed 2%, the highest being in the films deposited with the highest P_w , irrespective of the overall content of W in the GWO films. The tungsten content in the films determined using XPS

are: 1 %, 1.7%, and 2% for GWO-50, GWO-75 and GWO-100 samples, respectively. However, as indicated by the RBS data and analysis, the corresponding W at% of the GWO-50, GWO-75 and GWO-100 films are 4.3%, 6.4% and 11.9%, respectively. Comparison of these results indicate that the W atoms in the surface layers of GWO films diffuse into Ga₂O₃ matrix; the interdiffusion seems proceeding from the surface towards the bulk portion of the films allowing the chemistry of the surface to diminish compared to the overall composition of the films, the mechanism of diffusion will be explained at the discussion section.

Table 5.4: Comparison of atomic percentage of RBS and XPS results

Tungsten Sputtering Power (Watts)	Ga-RBS (%)	W-RBS (%)	O-RBS (%)	Ga-XPS (%)	W-XPS (%)	O-XPS (%)
50	28.6	4.3	67.1	36	1	63
75	24.6	6.4	69	35	1.7	63.3
100	15	11.9	73.1	37	2	61

High resolution Core-level XPS data analysis has been performed on the annealed samples to determine the chemical state of Ga and W ions present in the GWO films. The data obtained for annealed GWO samples is presented in Figure 5.20 where the data are presented for GWO films with variable W-content. Similar to as-deposited samples, the XPS data indicates that the Ga, W, and O as the main constituents of the films. The core-level XPS spectra of Ga *3d* peak is located at BE~20.5 eV, which is same as the intrinsic Ga-oxide and as-deposited GWO films. No peak shift and other changes are noted for any of the films. Thus, the Ga *3d* results confirm that the gallium is present in its highest oxidation state i.e., Ga⁺³, which is stable before and after annealing.

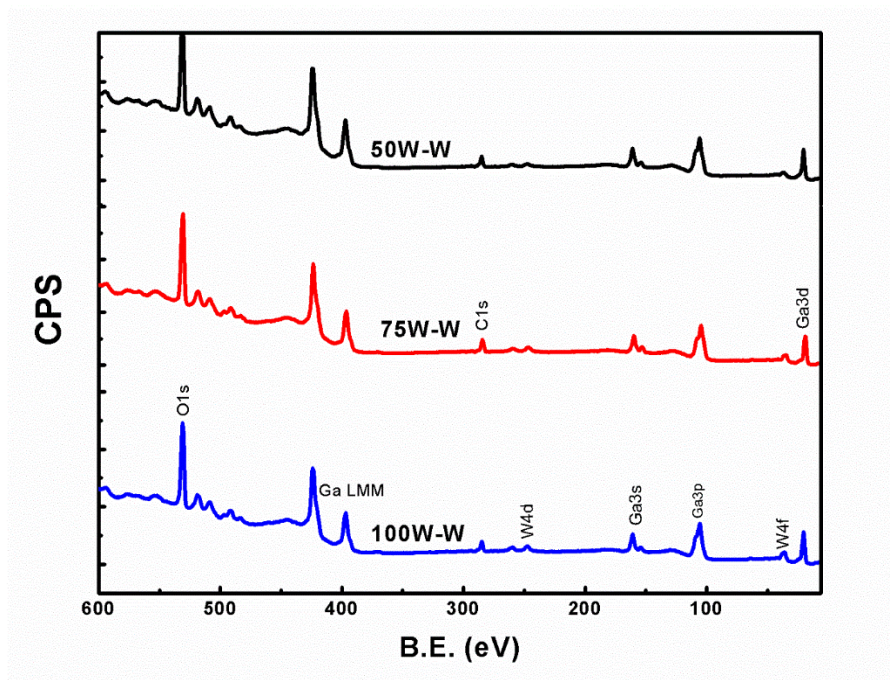


Figure 5.20: Core XPS spectra from 600-5 eV for W-doped Ga_2O_3 films as a function of P_w after annealing

The core-level XPS data of W $4f$ region for annealed GWO films are shown in Figure 5.21b. The spectra indicate the presence of W $4f_{7/2}$ and W $4f_{5/2}$, which are located at 35.8 and 37.9 eV, respectively. The location of the peaks matches those seen in as-deposited films with no significant shift in the peaks due to the annealing process, nor the content of tungsten doped into Ga_2O_3 . Peak positions matches with the reported values for WO_3 , and showing W^{6+} as the dominant specie for W inside the films. XPS results for the samples as-deposited show the presence of peak broadening, which corresponds to presence of secondary chemical valance state for non-stoichiometric WO_3 , after the annealing of the samples the secondary oxidation state contributions on the XPS spectra were not observed

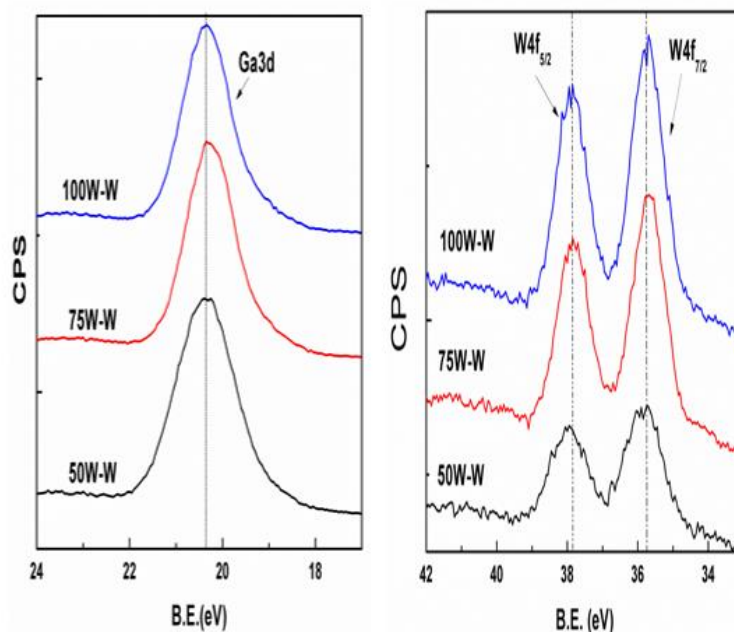


Figure 5.21: a) High resolution Ga3d XPS peak after annealing; b) High resolution W4f XPS spectra after films annealing

Similar to the results for as-deposited testing for the high resolution spectra for O *1s* showed peak shifting with increasing W atomic percentage as shown in Figure 5.22, where all O1s spectra are presented as a function of variable W-content. The position for the films with the lowest W-content is at BE~531 eV, which corresponds to the peak position for O *1s* when stoichiometric Ga₂O₃ is presented, and matches the position of GWO-50 as-deposited film(Ramana et al. 2014b; Geller 1960; Yamaga et al. 2003; Varley et al. 2010; Zinkevich and Aldinger 2004; Lovejoy, Chen, Yitamben, Shutthanadan, Heald, Villora, Shimamura, Zheng, Dunham, Ohuchi, et al. 2012; Encarnación G. Villora et al. 2008; Yijun Zhang et al. 2011b; Rubio and Ramana 2013b; Dakhel 2011; M. Mayer 1999; Ramana et al. 2005; Mudavakkat et al. 2012; Goyal et al. 2014; Trinchì et al. 2004). With increasing W-content the peak shifts towards a lower B.E. position, comparable with the occurred with as-deposit samples, this is due the influence of WO₃ interaction, for which the prefer O *1s* position is >530.6 eV(BATHE and PATIL 2008; Vemuri, Engelhard, and Ramana

2012; Riech et al. 2010; Shim et al. 2009). Nevertheless, it is important to mention that O 1s peak remained at the same position for GWO-75 and GWO-100 due to the similar surface W-atomic percentage in both samples. The presence of a peak broadening for O 1s in the B.E. levels indicates interactions with of the metal hydroxyl type, which is understood due to the exposure of the films to environmental air, and the annealing process perform in air(Azimirad et al. 2007; Naseri et al. 2007; Srinivasan and Miyauchi 2012).

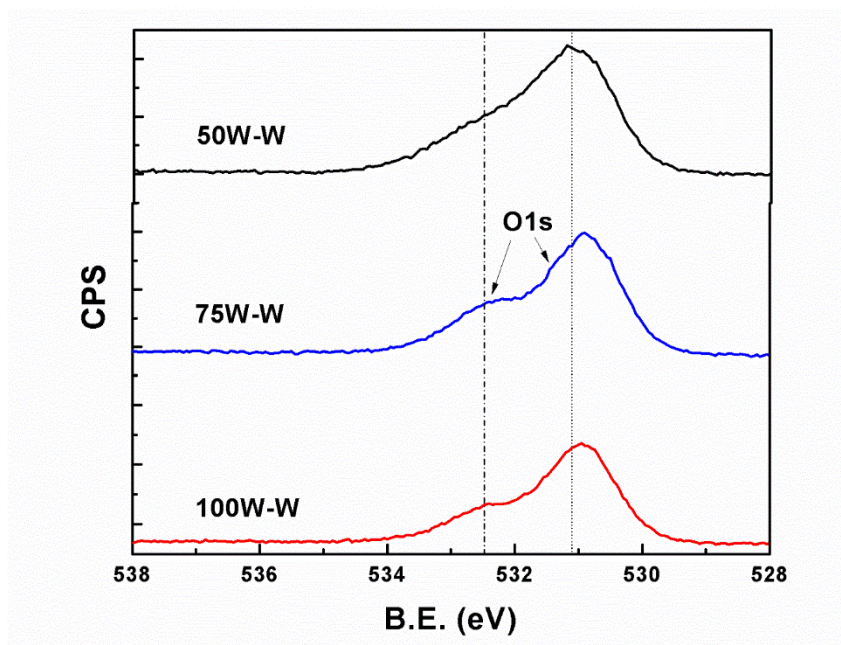


Figure 5.22: High resolutions XPS scans for O1s peak for W-doped Ga₂O₃ films as a function of Pw after the annealing process

The GIXRD spectra obtained for the GWO samples are shown in Figure 5.23. It is evident that all the patterns exhibit peaks indicating the crystalline nature of the samples. In the case of annealed intrinsic Ga₂O₃, the data show a similar crystal structure as the as-deposited samples, with peaks corresponding to β -Ga₂O₃. However, for W incorporated films, the patterns indicate crystal formation on the surface with contributions from both monoclinic Ga₂O₃ and monoclinic WO₃. The β -Ga₂O₃ phase was corroborated using JCPDS No. 00-041-1103 and monoclinic WO₃

corresponded to JCPDS No. 00-043-1035. Similar to what we are seen in as-deposited films, β - Ga_2O_3 shows preferred orientation on (40-1) and (512) planes at $2\theta \sim 30.8^\circ$ and 65.4° , respectively; the presence of these peaks is also observed on W-doped Ga_2O_3 films with no appreciable peak shift for variable W-content. Orientations (202), (111), and (-113) were also detected for β - Ga_2O_3 at $2\theta \sim 32.2^\circ$, 36.6° , and 55.8° , respectively, but no presence of (-113) appeared on W-doped films. All W-doped films showed presence of secondary phase formation of monoclinic WO_3 , with preferred orientations at (121) and (122) located at $2\theta \sim 29.5^\circ$, and 36.1° , respectively. Furthermore, presence of (220), (312), and (040) were also recorded for monoclinic WO_3 .

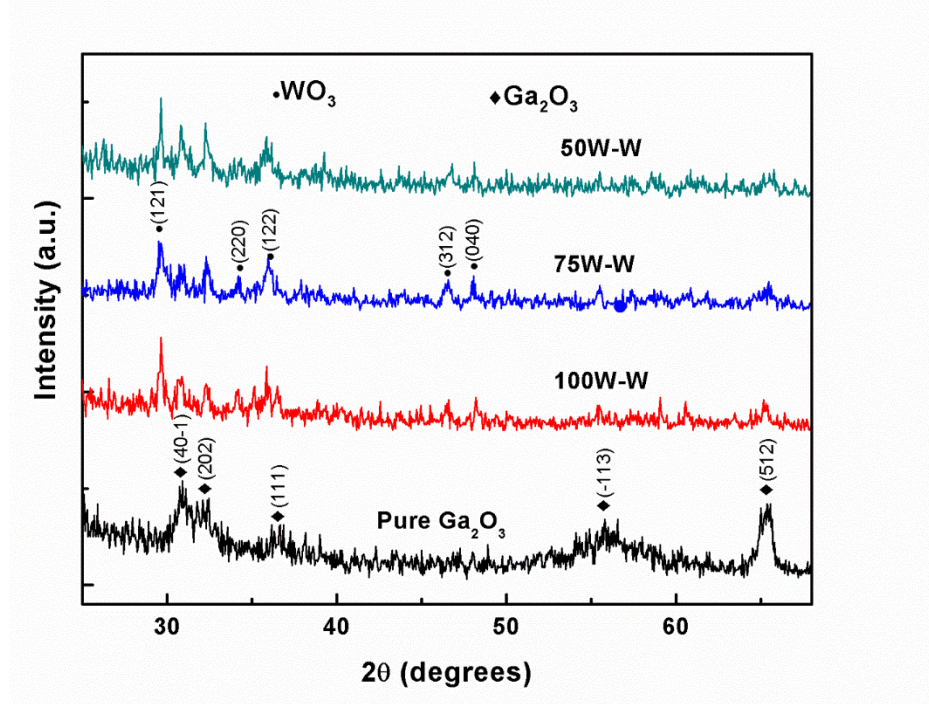
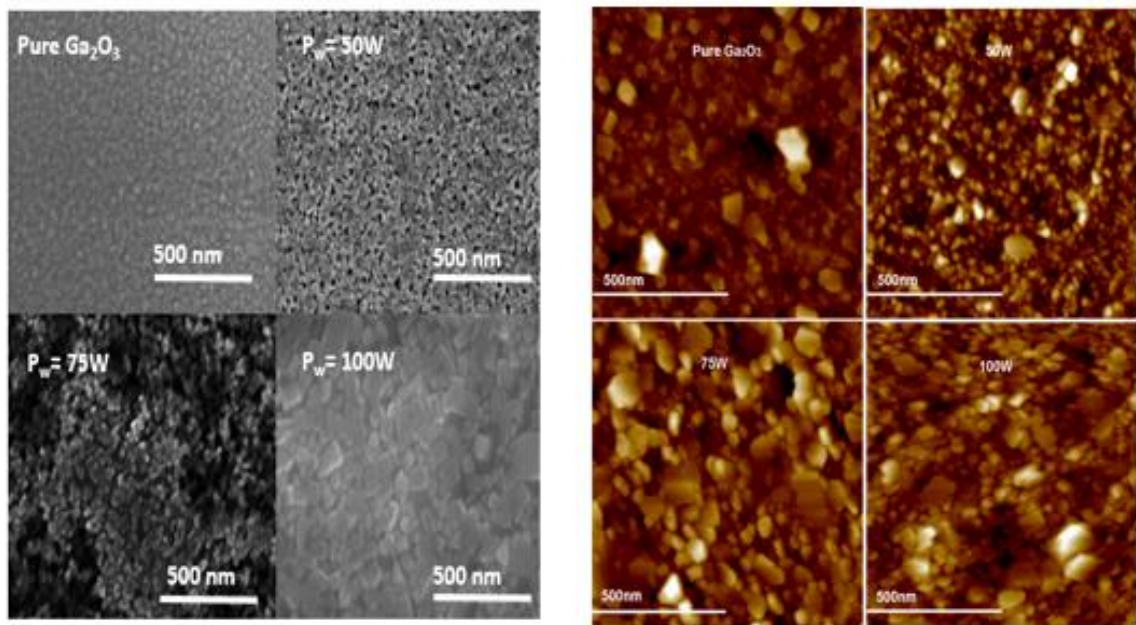


Figure 5.23: GIXRD plot for after annealing Pure and W-incorporated Ga_2O_3 films deposited via co-rf-sputtering

Surface morphology and topography data obtained from SEM and AFM are presented in Figures 5.24a and Figure 5.24 b, respectively. In complete agreement with the GIXRD results, the imaging analysis using SEM and AFM data, film surfaces demonstrated the granular morphology.

The topographic images the GWO surfaces show crystallites formation all over the film surfaces. It is also observed the formation of pores in the surface of the films. SEM and AFM data agree with each other in term of grain size and pore formation. The average grain size of the films changes with W-content. Grain size of 38 nm is noted for intrinsic Ga-oxide films while increasing W-content first decreases the grain size and then increases rapidly at higher W-content. The grain size decreased to 32 nm and then rapidly increases to 46 nm for the GWO-100 films, which contain the highest W-content. The change in surface morphology was better appreciated in W-doped films, where the change from amorphous to granular surface was observed; nevertheless, the formation of pore was also presented with the annealing process.



Figures 5.24: a) SEM micrographs for Pure and W-doped Ga₂O₃ films as a function of P_w after annealing, b) AFM topography images for Pure and W-doped Ga₂O₃ films after annealing

The W-doped Ga₂O₃ films analyzed after exposure to a post-deposition annealing for 1 hour at 900 °C where a change in the crystal structure and morphology was observed. Nevertheless, the intended application for this films requires the stability to temperature higher than 900 °C for

several hours of operation. In this case the Pure and W-doped Ga_2O_3 films were exposed to several cycles at 900 °C with increment on the time period. The films were evaluated via Scanning Electron Microscopy (SEM) in order to determine the surface quality of the film and that the grain structure are presented after all the heat exposure periods. For this experiments three samples were chosen to identify any possible failure due to heat exposure or any morphological modification that could provide false response on the films. Pure Gallium Oxide film (Fig 5.25a) demonstrated to be heavily stable at higher temperatures without any change on the morphology of the surface of the film even after 15 hours of continuing heat exposure. In the case of W-doped films the already reported change in surface morphology is presented in the films from as-deposited condition after 1 hour of annealing at 900 °C, where nano-grains are encountered in the surface along with vast number of porous. The crystallization is attributed to the high thermal energy introduced to the films allowing self-diffusion of the ions inside the film, and the appearance of porous on the surface is a result in the change on the internal chemistry of the material. Nevertheless, it is important to mention that the original change is preserved, and that the films does not produces any further change with the cyclic process of heat treatments. No change is visible in the grain size of the pores dimensions. Figure 5.25 represents the SEM images for the surface morphology of the different samples tested, where the thermal stability of the samples is observed throughout all the hours of heat exposure. The heat treatment was carried at 900 °C for several hour of exposure, starting at 1 hour and increasing the treatment by 1 hour intervals for the first 5 hours, after that, increments of 5 hours were carried until the goal of 15 hours was reached. The three samples were chosen for the following reasons: Pure Ga_2O_3 films as the standard material and in order to compare the stability of the pure films versus the films containing tungsten. 50W of tungsten sputtering power at 800 °C as the substrate temperature in order to compare fully

crystalline Ga_2O_3 films versus a fully crystalline W-doped film, and a 50W of tungsten sputtering power at 500 °C as the substrate temperature to include a sample that was not crystalline as-deposit, but contained tungsten into the lattice of Ga_2O_3 .

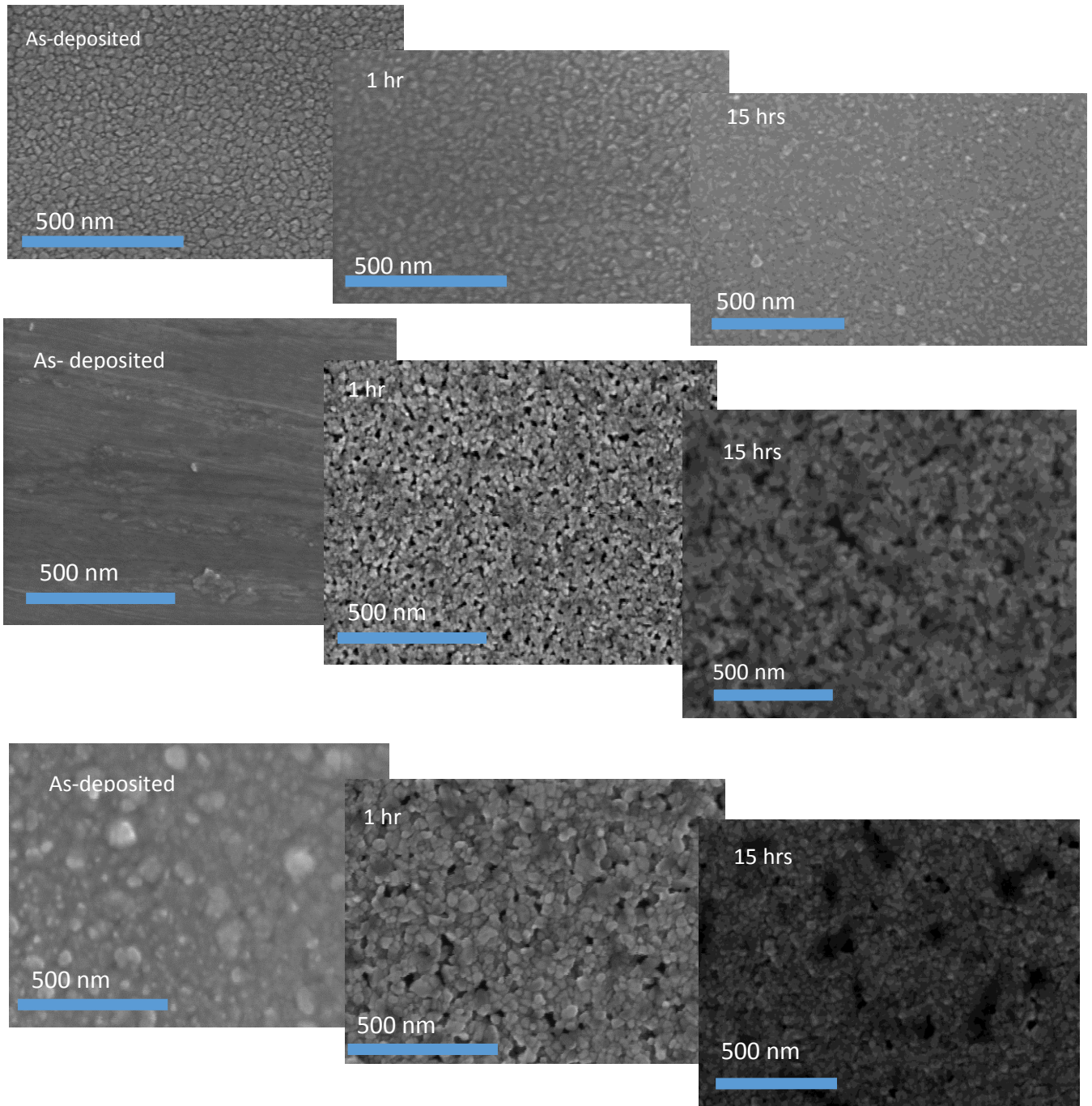


Figure 5.25: SEM micrographs of long period exposure to 900 °C for a) (top) Pure Ga₂O₃; b) (middle) W-doped Ga₂O₃ films deposited with P_w=50W at 500 °C; c) (bottom) W-doped Ga₂O₃ films deposited with P_w=50W at 800 °C

5.6 MECHANICAL PROPERTIES

Mechanical characterization of metal oxide based nanostructured sensors in has not been properly understood in the literature, the evaluation of the young modulus and hardness values of the system will help us to maximize lifespan of the system whenever mechanical load and thermal stresses are applied, especially under the reported drift due to the presence of cracking. Figure 5.26 shows an example of the load-displacement curve obtained from evaluating the mechanical properties of Ga₂O₃ based films. The films tested were deposited on top of a silicon substrate and annealed at 900 °C for 1 hour to maximize crystallinity.

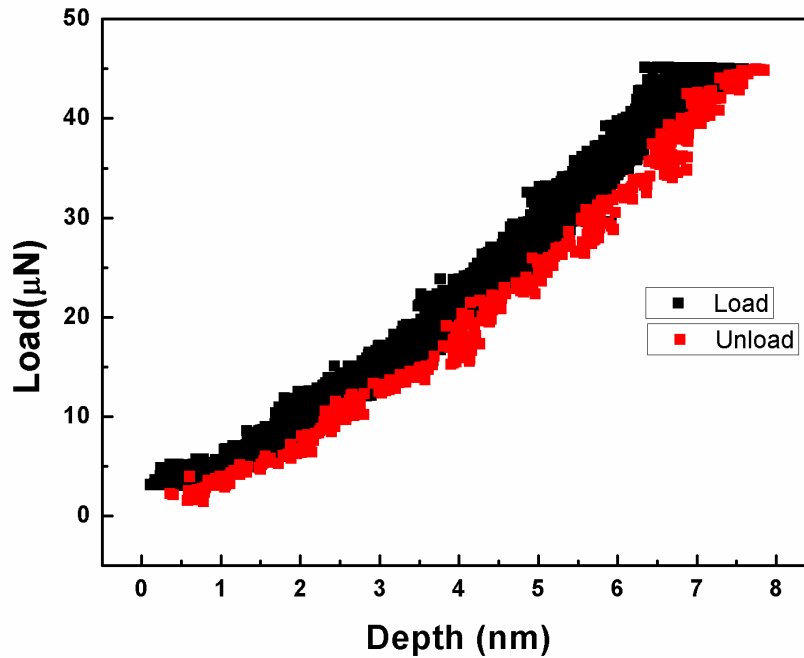


Figure 5.26: Load and unload curve for Pure Ga₂O₃ thin films versus indentation depth.

The values for hardness and elastic modulus for pure Ga_2O_3 are 3.01 GPa, and 78 GPa respectively; with initial incorporation of W ($P_w=50\text{W}$), the values of the mechanical properties decrease, similar the occurred to several other parameters such thickness, or in the case of resistance (not shown). The values of the hardness and elastic modulus for the sample deposited with $P_w=50\text{W}$ are the followings: $H= 2.95\text{GPa}$, $E= 70\text{GPa}$. When the films are exposed to higher levels of W-doping, the mechanical properties start to increase as we can see in Figure 5.27 where the Hardness and Young's Modulus values for W-doped films are presented. After the initial decrement with $P_w=50\text{W}$, the films showed to be strengthened by the addition of tungsten. The maximum hardness values and elastic modulus achieve in this investigation was achieved when the films were deposited using $P_w=100\text{W}$, where the values obtained are $H=3.25\text{GPa}$, and $E=132\text{GPa}$. It is important to mention that the evaluation of the mechanical properties was performed on the films after exposing them to the high temperature heat treatment of 900°C for 1 hour.

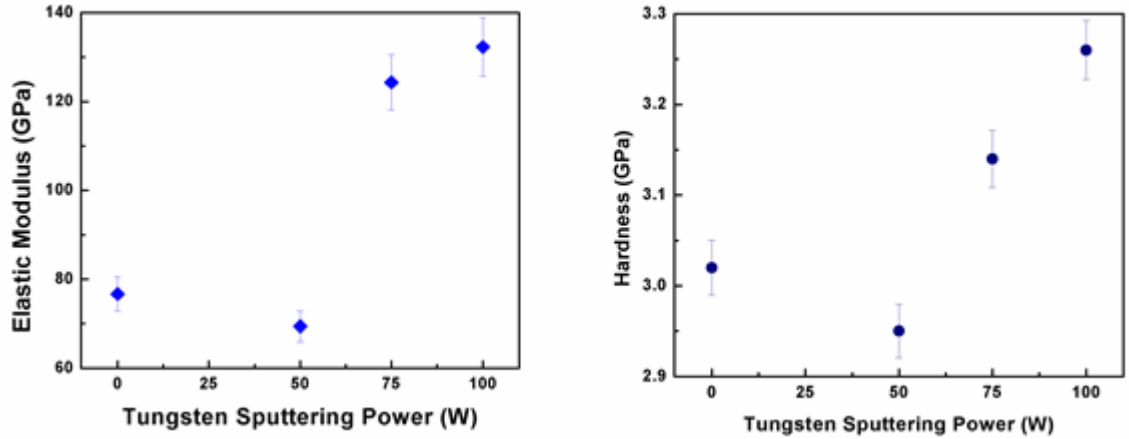


Figure 5.27: Hardness (left) and Elastic Modulus (right) values of Ga_2O_3 based thin films as a function of tungsten sputtering power

5.7 OXYGEN SENSOR CHARACTERISTIC

The initial oxygen sensor was performed using the line set-up method where two electrodes were attached to the surface of the films. The electrodes were adhered ~5mm apart from each other. The initial test was performed with the intention of determine the effect of tungsten doping in the time response of the films, which the improvement of this feature is one of the premises of this work. Figure 5.28 shows the initial testing for gas sensors where 4 graphs are presented, and the time response that each one showed is included. The time response was calculated by accounting the time that takes to complete 90% of the overall change in resistance. The time response for pure gallium oxide and for the film deposited with the highest content of W showed similar values of 36 seconds. Nevertheless, when the films are deposited with $P_w = 50$ and 75 Watts, the time response significantly improves, to 15 s and 20 s, respectively. It is also important to mention that Pure Ga_2O_3 films showed n-type semiconductivity by increasing the resistance value whenever the oxygen partial pressure was increased, whereas the W-doped films showed p-type semiconductivity when oxygen interacted with the films by reducing their resistance values.

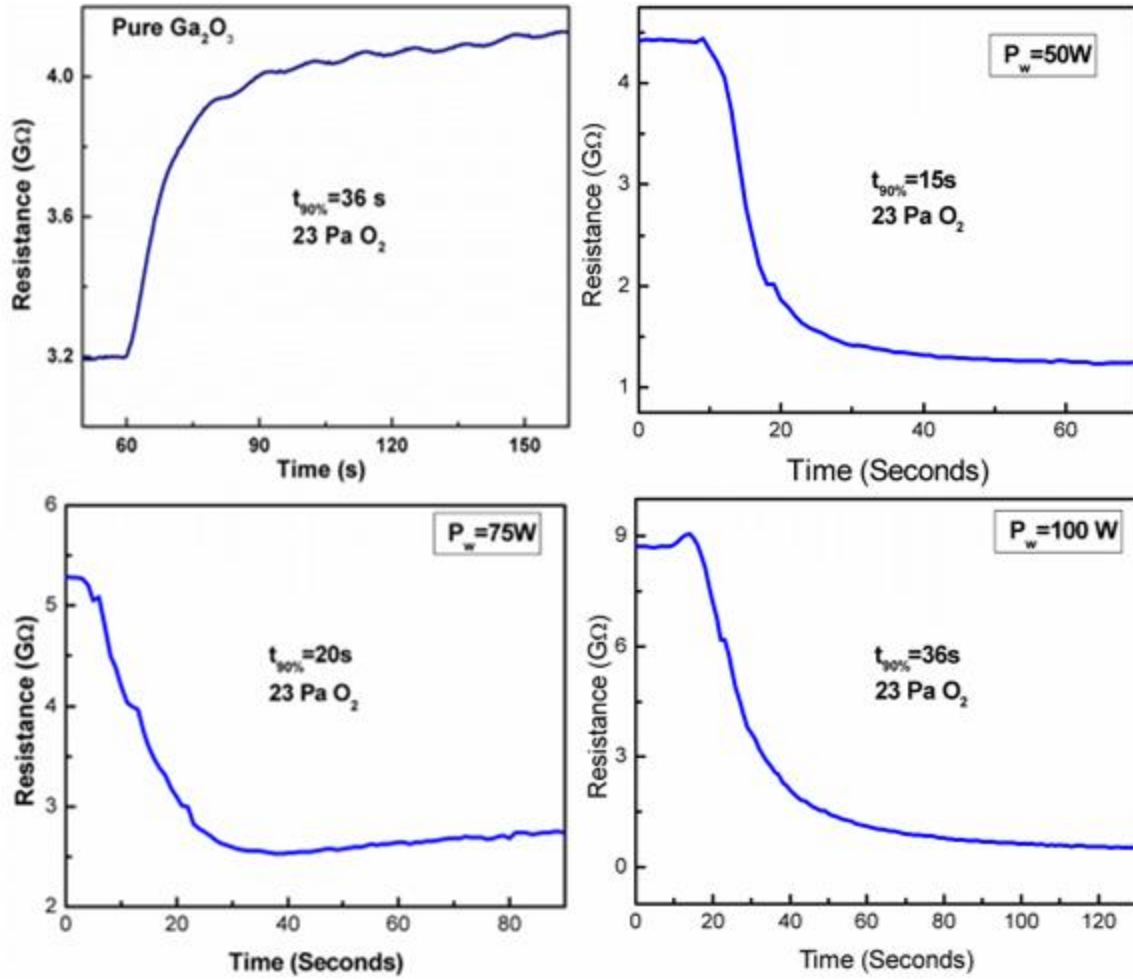


Figure 5.28: Oxygen sensor response of in-line setup for Ga_2O_3 based films deposited on Al_2O_3

After the initial time response testing, the focus towards improving the oxygen sensor characteristics of Ga_2O_3 films was directed towards the lower doping region by depositing the films with low P_w . The films evaluated were deposited onto Pyrex glass substrate with integrated interdigital electrodes. The initial testing was performed to determine the activation energy of the films with respect to oxygen, and calculated by using the slopes of the Arrhenius plot as shown in Figure 5.29 which follow a linear behavior and by implementing the following equation, the value could be obtained:

$$R = R_{\infty} \left(\frac{E_A}{kT} \right) \dots\dots\dots 5.1$$

Where R_{∞} is the resistance at infinity temperature, E_A is the activation energy, k is the Boltzmann constant, T is the absolute temperature, R is the resistance (Bartic, Ogita, et al. 2007). The value of the activation energy reduces as a function of W-incorporation, which was expected due to the reduction of the band gap values originally studied at the optical properties section. The intrinsic value for Ga_2O_3 films was 1.8 eV which correspond to the values obtained in the literature (Bartic, Ogita, et al. 2007), and reduced to a final value of 1.4 eV when the highest concentration was utilized at $P_w=100\text{W}$. This indicated that the energy required for oxygen detection is reduced by the incorporation of W-ions, which can be explain from the sensitivity point of view. Sensitivity react as a bell-shape curve, finding its maximum value at a specific temperature and reducing if the temperature increases or decreases; when W is incorporated to the films, the temperature for the maximum sensitivity is reduced due to the reduction of the activation energy values (Korotcenkov 2007).

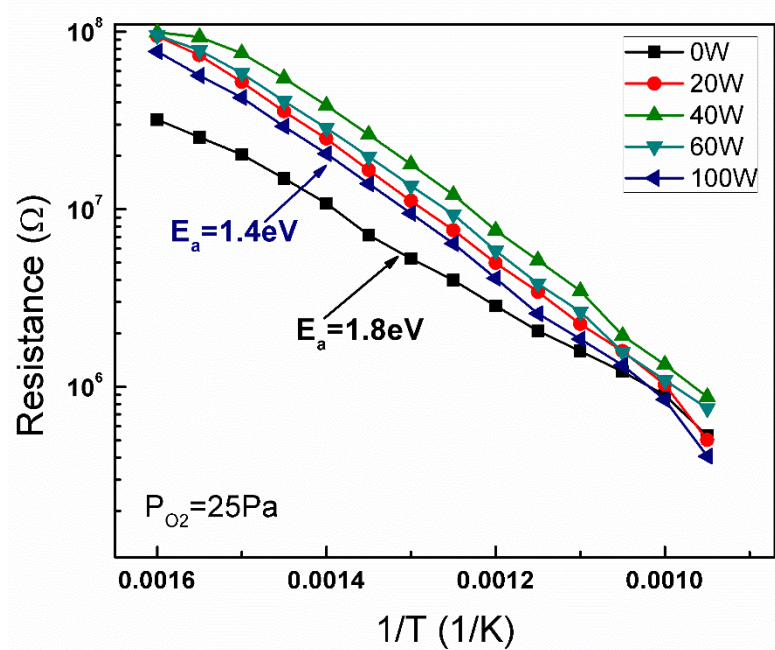


Figure 5.29: Arrhenius plot for Ga_2O_3 based thin films as a function of W-sputtering power

The sensitivity and time response of the Ga₂O₃ based oxygen sensors using Pyrex glass with interdigital electrodes. Figure 5.30 shows the comparison between pure and W-doped Ga₂O₃ films in terms of initial time response and sensitivity to 25 Pa of O₂ at 800 °C. The sensitivity was calculated by:

$$S = R_a/R_g \dots\dots\dots 5.2$$

Where S is the sensitivity, R_a is the resistance when the films is exposed to Ar, and R_g is the resistance when Oxygen is introduced. Similar to the results presented with the line set-up sensors, Pure Ga₂O₃ and the films deposited using 100W of W-sputtering power presented similar behavior and response time. The response time for Pure Ga₂O₃ was 67 seconds and a sensitivity value of 1.2, whereas for the films deposited with the maximum level of w-doping showed a time response of 71 seconds and sensitivity value of 1.2. Nevertheless, it is important to mention that similar to the results encountered when using line set up sensors, the best sensor performance was achieved when the films were deposited with a sputtering power in the range of 40W-60W, were the time response reduced to 43 s and 46 s, respectively, and the sensitivity of the films reduce to a 1.1 value. Furthermore, the highest sensitivity value was achieved when the film was deposited using P_w=20W, which increased from 1.2 with un-doped Ga₂O₃ to 1.5. Nevertheless, the time response increased from 67s with un-doped Ga₂O₃ to 73 s when the P_w=20W was used.

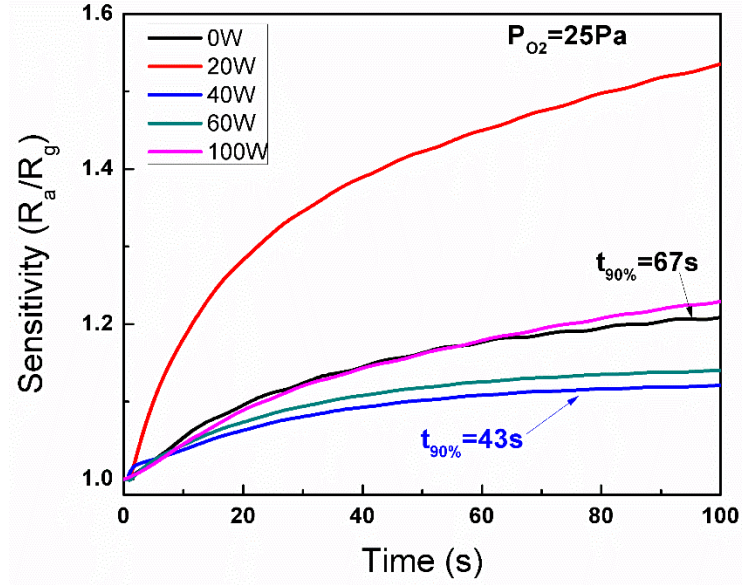
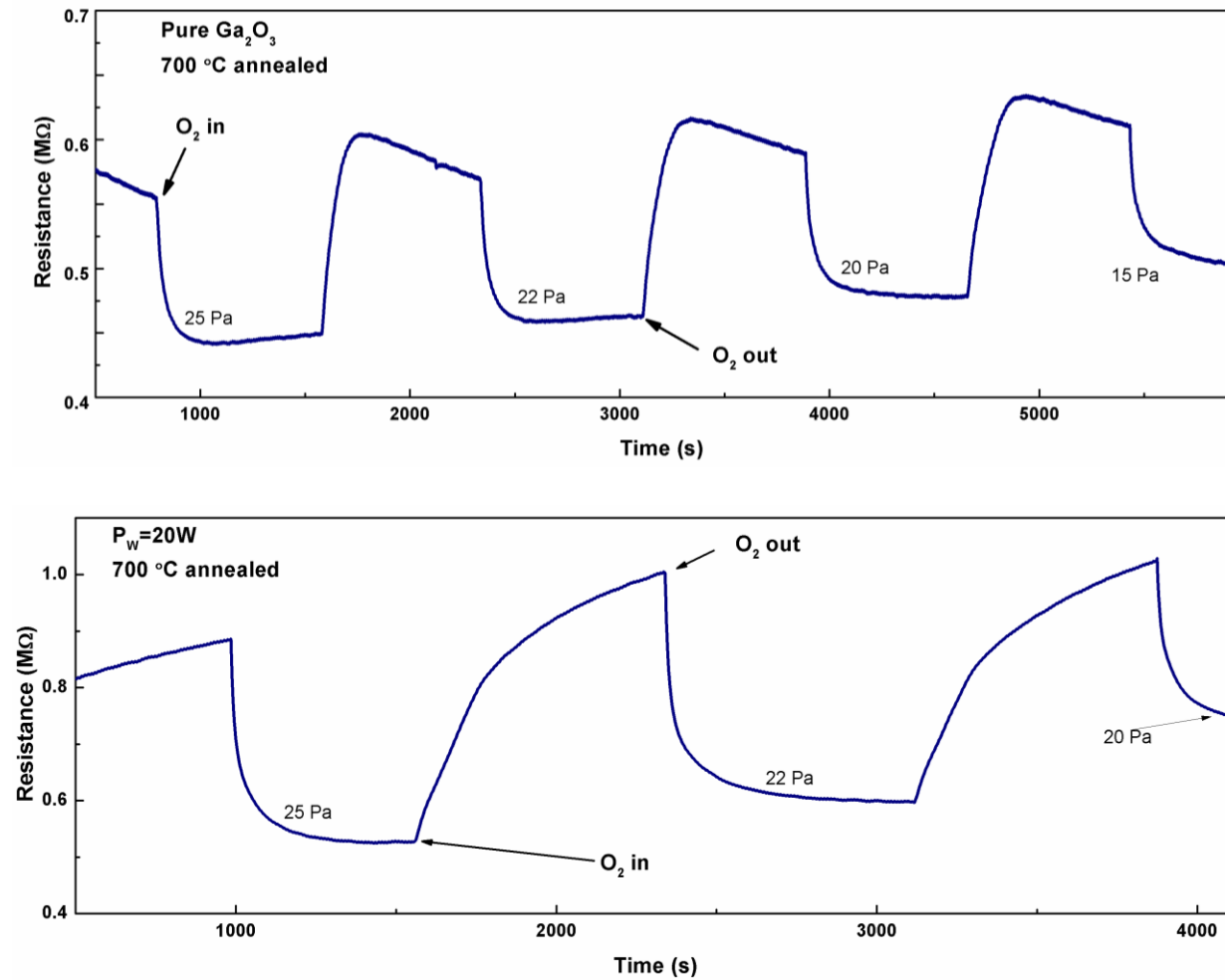


Figure 5.30: Sensitivity and time response comparison of Ga₂O₃ based sensors evaluated at 800 °C.

24 hours after the films were evaluated in terms of initial sensitivity and time response, they were tested under different partial pressure of oxygen in cyclic periods of pure Ar flow and Ar/O₂ flow to determine the repeatability and stability of the films at 800 °C. The films that demonstrated the highest stability is the un-doped Ga₂O₃ film as presented in figure 5.31 where the comparison of the oxygen sensor response for Ga₂O₃ bases films is presented. Similarly to the results previously presented, the W-doped films with higher repeatability are the ones deposited within the range of 40W to 60W of tungsten sputtering power, due to the stability of the resistance values when the films are under oxygen exposure. However, the stability is affected by the presence of W, as is evident from the increase of noise p on the P_w=40W responses, the sharp curves presented on P_w=20W and 100W, and the sudden change in resistance during Ar exposure. Un-doped Ga₂O₃ also presented change in the resistance value under Ar exposure, corresponding the polarization effects caused by the ionic conductivity of the films (M Fleischer et al. 1995), and the constant increment on the base resistance is attributed to the grain boundary capacitance of the films (Reti 2001). The response for all the evaluated films corresponds to the p-type conductivity

where the resistance of the films decrease with the presence of oxygen, this behavior is attributed to the diffusion of Be-ions from the Pyrex glass substrates. This behavior was previously described by Kiss et al (Kiss et al. 1999).



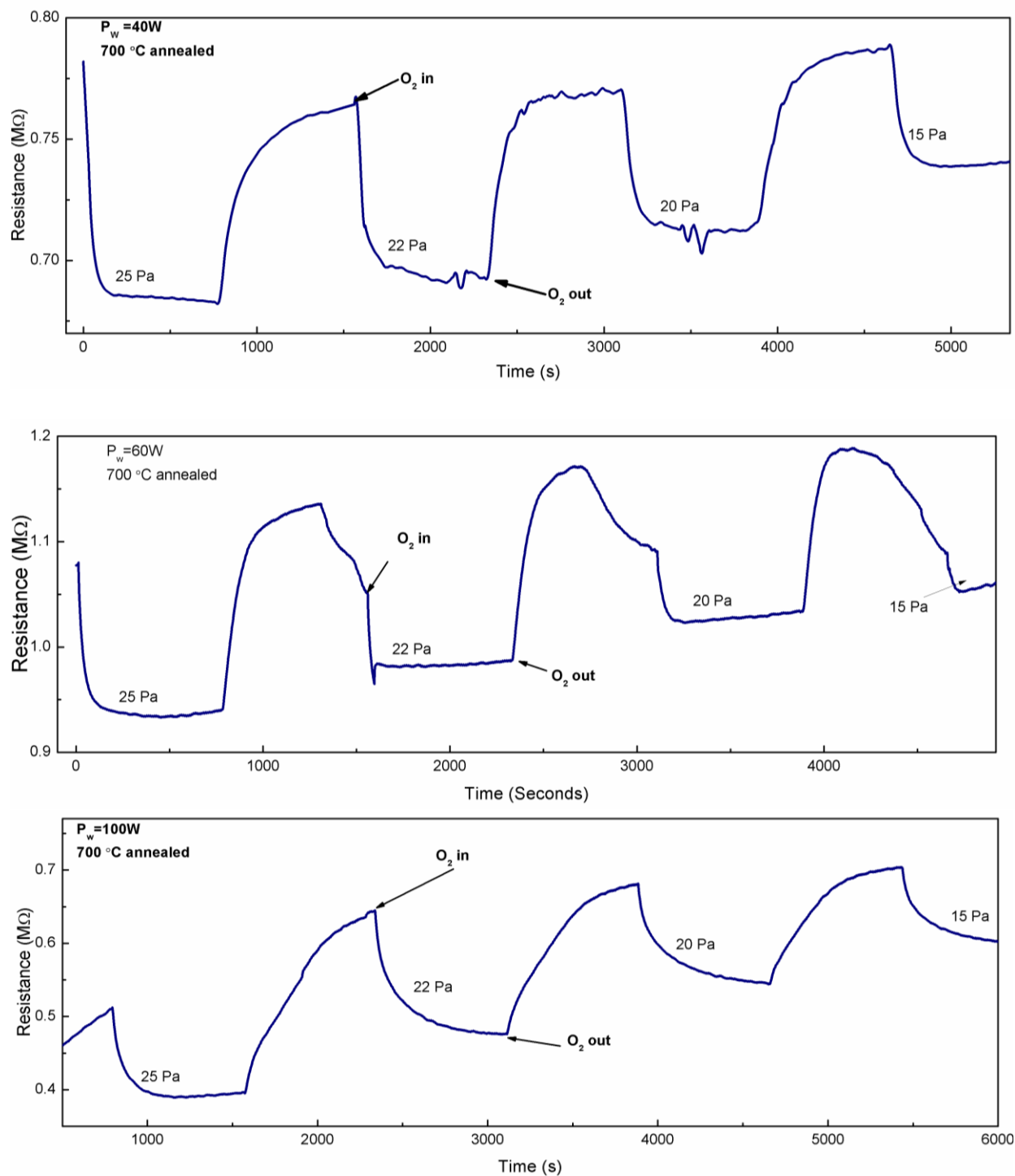


Figure 5.31: Oxygen sensor response for Ga₂O₃ based sensor evaluated at cyclic inputs of P_{O2} at 800 °C

The oxygen partial pressure employed for this tests varied from 15, 20, 22, and 25 Pa, and their resistances values were employed to calculate the m-values corresponding to Eq 1.17 which represents the sensing mechanism of MOS sensors. However, the m-values for the films deposited with 20W and 100W of W-sputtering power did not showed sufficient stability and repeatability for the calculation; whereas for un-doped Ga₂O₃ films the m-value calculate was 0.26 which is close to the -1/4 which correspond to the theoretical value presented in the literature (Xu, Zhou, and Sorensen 2000). The values for 40W and 60 W reduced to 0.19 and 0.22, respectively. Figure 5.32 shows the plots for the Log σ vs Log P_{O₂} and the m values are obtained by the linear regression analysis of the data obtained, all the data points were recorded when the films were deposited on the pyrex glass substrates and evaluated at 800 °C.

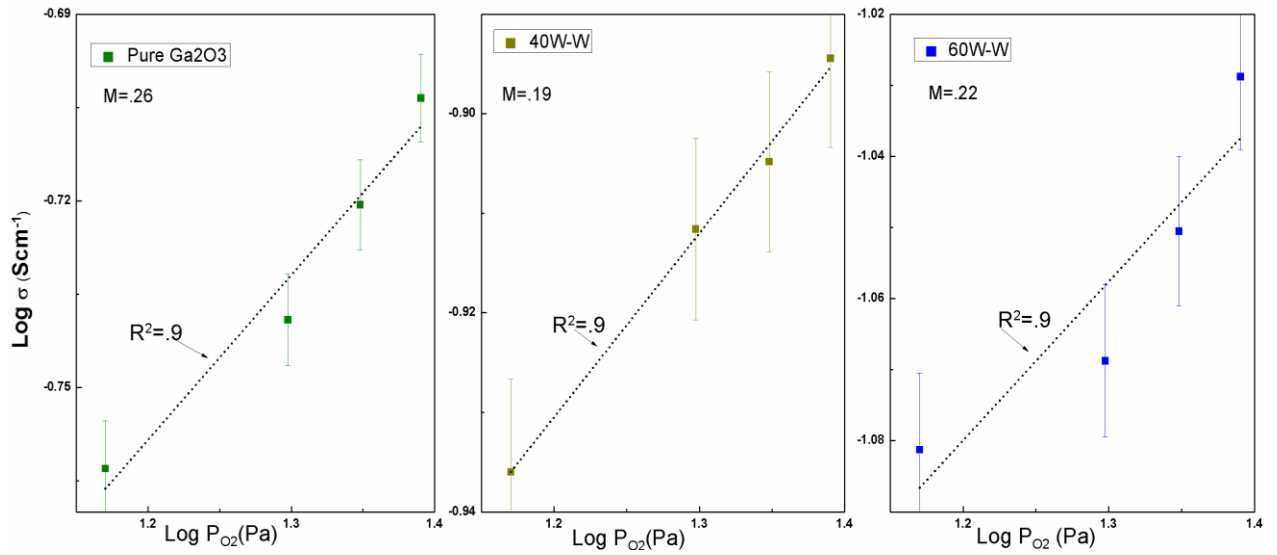


Figure 5.32: Log σ vs Log P_{O₂} plots for m-value calculations for Ga₂O₃ based films evaluated at a constant temperature of 800 °C

Chapter 6: Discussion

The discussion of the observed results and mechanism of the Ga-oxide based materials and their sensing behavior is presented in this chapter. The logistic discussion is presented in four sequential parts: (1) intrinsic Ga_2O_3 , (2) effect of W-incorporation into Ga_2O_3 , (3) thermal stability and (4) sensor performance and, finally, comparison of intrinsic versus W-incorporated Ga-oxide materials.

The observed growth behavior, crystal structure, grain-size variation, and surface morphology evolution in nanocrystalline Ga_2O_3 as a function of processing conditions can be explained as follows. The growth temperature, which is an important thermodynamic parameter, plays an important role, besides the reactive oxygen partial pressure, in deciding the microstructure as well as properties of materials resulting from vapor-transport deposition. The observed results for intrinsic Ga_2O_3 can be thus accounted for the effect of deposition temperature since the other conditions are kept constant. We first establish the optimum temperature required to obtain nanocrystalline, intrinsic Ga_2O_3 films based on the experimental results. If the deposition temperature is low so that the period of the atomic jump process of ad-atoms on the substrate surface is very large, then the condensed species may stay stuck to the regions where they are landing thus leading to an amorphous or amorphous medium. However, sometimes such amorphous matrix may contain embedded small but ordered nano-particles. In the present work, based on the experimental results, it is very clear that for Ga_2O_3 films deposited at room temperature, the impinging flux may be just sticking to the substrate surface at its place of hitting with almost no surface diffusion since no well-defined long-range order or oriented growth is observed (XRD or SEM data). However, with increase in deposition temperature, the ad-atom mobility on the surface increases. The small size grains, spherical in shape, observed in SEM

images coupled with XRD data for films grown at 500 °C indicate the situation is entirely different compared to films deposited in the temperature range of 25-500 °C. The presence of well-resolved peaks indicates the improved structural order resulting in the formation of nanocrystalline Ga₂O₃ films. This is due to increased diffusion of ad-atoms leading to a larger rate of atoms joining together and, hence, formation of nanocrystalline films as a result of an increase in deposition temperature. The observed higher temperature to deposit nanocrystalline Ga₂O₃ films by the sputter deposition for the set of conditions employed in this work can be attributed to the difference in material's physical and electronic characteristics when compared to other oxides. The morphological changes, increase in grain-size as well as their distribution characteristics, as a result of further increase in deposition temperature can be attributed to the enhanced mobility of sputtered-species impinging on the Si(100) surface. Similar to diffusion coefficient, the grain-size (L) is typically observed to depend on temperature as:

$$L = L_0 \exp (-\Delta E/k_B T) \dots\dots\dots 6.1$$

where ΔE is the activation energy, k_B is the Boltzmann constant, T is the absolute temperature ($T=T_s+273$ K), and L_0 is a pre-exponential factor that depends on the physical properties of the substrate-deposit. At lower temperatures, the impinging species may not have sufficient energy for atomic jump process or to overcome the potential energy of the nucleation sites of the substrate. At higher temperature, the mobility of ad-atoms on the substrate surface is generally higher. As a result, the diffusion distance of the ad-atom on the surface increases and the collision process initiates the nucleation for more ad-atoms joined together resulting in increased L values. If we assume that the grain-size is directly related to the surface diffusion of sputter-deposited species on the substrate surface, one would expect to see the increase in L with temperature in accordance with the above relation. Therefore, the grain size values determined from XRD and SEM

measurements were analyzed, where a very good agreement between the measured L values from XRD and SEM data and data fitting to an exponential function were noted. These features indicate the thermally activated process of surface diffusion of the impinging flux which account for the evolution of crystallization, surface morphology and grain-size as a function of deposition temperature as seen in XRD, SEM and AFM data.

Our attention now is towards the specific phase of nanocrystalline Ga_2O_3 films. Note that Ga_2O_3 can exhibit polymorphism and can adopt different crystal structures. However, the goal of this project is to obtain $\beta\text{-Ga}_2\text{O}_3$. XRD data indeed indicate that the Ga_2O_3 films crystallize in Ga_2O_3 monoclinic structure, which is expected based on the phase-stability considerations. Stabilization of any of the phases is not observed in nanocrystalline Ga_2O_3 films. Thus, the outcome of the initial processing efforts of intrinsic Ga_2O_3 films and associated characterization is the microstructure phase diagram, which is summarized in Fig. 6.1. This phase diagram explains the effect of substrate temperature on the crystal structure, chemical composition, surface morphology and structural transformations noted along with specific grain size of Ga_2O_3 films. This schematic representation of the summary of the data will be quite useful for other researchers in the field when sputter-deposition is considered to fabricate Ga_2O_3 films for a set of given technological applications. For our purpose of W-incorporation and oxygen sensor, the most important features that was considered further is the fact that a deposition temperature of 500°C is critical to promote or resulting in the formation of nanocrystalline Ga_2O_3 films.

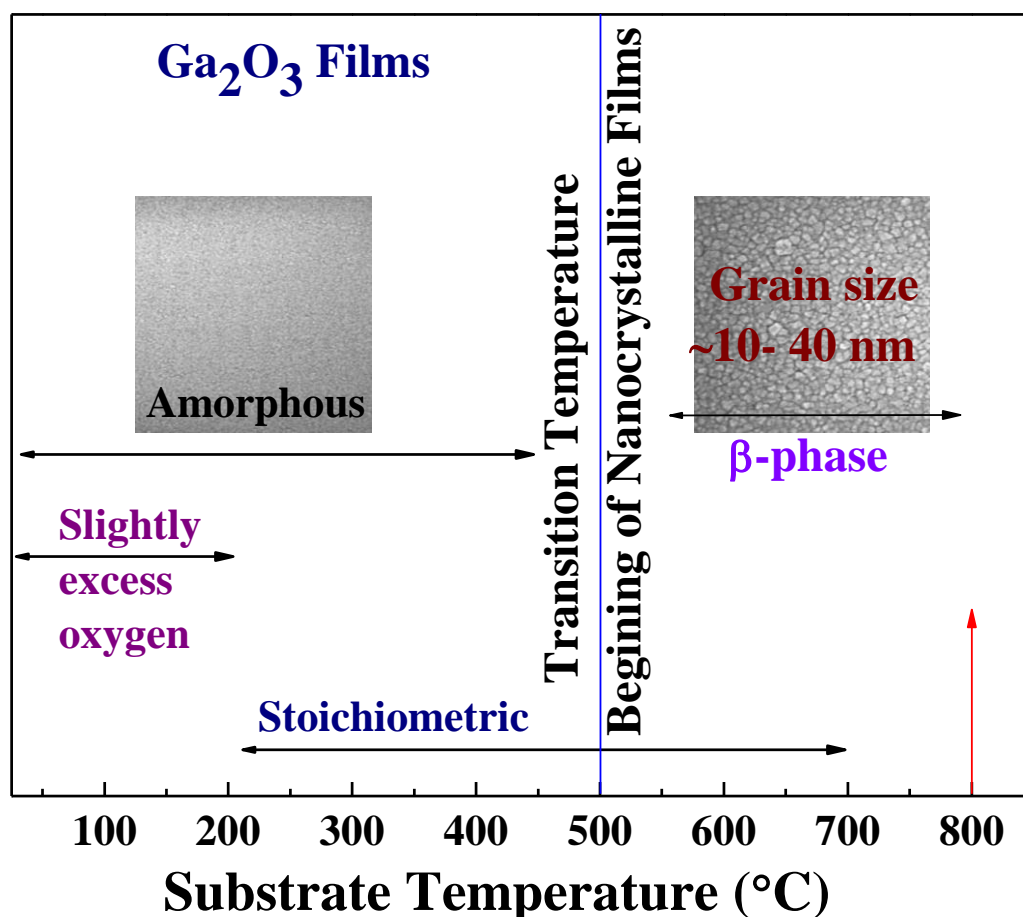


Figure 6.1: Behavioral diagram of intrinsic Ga₂O₃ deposited as a function of substrate temperature (Kumar et al. 2013)

Now, we focus our attention on the XPS results to establish the surface chemistry of the Ga₂O₃ films deposited at variable substrate temperature. XPS analyses indicate that the films are nearly stoichiometric and Ga exists in its highest chemical valence state. The BE values of Ga 2p_{3/2} and Ga 2p_{1/2} peaks (1118.0 and 1145.0 eV, respectively) and the BE shift from Ga⁰ (1 eV) characterizes the Ga in its highest chemical valence state (Ga³⁺) in all the films, almost without any appreciable change, as a function of deposition temperature. This is important from the view point of electronic structure since reduced chemical valence states of Ga can create defects, which in turn alter the optical and electrical properties. Furthermore, the chemical stoichiometry analyses

made by XPS and RBS are in good agreement with each other. Also, these chemical studies rule out the possible compositional defects or reduced Ga states and their influence on the optical and electrical properties of Ga₂O₃ films.

After having discussed about the effect of deposition temperature on the growth, crystal structure, surface chemistry, and phase formation of intrinsic Ga-oxide films, attention now is towards is to establish the direct relationship between the structural and electronic properties. Such structure-property relationships are quite useful and provide a roadmap to optimize the conditions to obtain Ga-oxide films with desired properties, which can be suitable to meet the set criteria of a given application.

We considered the index of refraction (n') and structural quality of sputter-deposited Ga₂O₃ films grown under variable growth temperature (T_s). It must be emphasized that the optical properties are sensitive to the film microstructure. Various factors such as surface/interface structure, grain size, crystal quality, lattice parameters, defect structure, and chemical composition influence the optical properties of oxide films. The growth temperature, which is an important thermodynamic parameter, plays an important role, besides the reactive oxygen pressure, in deciding the microstructure as well as properties of materials resulting from sputter-deposition. Therefore, the XPS, AFM, and SE results along with electrical resistivity variation are considered in order to derive the functional relationship between the surface physics, morphology, and optical properties of Ga₂O₃ films.

Finally, the observed variation in the index of refraction and electrical resistivity of Ga-oxide films can be explained based on the microstructure variation of Ga₂O₃ films with substrate temperature. A simple model can be formulated to explain the observed functional relationship between the optical constants and substrate temperature in Ga₂O₃ films. Evident from the SE

results, the dispersion of optical constants depend on the growth temperature. XRD measurements demonstrated that the Ga_2O_3 films are completely amorphous when deposited at 25-500 °C, at which point amorphous to nano-crystalline structural transformation occurs. The observed increase in ' n ' values when Ga_2O_3 films are grown at higher temperatures can, therefore, be attributed to the improved structural order and packing density of the films. Furthermore, while surface roughening can induce scattering losses, AFM data evidenced the rms roughness of the films is not significant in Ga_2O_3 films as a function of substrate temperature. Usually, rough film surfaces result in increased light-scattering losses at the interface. Therefore, the critical temperature (500 °C) noted in the XRD measurements seems to promote the structural order and increases the mobility of ad-atoms to join together to increase the packing density of the material in the films leading to observed increase in ' n ' values. Such behavior was also noted in sputter-deposited Y_2O_3 films. The effect of microstructure was also reflected in the electrical resistivity analysis of the Ga_2O_3 films. The electrical resistivity usually becomes higher with grain size reduction due to the increasing grain boundary volume and associated impedance to the flow of charge carriers. If the crystallite size is smaller than the electron mean free path, grain boundary scattering dominates and hence the higher electrical resistivity. Furthermore, the electrical resistivity is also very sensitive to lattice imperfections in solids, such as vacancies and dislocations which are often present in nanocrystalline materials. In addition to that, lattice strain and their distortions can affect the charge mobility causing a decrease in conductivity. The room-temperature electrical resistivity variation with substrate temperature observed for Ga_2O_3 films can be explained by taking these factors into consideration. Ga_2O_3 films deposited at a temperature of room temperature-300 °C are completely amorphous as evidenced in the XRD studies. The randomness or disordered structure of the films, therefore, accounts for the observed high electrical

resistivity of amorphous Ga_2O_3 films. The resistivity decrease with increasing substrate temperature can be attributed to the increasing crystalline nature of Ga_2O_3 films. The observed sharp decrease in the electrical resistivity for Ga_2O_3 films grown at higher temperatures seems to be a result of the combined effects of the grain-size increase and the phase transformation from amorphous- Ga_2O_3 to β - Ga_2O_3 films. Thus, this trend in resistivity is expected and can be attributed to better crystallinity, the presence of larger grains and fewer grain boundaries in the samples prepared at higher temperatures. Furthermore, the electrical results are in agreement with the results obtained from AFM and XRD studies.

The most important characteristic feature that was observed in this study is the reduction in the bandgap of Ga_2O_3 due to W-incorporation. As noted in optical absorption measurements and analyses, W-induced effect is predominant on the electronic parameters, such as band gap and index of refraction. The W-incorporation induced changes not only provide a clue about the material modifications but also accounts for the observed improvement in sensor response time. Therefore, an attempt is made to understand the W-incorporation induced changes. The effect of W-incorporation and the mechanism of electronic structure changes leading to a substantial red shift in the bandgap can be understood as follows. To shed light on the crystal structure of W-incorporated Ga_2O_3 films, the available crystallographic data can be considered. The very first is the structural similarity. While both Ga- and W-oxides exhibit polymorphism, monoclinic structure is thermodynamically stable phase for both W-oxide and Ga-oxide. WGO films crystallize in monoclinic structure as evident in XRD patterns of both Ga_2O_3 and W-incorporated Ga_2O_3 films. No significant changes were noted due to W-incorporation. If the ionic size and other structural parameters are compatible or comparable, a solid solution without any structure change can be expected for W-incorporation into Ga_2O_3 lattice, i.e., W atoms can occupy the lattice

positions of Ga inside the β -Ga₂O₃. This indeed is clearly seen in XRD patterns, where there is no evidence of secondary phase or no distortion of the peaks of parent β -Ga₂O₃. Therefore, XRD observations indicate that W-incorporated β -Ga₂O₃ films accommodate W-atoms without any structural distortion even for the highest concentration of W-atoms at a sputtering power of 100 W. The reason for W-Ga₂O₃ single phase system could be the comparable ionic radii of Ga³⁺ and W⁶⁺ ions which are 0.062 nm and 0.060 nm, respectively. Therefore, W ions can occupy the Ga-lattice positions and can act as substitutional metal dopants. The effect of W-incorporation into β -Ga₂O₃ on the optical properties can then be understood as follows. The bandgap value measured for in this work for Ga₂O₃ films without any W-incorporation (5.0 eV) is in agreement with that reported β -Ga₂O₃ in the literature (Müller et al. 2014; Ramana et al. 2014a). W-incorporation effectively induces the reduction in the bandgap as seen in previous Chapter, where the results are presented. Due to substitutional nature, W ions incorporated will form donor levels within the bandgap of β -Ga₂O₃. The increasing sputtering power to W-metal target from 50 to 100 W increases the effective concentration of W content incorporated into the β -Ga₂O₃ structure. This will in turn increase the donor levels within the bandgap which is responsible for the effective reduction in the bandgap. This accounts for the observed red-shift in the bandgap of β -Ga₂O₃. The substantial shift can be attributed to the large amount of W-ions able to form single phase system. The evidence for this comes from chemical analyses of the films where it was found that the W concentration increases from 5 at. % to 11 at. % with increasing sputtering power to the W-metal target from 50 to 100 W. Note that the bandgap of W-oxide is 3 eV. The measured E_g for WGO films is not even close to this value which is another, indirect evidence for the absence of secondary W-oxide phases as noted in various other measurements. While the attempt made in this study is to understand the effect of W-incorporation on the electronic structure of Ga₂O₃, we believe that

there may be further options available to further tune the structure and optical properties of W-Ga₂O₃ materials, which could be useful for improved electronic and optical device applications.

We now focus our attention to evaluating the structural and morphological behavior of intrinsic versus W-doped Ga₂O₃ films. It should be noted that the XRD peaks were not intense for W-incorporated Ga₂O₃ compared to that of Ga₂O₃ films. We can consider the early models of thin film growth and microstructure to explain the differences although such models were mostly based on observations noted for metal and alloy thin films. Thornton developed a model, which is a schematic representation, to explain the growth behavior of sputter-deposited films when is deposited under different argon sputtering pressures and substrate temperatures. The model is presented in Figure 6.2 (Thornton 1974). The diagram shows the importance of the thermal energy to achieve recrystallization of the film once deposited onto the substrate by increasing the ratio of the substrate temperature over the melting temperature of the sputtering material (T/T_M). High T/T_M ratio provides sufficient energy to the arriving adatoms to increase their mobility and form granular structures. This is evident in the case of temperature dependent deposition of Ga₂O₃ based films that initiate full crystallization at 500 °C in the case of intrinsic films, and 800 °C when W is incorporated. It is important to mention that parameters such mean free path of ejected atoms, reactive gases such O₂ and N₂, and voltage bias during deposition also influence the structure, morphology and topography of the films, which may be the reason for the observed change in crystallization temperature when W is doped in Ga₂O₃. Nevertheless, it is important to mention that sputtering is a non-equilibrium process, which has the capacity to fabricate exotic materials due to quenching process that occurs at the surface of the film. Compared to thermal evaporation and chemical vapor deposition, which are processes that form films under thermodynamic equilibrium, sputtering is a high energetic process that does not require external thermal energy

for the quenching of the films. This condition is better exemplified by the deposition of diamond at room temperature (Wasa, Kitabatake, and Adachi 2004).

It is also important to mention the non-stoichiometric growth of intrinsic Ga_2O_3 films at variable substrate temperature. Our finding demonstrated that by depositing the films at temperature higher than 200 °C the Ga to O was maintain at 1.5, but if temperatures lower than 200 °C is utilized the films presented a metal deficiency in their chemical composition. This phenomena was previously observed in Y-based sesquioxide (Y_2O_3) (Muduvakkat et al, 2012). Their results showed that, again, if the films was deposited in the temperature range from room temperature to 200 °C the films will show an excess of oxygen in the chemical composition of the films. This oxygen excess was attributed to the lack of thermal energy to fully oxidize Y metallic formation in the film, even when the argon to oxygen reactive gas ration was kept constant (Mudavakkat et al. 2012)

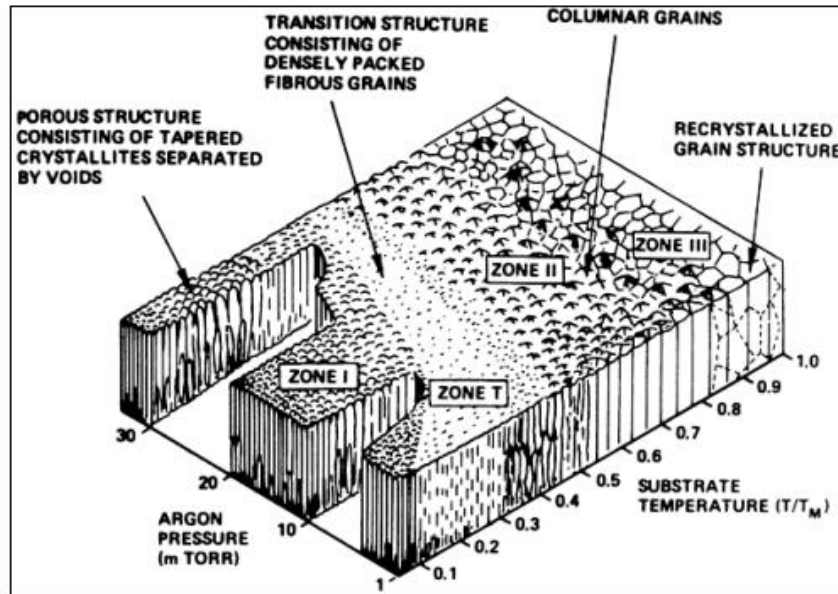
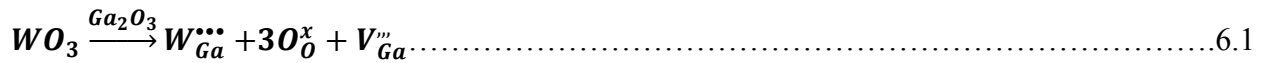


Figure 6.2: Sputtering growth diagram presented by Thornton (Alfonso, Olaya, and Cubillos 2012)

After having understood the structure and morphology evolution in intrinsic and W-incorporated Ga₂O₃ films, the attention now is towards thermal stability. Based on the results, we propose a three stage, independent processes, which account for the thermal stability and annealing induced changes in the Ga-W-O nanocrystalline films. These are: (a) pore formation leading to porosity in the Ga-W-O films, (b) W-diffusion across the interface and (c) the reduction of W atomic content. These phenomenon can be explained as follows. The W-diffusion occurs as per the defect equilibria in the system under the effect of W-incorporation. As gathered from XPS results, W⁺⁶ and Ga⁺³ were the dominant ionic states of W and Ga, respectively, in these Ga-W-O films. Note that the ionic size of W⁺⁶ and Ga⁺³ are 0.060 nm and 0.062 nm, respectively. Additionally, while Ga₂O₃ and WO₃ both exhibit polymorphism, monoclinic phase is thermodynamically preferred phase for both the oxides. This allows, under W-doping up to certain concentration, W ions to act as substitutional defects in the host matrix of Ga₂O₃. The defect chemistry of the films can be presented in the following equation using Kröger-Vink notation (Kroger, 1973):



The equation shows that the charge equilibria for W-doped films, where W is assumed to be acting as a substitutional defect, is achieved by introducing Ga³⁺ vacancies on the Ga₂O₃ matrix. This process open pathways for W ions to flow from the surface towards the bulk portion of the films, as evident from the results of XPS and RBS measurements.

It is also important to consider the difference of electronegativity values of Ga and W because due to this difference the formation of secondary phases of WO₃ in the film is enabled. Similarly, the formation of WO₃ as the dominant oxide formation for W, was expected due to the partial pressure of oxygen employed during deposition (~1E-6 atm) as well as the substrate

temperature of 500 °C according to the W-O phases diagram presented in figure 6.3. Previous work performed in reactive rf-sputtered WO₃ films demonstrated the dependency of oxidation state of tungsten and stoichiometry of the film in the ratio of the partial pressures of oxygen and argon. Their results suggested that to form WO₃ films the ration of P_{O2}/P_{Ar} has to be 0.25 or higher (Lemire et al. 2002). In this particular work, the ratio employed for deposition was 0.33 and the W⁶⁺ was the dominant oxidation state for tungsten.

From XPS surface analysis the shouldering of the W4f peaks was encountered, this behavior is representative of the presence of different oxidation states. Khyzhun et al. have reported a study of different oxidation states of W, where the results demonstrated the shift of the W 4f peak to the right when the oxidation state changes from W⁴⁺ to W⁶⁺ similar to the results that were recorded in this research. After the disintegration of the W4f XPS peak using CASA software and the study of the FWHM of the peak causing the shouldering effect, the position of the peak producing this effect is at 39.2 eV, which from historically available data corresponds to the formation of WO_x when x=2.77 (Khyzhun 2000). After exposing the film to the post-deposition heat treatment, the partial pressure of oxygen was relative to the oxygen in the environment which also allow the film to form secondary WO₃ phases.

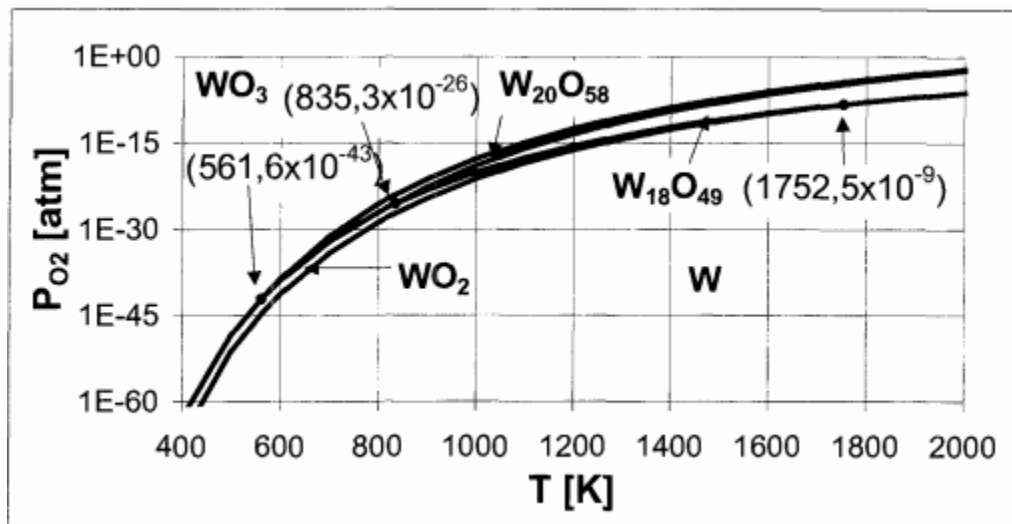


Figure 6.3 W-O phase diagram proposed by Schwenke (Schwenke 2001)

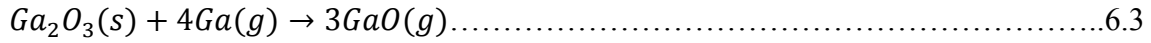
The mechanism for porosity formation and the reduction of W-atomic percentage inside the film is explained through the formation of metal-hydroxyl formations at the surface of the film as previously reported. Tungsten oxides become highly volatile under the presence of water vapor; the evaporation of W-O-H molecules decreases the overall W-content on the films, while inducing pore formations. GIXRD results demonstrated presence of WO₃ formation on the surface after the films are exposed to high temperature annealing, whereas XPS results demonstrated broadening of O1s peaks corresponding to the presence of hydroxyl formations at the surface.

The W-O-H formations corresponds to tungstic acid which from previous studies, can be generated when WO₃ interacts with partial pressure of vapor at elevated temperatures (>800 °C), and the chemical reaction is expressed as follows (Lassner and Schubert 1999):



Sublimation of WO₃ in the presence of water vapor was studied by Millner at temperatures of 1000 °C, and 1 atm of pressure (Millner and Neugebauer 1949). In this particular work, the presence of water vapor is provided by the relative humidity in the atmosphere.

The possibility of the evaporation of Gallium sub-oxide during operation at temperatures above 400 °C may exist in the case of high amount of gallium vapor pressure as the following chemical reaction expresses (Tsai et al. 2010):



Nevertheless, studies on the presence of volatile metals on the flue gases from coal combustion do not reveal presence of gallium as a byproduct (Pavageau et al. 2002). At the same time, the Ga-hydroxyl formations such Ga(OH)₃ and GaOOH are oxidized at temperature >700 °C, and transformed into β- Ga₂O₃ (Sato and Nakamura 1982).

To corroborate the presence of the two mechanisms discussed in this work (W-diffusion and W-content loss), a representative sample was evaluated using XPS depth profile before and after the exposure to a high temperature treatment, and the results are plotted in Figure 6.4. It is evident that change in the overall atomic concentration of W decreased after the annealing process was performed, which can be explained by the volatilization of W-hydroxyl phases. Furthermore, it can be noticed that the oxygen content in the film decreases as well, and the increment in thickness of the Si-W-Ga-O interface after the high temperature exposure. The change of oxygen content is related to the W-content loss, which can be explained through the change of the oxygen to metal ratio decreasing from 3 for WO₃ to 1.5 for Ga₂O₃ which is the predominant oxide after the films are annealed. In the case of the interface broadening, it is attributed to the diffusion of Si from the substrate towards the interfacial region of the film.

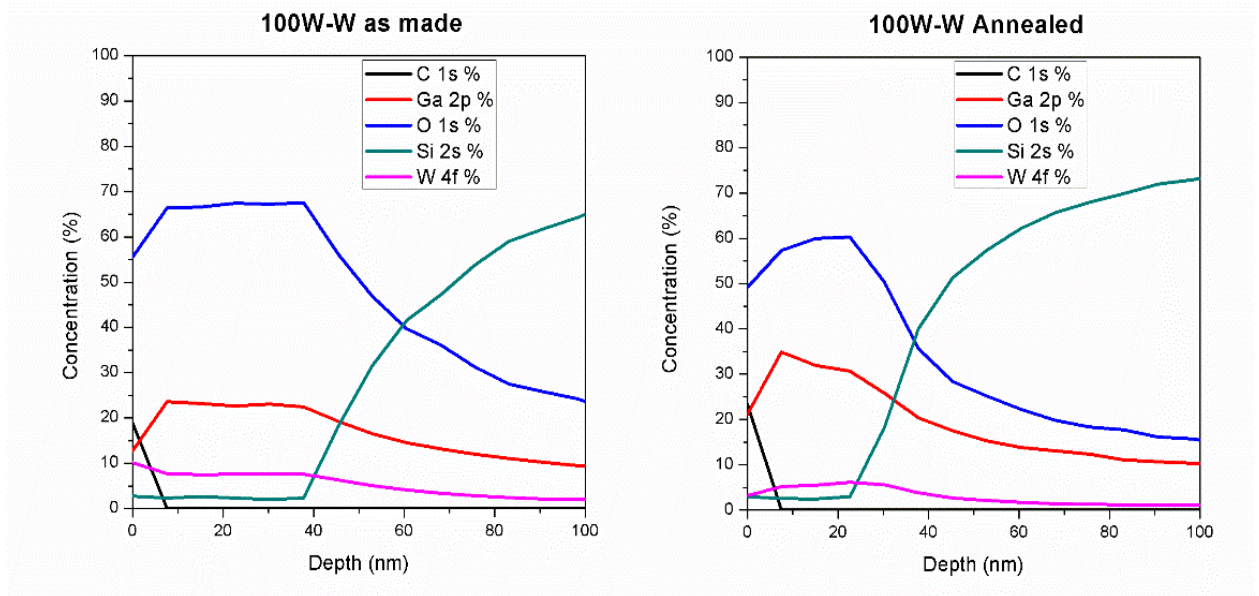


Figure 6.4: XPS depth-profile of as-grown film vs annealed W-doped Ga₂O₃ representative film.

Among these three phenomenon, porosity formation is the mechanism which aids the oxygen sensor performance of the films. The pore formation follows the dimension corresponding to mesoporous materials (2 nm -100 nm pore size) which are ruled by Knudsen diffusion. Mesoporous films gas diffusion is directly related to the dimensionality of their pores because this magnitude is roughly comparable to the molecules mean free path (Thorsten Wagner et al. 2013). These pores, as previously explained, are formed due to the evaporation of W-O-H molecules. As the porosity dimension increases the diffusion coefficient increases as well, as the following equation shows:

$$D_k = \frac{4r}{3} \sqrt{\frac{2RT}{\pi M}} \dots\dots\dots 6.4$$

Where D_k is the Knudsen diffusion coefficient, r is the pore radius, T is temperature, R is the gas constant and M is the molecular weight of the diffusing gas (Sakai et al. 2001). The increment of the diffusion coefficient has a direct impact on the rate at which oxygen and bulk defects of the material interact and, as explained before, at temperatures $> 700^\circ\text{C}$ bulk defect equilibria is the

major contributor to the conductivity variation in the presence of oxygen. Furthermore, the time response of Ga₂O₃ films significantly improves by the formation of the mentioned pores as the following differential equation expresses:

$$\frac{\partial C_A}{\partial t} = D_k \frac{\partial^2 C_A}{\partial x^2} - k C_A \dots \dots \dots 6.5$$

Where C_A is the concentration of Oxygen, t is time, k is the rate constant, and x is the distance that the oxygen molecules diffuse towards the bulk of the film (Sakai et al. 2001; Yamazoe 2005). The instability of the sensor response for the films when the atomic percentage surpassed 5% is due to the high quantified presence of WO₃ secondary phase formation which electrical response under high temperature oxygen sensing condition is presented. The oxygen activation energy of WO₃ reported in the literature is .79 eV (Aguir, Lemire, and Lollman 2002), and 1.8 eV for Ga₂O₃ (Bartic, Ogita, et al. 2007), as mention before the sensitivity to oxygen for MOS sensors works as a bell curve finding their maximum value at certain temperature that is directly relate to activation energy of the material. The differences in the responses to oxygen at elevated temperature is one of the key reasons for the instability of the electrical properties during oxygen sensor evaluation. Similarly, the parameter “m” representative to the defect equilibria and sensitivity in equation 1.17 varies from WO₃ to Ga₂O₃, which is also an influencing factor for the lack of reliability in the responses of the sensors. WO₃ presents a “m” value of 1/6 (Gillet et al. 2003), whereas for Ga₂O₃ 1/4 is the representative “m”value (Xu, Zhou, and Sorensen 2000).

Chapter 7: Conclusions

The different studies performed in this research allowed us to understand the overall behavior of W-doping into Ga_2O_3 sputter deposited films. The evaluation of the optical-structural-chemical properties of the films revealed that the W-content and chemistry will have profound influence on the electronic behavior and sensor response of the W-doped Ga_2O_3 films. Increasing sputtering power to the W target increases W-doping content in the films; therefore, tailoring the composition is possible by the careful choice of processing conditions. In terms of the optical properties of the films, the transmittance spectra showed that the W-incorporation reduces transparency of the films, and at the same time the band gap values of the films decreases with increasing W-content. On the other hand, the index of refraction of the films increased with increasing W-atomic content. The surface morphology and the crystal structure of the films changes from monoclinic to amorphous whenever W is doped into the film. The chemical state analysis of the films suggested the only Ga^{3+} was present in the films, whereas for W-doped samples, W^{6+} was the dominant oxidation state, but presence of sub-6+ oxide was encountered

The thermal stability of the Ga-W-O films indicated the three main phenomenon occurred during annealing at 900 °C. These are porosity formation, W-diffusion and W-atomic percentage decrement. The surface morphology of the films, evaluated using SEM, indicate a transition towards mesoporous films. The valance states of the films, analyzed using XPS, showed that no presence of sub-6+ oxidation state for W ions, and only chemical states present were Ga^{3+} and W^{6+} . Similarly, the thermal stability of the films studied by analyzing the surface morphology and chemistry of three films after exposing them to 15 hours at 900 °C indicate no significant changes. The evaluation of the oxygen sensor capabilities demonstrated that the time response of the films in sensor can be improved by tuning the W-content in the films. In fact, annealing the films to 1

hour at 900 °C can induce pore formation, which results in enhanced oxygen sensor performance with improved response time. However, the sensitivity of the films is affected by the presence of W ions. The ideal W-sputtering power for enhancing the time response while sustaining stability is within the range of 40W-60W. For the cases where W-doping occurred outside that range the stability of the films diminishes, and repeatability is compromised. The already mentioned improvement in the time response of the Ga₂O₃ based sensors is attributed to the increasing Knudsen diffusion coefficient; for this particular set of samples, the diffusion mechanism is dominated by Knudsen diffusions due to the dimension of the pores. The sensors were evaluated using two types of set-ups, in-line and integrated interdigital electrodes, in the in-line setting two probes are attached at the surface of the films and the change in resistance is measured by means of ohms law, and in the case of integrated interdigital electrodes, a predefined distance of 100 micrometers is used as separation between electrodes and the films is deposited on top of these electrodes. Both settings showed similar results, suggesting that the optimum range of W-doping is when the films are deposited between 40W and 60W of sputtering power under the deposition conditions that this work followed. The activation energy of the films was also studied and the behavioral trend acted similar as the band gap values of the films, where the energy reduced with increasing W-incorporation.

Finally, the mechanical properties of the films were evaluated as a function of W-content and the results demonstrated an overall increment on the hardness values and Young modulus with increasing W-content. Nevertheless, when the films are deposited using P_w=50W the mechanical properties of the films decrease compared to the value on un-doped Ga₂O₃. This group initiated the investigation of the mechanical properties of the MOS sensors, which up to now was not

extensively discussed in the literature and is one of the key points to maintain systematic stability of the oxygen sensors.

This research fulfilled the goals that were set at the beginning of the investigation, especially in the case of the improvement of the response time required for the Ga_2O_3 based sensors to overcome the change in conductivity in the presence of high temperature oxygen, in particular at temperatures required to work on combustion processes ($>700\text{ }^\circ\text{C}$). Furthermore, not only the improvement of the response time was achieved, but also the understanding of the mechanism that enhances the oxygen sensors characteristics of the studied materials.

Chapter 8: Future Work and Outcomes

The following work is recommended for continuation of this research:

- Investigation of the electrical properties via Hall Effect method to determine the change in carrier mobility, carrier concentration, and the type of conductivity that W-doped films. This experiment will not only benefit the on-going investigation of high temperature oxygen sensors, but also will provide information relatively important for application such as transparent conductive oxides, and high power electronics.
- Manufacturing W-doped Ga_2O_3 sensor for in-situ testing. The manufacture process will include the deposition of an integrated heater in the back of the substrate to be able of sustain steady temperature during operation. The inclusion of a protecting casing must be consider to protect the films from incoming ashes and solid byproducts of the combustion. The connections between the interdigital electrodes and the wires carrying the incoming current should be connected with platinum weld to minimize resistance.
- Continuation of different refractive metal doping. This work investigate the effect of W-doping in the oxygen sensor characteristics of Ga_2O_3 . Nevertheless, the doping of material with different oxidation state may help improving the sensing process of the film, while keeping the stability that Ga_2O_3 offers. Refractive metals such Hf, Ti and Mo are among the metallic ions that may be considered for improvement of the oxygen sensors performance.

References

- Administration, U.S. Energy Information. 2015. "What Is Energy? Explained."
http://www.eia.gov/energyexplained/index.cfm?page=about_home.
- Aguir, K., C. Lemire, and D. B B Lollman. 2002. "Electrical Properties of Reactively Sputtered WO₃ Thin Films as Ozone Gas Sensor." *Sensors and Actuators, B: Chemical* 84 (1): 1–5.
- Alfonso, E., J. Olaya, and G. Cubillos. 2012. "Thin Film Growth through Sputtering Technique and Its Applications." *Crystallization - Science and Technology*, 397–432.
- Alford, Terry L., Leonard C. Feldman, and James W. Mayer. 2007. *Fundamentals of Nanoscale Film Analysis. PhD Proposal*. Vol. 1. Springer.
- Arregui, Francisco J. 2009. *Sensors Based on Nanostructured Materials*. Edited by Francisco J Arregui. Pamplona, Spain: Springer..
- Auciello, O., and A.R. Krauss. n.d. *In-Situ Real Time Characterization of Thin Films*. New York: John Wiley & Sons Incorporated.
- Australian Microscopy and Microanalysis Research Facility. 2013. "Lay Out."
<http://ammrf.org.au/myscope/sem/practice/principles/layout.php#detail>.
- Australian Microscopy and Microanalysis Research Facility. 2014. "Introduction."
<http://ammrf.org.au/myscope/xrd/introduction/>.
- Azimirad, R, N Naseri, O Akhavan, and A Z Moshfegh. 2007. "Hydrophilicity Variation of WO₃ Thin Films with Annealing Temperature." *Journal of Physics D: Applied Physics* 40 (4). IOP Publishing: 1134–37.
- Baban, C., Y. Toyoda, and M. Ogita. 2005. "Oxygen Sensor Based on Ga₂O₃ Films Operating at High Temperature." *Journal of Optoelectronics and Advanced Materials* 7 (2): 891–96.

- Barsan, Nicolae, and Udo Weimar. 2001. "Conduction Model of Metal Oxide Gas Sensors." *Journal of Electroceramics* 7 (3): 143–67.
- Bartic, M., C. L. Baban, H. Suzuki, M. Ogita, and M. Isai. 2007. "Gallium Oxide as Oxygen Gas Sensors at a High Temperature." *Journal of the American Ceramic Society* 90 (9): 2879–84..
- Bartic, M., M. Ogita, M. Isai, C. L. Baban, and H. Suzuki. 2007. "Oxygen Sensing Properties at High Temperatures of β -Ga₂O₃ Thin Films Deposited by the Chemical Solution Deposition Method." *Journal of Applied Physics* 102 (2): 023709..
- BATHE, S, and P PATIL. 2008. "Titanium Doping Effects in Electrochromic Pulsed Spray Pyrolysed WO₃ Thin Films." *Solid State Ionics* 179 (9-10): 314–23.
- Bene, R, Z Pinte, I V Perczel, M Fleischer, and F Re. 2001. "High-Temperature Semiconductor Gas Sensors." *Vacuum* 61: 275–78.
- Bertus, L. M., C. Faure, A. Danine, C. Labrugere, G. Campet, A. Rougier, and A. Duta. 2013. "Synthesis and Characterization of WO₃ Thin Films by Surfactant Assisted Spray Pyrolysis for Electrochromic Applications." *Materials Chemistry and Physics* 140 (1). Elsevier B.V: 49–59.
- Candel, Â, and Nicolas Docquier. 2002. "Combustion Control and Sensors a Review.pdf" 28.
- Carpenter, Michael A., Sanjay Mathur, and Andrei Kolmakov. 2003. *Metal Oxide Nanomaterials for Chemical Sensors*. New York: Springer.
- Chang, J.F., H.H. Kuo, I.C. Leu, and M.H. Hon. 2002. "The Effects of Thickness and Operation Temperature on ZnO:Al Thin Film CO Gas Sensor." *Sensors and Actuators B: Chemical* 84 (2-3): 258–64.
- Cheng, Yi, Kun Yang, Yong Peng, Yan Yin, Jixiang Chen, Bo Jing, Hongwei Liang, and Guotong Du. 2013. "Research on the Structural and Optical Stability of Ga₂O₃ Films Deposited by Electron Beam

- Evaporation.” *Journal of Materials Science: Materials in Electronics* 24 (12): 5122–26.
- Choi, Kyoung Jin, and Ho Won Jang. 2010. “One-Dimensional Oxide Nanostructures as Gas-Sensing Materials: Review and Issues.” *Sensors* 10 (4): 4083–99.
- Dakhel, A. A. 2012. “Structural, Optical, and Opto-Dielectric Properties of W-Doped Ga₂O₃ Thin Films.” *Journal of Materials Science* 47 (7): 3034–39.
- Dakhel, A. A. 2013. “Investigation of Opto-Dielectric Properties of Ti-Doped Ga₂O₃ Thin Films.” *Solid State Sciences* 20. Elsevier Masson SAS: 54–58.
- Fan, Zhiyong, Dawei Wang, Pai Chun Chang, Wei Yu Tseng, and Jia G. Lu. 2004. “ZnO Nanowire Field-Effect Transistor and Oxygen Sensing Property.” *Applied Physics Letters* 85 (24): 5923–25.
- Feng, P., X. Y. Xue, Y. G. Liu, Q. Wan, and T. H. Wang. 2006. “Achieving Fast Oxygen Response in Individual β -Ga₂O₃ Nanowires by Ultraviolet Illumination.” *Applied Physics Letters* 89 (11): 87–90.
- Fleischer, M, M Seth, C D Kohl, and H Meixner. 1996. “A Study of Surface Modification at Semiconducting Ga₂O₃ Thin Film Sensors for Enhancement of the Sensitivity and Selectivity.” *Sensors and Actuators* 36: 290–96..
- Fleischer, M, V Wagner, B Hacker, and H Meixner. 1995. “Comparison of A.c. and D.c. Measurement Techniques Using Semiconducting Ga₂O₃ Sensors” *Sensors and Actuators B* 26-27 (1995): 85-88
- Fleischer, M., and H. Meixner. 1993. “Electron Mobility in Single- and Polycrystalline Ga₂O₃.” *Journal of Applied Physics* 74 (1): 300–305.
- Fleischer, M., and H. Meixner. 2000. “Gallium Oxide Thin Films: A New Material for High-Temperature.” *Sensors and Actuators B* 4 (1991): 437–41.
- Fleischer, Maximilian. 2008. “Advances in Application Potential of Adsorptive-Type Solid State Gas Sensors: High-Temperature Semiconducting Oxides and Ambient Temperature GasFET Devices.”

Measurement Science and Technology 19 (4): 042001.

Fleischer, Maximilian, Leo Hollbauer, Eberhard Born, and Hans Meixner. 1997. "Evidence for a Phase Transition of Beta-Gallium Oxide at Very Low Oxygen Pressures." *Journal of American Ceramics Society* 80 (8): 2121–25.

Fouletier, J., G. Vitter, and M. Kleitz. 1975. "Measurement and Regulation of Oxygen Content in Gases Using Solid Electrolyte Cells . HL Oxygen Pump- Gauge" 5: 111–20.

Frank, J., M. Fleischer, and H. Meixner. 1996. "Electrical Doping Of Gas Sensitive, Semiconducting Ga₂O₃ Thin Films." *Sensors and Actuators* 34: 373–77.

Frank, J., M. Fleischer, and H. Meixner. 1998. "Gas-Sensitive Electrical Properties of Pure and Doped Semiconducting Ga₂O₃ Thick Films." *Sensors and Actuators B: Chemical* 48 (1-3): 318–21.

Frank, J., M. Fleischer, H. Meixner, and A. Feltz. 1998. "Enhancement of Sensitivity and Conductivity of Semiconducting Ga₂O₃ Gas Sensors by Doping with SnO₂." *Proceedings of International Solid State Sensors and Actuators Conference (Transducers '97)* 49: 110–14.

Fujiwara, H. 2007. *Spectroscopic Ellipsometry: Principles and Applications*. John Wiley & Sons Inc.

Geller, S. 1960. "Crystal Structure of β -Ga₂O₃." *The Journal of Chemical Physics* 33 (3). AIP Publishing: 676.

Gerblinger, J., U. Lampe, and H. Meixner. 1995. "Sensitivity Mechanism of Metal Oxides to Oxygen Detected by Means of Kinetic Studies at High Temperatures." *Sensors and Actuators: B. Chemical* 25 (1-3): 639–42..

Gerblinger, J., U. Lampe, H. Meixner, I.V. Perczel, and J. Giber. 1994. "Cross-Sensitivity of Various Doped Strontium Titanate Films to CO, CO₂, H₂, H₂O and CH₄." *Sensors and Actuators B: Chemical* 19 (1-3): 529–34.

- Gillet, M., C. Lemire, E. Gillet, and K. Aguir. 2003. "The Role of Surface Oxygen Vacancies upon WO₃ Conductivity." *Surface Science* 532-535: 519–25..
- Goyal, Anshu, Brajesh S. Yadav, O.P. Thakur, A.K. Kapoor, and R. Muralidharan. 2014. "Effect of Annealing on β -Ga₂O₃ Film Grown by Pulsed Laser Deposition Technique." *Journal of Alloys and Compounds* 583 (January): 214–19.
- Guide to Using WVASE32 Spectroscopic Ellipsometry Data Acquisition and Analysis Software*. 2008. J. A. Woollam Co., Incorporated.
- Gullapalli, S. K., R. S. Vemuri, and C. V. Ramana. 2010. "Structural Transformation Induced Changes in the Optical Properties of Nanocrystalline Tungsten Oxide Thin Films." *Applied Physics Letters* 96 (17): 1–4.
- Haaland, David M. 1977. "Internal-Reference Solid-Electrolyte Oxygen Sensor." *Analytical Chemistry* 49 (12): 1813–17.
- Han, X, Y Yan, C Cheng, Y Chen, and Y Zhu. 2013. "Monitoring of Oxygen Content in the Flue Gas at a Coal-Fired Power Plant Using Cloud Modeling Techniques." *Instrumentation and Measurement, IEEE Transactions on PP* (99): 1.
- Hao, Jianhua, and Michael Cocivera. 2002. "Optical and Luminescent Properties of Undoped and Rare-Earth-Doped Ga₂O₃ Thin Films Deposited by Spray Pyrolysis." *Journal of Physics D* 35: 433–38.
- Hyodo, Takeo, Norihiro Nishida, Yasuhiro Shimizu, and Makoto Egashira. 2002. "Preparation and Gas-Sensing Properties of Thermally Stable Mesoporous SnO₂." *Sensors and Actuators B: Chemical* 83 (1-3): 209–15..
- International Energy Agency. 2015. "Key World Energy Statistics 2015," 81.
- Izu, N, W Shin, I Matsubara, and N Murayama. 2004. "Kinetic Behavior of Resistive Oxygen Sensor Using

- Cerium Oxide.” *Sensors and Actuators B: Chemical* 100 (3): 411–16.
- Izu, Noriya, Woosuck Shin, Ichiro Matsubara, and Norimitsu Murayama. 2004. “Development of Resistive Oxygen Sensors Based on Cerium Oxide Thick Film.” *Journal of Electroceramics* 13 (1-3): 703–6.
- Janowitz, Christoph, Valentina Scherer, Mansour Mohamed, Alica Krapf, Helmut Dwelk, Recardo Manzke, Zbigniew Galazka, et al. 2011. “Experimental Electronic Structure of In_2O_3 and Ga_2O_3 .” *New Journal of Physics* 13.
- Jasinski, Piotr, Toshio Suzuki, and Harlan U. Anderson. 2003. “Nanocrystalline Undoped Ceria Oxygen Sensor.” *Sensors and Actuators B: Chemical* 95 (1-3): 73–77.
- Josepovits, V.K., O. Krafcsik, G. Kiss, and I.V. Perczel. 1998. “Effect of Gas Adsorption on the Surface Structure of $\beta\text{-Ga}_2\text{O}_3$ Studied by XPS and Conductivity Measurements.” *Sensors and Actuators B: Chemical* 48 (1-3): 373–75.
- Kaneko, Hiroyuki, Takayuki Okamura, Hitoshi Taimatsu, Yukio Matsuki, and Hiroshi Nishida. 2005. “Performance of a Miniature Zirconia Oxygen Sensor with a Pd–PdO Internal Reference.” *Sensors and Actuators B: Chemical* 108 (1-2): 331–34..
- Kärger, Jörg, Douglas M. Ruthven, and Doros N. Theodorou. 2012. *Diffusion in Nanoporous Materials*. *Diffusion in Nanoporous Materials*.
- Khoshman, J. M., A. Khan, and M. E. Kordesch. 2008. “Amorphous Hafnium Oxide Thin Films for Antireflection Optical Coatings.” *Surface and Coatings Technology* 202 (11): 2500–2502.
- Khyzhun, O. Yu. 2000. “XPS, XES and XAS Studies of the Electronic Structure of Tungsten Oxides.” *Journal of Alloys and Compounds* 305 (1-2): 1–6.
- Kim, Il Doo, Avner Rothschild, and Harry L. Tuller. 2013. “Advances and New Directions in Gas-Sensing Devices.” *Acta Materialia* 61 (3). Acta Materialia Inc.: 974–1000.

- Kiss, G, K Kovacs, I V Perczel, V K Josepovits, M Fleischer, H Meixner, and F Reti. 2000. "Impedance Spectroscopic Studies of the Electric Conduction in Polycrystalline Beta-Ga₂O₃." *Journal of The Electrochemical Society* 147 (7): 2644–46.
- Kiss, G., I.V. Perczel, M. Fleischer, F Reti, H. Meixner, and J. Giber. 1999. "Impedance Spectroscopic Study of β -Ga₂O₃/O₂ Interaction." *Journal of The Electrochemical Society* 146 (6): 2357–59.
- Kolmakov, Andrei, Youxiang Zhang, Guosheng Cheng, and Martin Moskovits. 2003. "Detection of CO and O₂ Using Tin Oxide Nanowire Sensors." *Advanced Materials* 15 (12): 997–1000.
- Korotcenkov, G. 2007. "Metal Oxides for Solid-State Gas Sensors: What Determines Our Choice?" *Materials Science and Engineering B: Solid-State Materials for Advanced Technology* 139 (1): 1–23..
- Korotcenkov, G., and B. K. Cho. 2011. "Instability of Metal Oxide-Based Conductometric Gas Sensors and Approaches to Stability Improvement (Short Survey)." *Sensors and Actuators, B: Chemical* 156 (2). Elsevier B.V.: 527–538.
- Kumar, S. Sampath, E.J. Rubio, M. Noor-A-Alam, G. Martinez, S. Manandhar, V. Shutthanandan, S. Thevuthasan, and C.V. Ramana. 2013. "Structure, Morphology, and Optical Properties of Amorphous and Nanocrystalline Gallium Oxide Thin Films." *The Journal of Physical Chemistry C* 117 (8): 4194–4200.
- Lassner, Erik, and Wolf-Dieter Schubert. 1999. *Tungsten*. Boston, MA: Springer US.
- Lemire, Céline, Dave B.B. Lollman, Ahmad Al Mohammad, Eveline Gillet, and Khalifa Aguir. 2002. "Reactive R.F. Magnetron Sputtering Deposition of WO₃ Thin Films." *Sensors and Actuators B: Chemical* 84 (1): 43–48.
- Li, Huihua, Fanli Meng, Jinyun Liu, Yufeng Sun, Zhen Jin, Lingtao Kong, Yanjiao Hu, and Jinhuai Liu. 2012. "Synthesis and Gas Sensing Properties of Hierarchical Meso-Macroporous SnO₂ for Detection

- of Indoor Air Pollutants.” *Sensors and Actuators B: Chemical* 166-167 (May): 519–525.
- Li, Q. H., Y. X. Liang, Q. Wan, and T. H. Wang. 2004. “Oxygen Sensing Characteristics of Individual ZnO Nanowire Transistors.” *Applied Physics Letters* 85 (26): 6389–91.
- Li, Yongxiang, Adrian Trinchì, Wojtek Wlodarski, Kosmas Galatsis, and Kourosh Kalantar-Zadeh. 2003. “Investigation of the Oxygen Gas Sensing Performance of Ga₂O₃ Thin Films with Different Dopants.” *Sensors and Actuators, B: Chemical* 93 (1-3): 431–34.
- Litimein, F., D. Rached, R. Khenata, and H. Baltache. 2009. “FPLAPW Study of the Structural, Electronic, and Optical Properties of Ga₂O₃: Monoclinic and Hexagonal Phases.” *Journal of Alloys and Compounds* 488 (1): 148–56.
- Liu, X. Z., P. Guo, T. Sheng, L. X. Qian, W. L. Zhang, and Y. R. Li. 2016. “β-Ga₂O₃ Thin Films on Sapphire Pre-Seeded by Homo-Self-Templated Buffer Layer for Solar-Blind UV Photodetector.” *Optical Materials* 51: 203–7.
- Liu, Y X, J Parisi, X C Sun, and Y Lei. 2014. “Solid-State Gas Sensors for High Temperature Applications - a Review.” *Journal of Materials Chemistry A* 2 (26): 9919–43.
- Liu, Zhifu, Toshinari Yamazaki, Yanbai Shen, Toshio Kikuta, Noriyuki Nakatani, and Yongxiang Li. 2008. “O₂ and CO Sensing of Ga₂O₃ Multiple Nanowire Gas Sensors.” *Sensors and Actuators, B: Chemical* 129 (2): 666–70.
- Long-Tsong Ju. 2011. “Enhanced Oxygen Gas Sensor by Surface-Etched Gallium Oxide.” *International Journal of the Physical Sciences* 6 (30): 7016–20.
- López, I, A Castaldini, A Cavallini, E Nogales, B Méndez, and J Piqueras. 2014. “β -Ga₂O₃ Nanowires for an Ultraviolet Light Selective Frequency Photodetector.” *Journal of Physics D: Applied Physics* 47 (41): 415101.

Louisville, University of. n.d. “RCA-1 and RCA-2 Wafer Clean.”
<https://louisville.edu/conference/ugim2008/cleanroom/sops/sops/rca-1-and-rca-2-wafer-clean/rca-1-and-rca-2-wafer-clean.html>.

Lovejoy, T C, Renyu Chen, E N Yitamben, V Shutthanadan, S M Heald, E G Villora, K Shimamura, S Zheng, S T Dunham, and F S Ohuchi. 2012. “Incorporation , Valence State , and Electronic Structure of Mn and Cr in Bulk Single Crystal β – Ga_2O_3 .” *Journal of Applied Physics* 111: 1–10.

Lovejoy, T. C., Renyu Chen, E. N. Yitamben, V. Shutthanadan, S. M. Heald, E. G. Villora, K. Shimamura, S. Zheng, S. T. Dunham, F. S. Ohuchi, et al. 2012. “Incorporation, Valence State, and Electronic Structure of Mn and Cr in Bulk Single Crystal β – Ga_2O_3 .” *Journal of Applied Physics* 111 (12). AIP Publishing: 123716.

Lovejoy, T. C., Renyu Chen, X. Zheng, E. G. Villora, K. Shimamura, H. Yoshikawa, Y. Yamashita, et al. 2012. “Band Bending and Surface Defects in β - Ga_2O_3 .” *Applied Physics Letters* 100 (18): 181602.

Maskell, W. 2000. “Progress in the Development of Zirconia Gas Sensors.” *Solid State Ionics* 134 (1-2): 43–50.

Mayer, M. 1999. “SIMNRA, a Simulation Program for the Analysis of NRA, RBS and ERDA.” *AIP Conference Proceedings* 475: 541–44.

Mayer, Matej, and Matej Mayer. 1997. “SIMNRA User ’ S Guide.”

Menesklou, Wolfgang, Hans-Jürgen Schreiner, Karl Heinz Härdtl, and Ellen Ivers-Tiffée. 1999. “High Temperature Oxygen Sensors Based on Doped SrTiO_3 .” *Sensors and Actuators B: Chemical* 59 (2–3): 184–89.

Mi, Wei, Caina Luan, Zhao Li, Cansong Zhao, Xianjin Feng, and Jin Ma. 2013. “Ultraviolet-Green Photoluminescence of β - Ga_2O_3 Films Deposited on MgAl_2O_4 (1 0 0) Substrate.” *Optical Materials*

35 (12). Elsevier B.V.: 2624–28..

- Mi, Wei, Jin Ma, Caina Luan, and Hongdi Xiao. 2014. “Structural and Optical Properties of β -Ga₂O₃ Films Deposited on MgAl₂O₄ (100) Substrates by Metal–organic Chemical Vapor Deposition.” *Journal of Luminescence* 146. Elsevier: 1–5. doi:10.1016/j.jlumin.2013.09.056.
- Millner, T., and J. Neugebauer. 1949. “Volatility of the Oxides of Tungsten and Molybdenum in the Presence of Water Vapour.” *Nature* 163: 601–2.
- Mudavakkat, V.H., V.V. Atuchin, V.N. Kruchinin, A. Kayani, and C.V. Ramana. 2012. “Structure, Morphology and Optical Properties of Nanocrystalline Yttrium Oxide (Y₂O₃) Thin Films.” *Optical Materials* 34 (5): 893–900.
- Müller, Stefan, Holger von Wenckstern, Daniel Splith, Florian Schmidt, and Marius Grundmann. 2014. “Control of the Conductivity of Si-Doped β -Ga₂O₃ Thin Films via Growth Temperature and Pressure.” *Physica Status Solidi (a)* 211 (1): 34–39.
- Naseri, N, R Azimirad, O Akhavan, and A Z Moshfegh. 2007. “The Effect of Nanocrystalline Tungsten Oxide Concentration on Surface Properties of Dip-Coated Hydrophilic WO₃ –SiO₂ Thin Films.” *Journal of Physics D: Applied Physics* 40 (7). IOP Publishing: 2089–95.
- Ogita, M., K. Higo, Y. Nakanishi, and Y. Hatanaka. 2001. “Ga₂O₃ Thin Film for Oxygen Sensor at High Temperature.” *Applied Surface Science* 175-176: 721–25.
- Oliver, W.C., and G.M. Pharr. 1992. “An Improved Technique for Determining Hardness and Elastic Modulus Using Load and Displacement Sensing Indentation Experiments.” *Journal of Materials Research* 7 (06): 1564–1583.
- Onuma, T., S. Fujioka, T. Yamaguchi, M. Higashiwaki, K. Sasaki, T. Masui, and T. Honda. 2013. “Correlation between Blue Luminescence Intensity and Resistivity in β -Ga₂O₃ Single Crystals.”

Applied Physics Letters 103 (4): 3–6.

Pavageau, Marie Pierre, Christophe P??cheyran, Eva M. Krupp, Anne Morin, and Olivier F X Donard.

2002. “Volatile Metal Species in Coal Combustion Flue Gas.” *Environmental Science and Technology* 36 (7): 1561–1573.

Petitmangin, A., B. Gallas, C. Hebert, J. Perri??re, L. Binet, P. Barboux, and X. Portier. 2013.

“Characterization of Oxygen Deficient Gallium Oxide Films Grown by PLD.” *Applied Surface Science* 278. Elsevier B.V.: 153–157.

Pharr, G.M., W.C. Oliver, and F.R. Brotzen. 1992. “On the Generality of the Relationship among Contact

Stiffness, Contact Area, and Elastic Modulus during Indentation.” *Journal of Materials Research* 7 (03): 613–17.

Ramamoorthy, R, P K Dutta, and S a Akbar. 2003. “Oxygen Sensors : Materials , Methods , Designs.” *J.*

Mater. Sci. 38: 4271–82..

Ramamoorthy, R., S. Ramasamy, and D. Sundararaman. 1999. “Annealing Effects on Phase

Transformation and Powder Microstructure of Nanocrystalline Zirconia Polymorphs.” *Journal of Materials Research* 14: 90–96.

Ramana, C. V., E. J. Rubio, C. D. Barraza, A. Miranda Gallardo, Samantha McPeak, Sushma Kotru, and J.

T. Grant. 2014a. “Chemical Bonding, Optical Constants, and Electrical Resistivity of Sputter-Deposited Gallium Oxide Thin Films.” *Journal of Applied Physics* 115 (4).

Ramana, C. V., R. J. Smith, O. M. Hussain, C. C. Chusuei, and C. M. Julien. 2005. “Correlation between

Growth Conditions, Microstructure, and Optical Properties in Pulsed-Laser-Deposited V₂O₅ Thin Films.” *Chemistry of Materials* 17 (5). American Chemical Society: 1213–19.

Rebien, M., W. Henrion, M. Hong, J. P. Mannaerts, and M. Fleischer. 2002. “Optical Properties of Gallium

- Oxide Thin Films.” *Applied Physics Letters* 81 (2): 250–52.
- Reti, F. 2001. “Impedance Spectroscopic β -Ga₂O₃/O₂ Interaction” 146 (6): 239–42.
- Rettig, Frank, Ralf Moos, and Carsten Plog. 2004. “Poisoning of Temperature Independent Resistive Oxygen Sensors by Sulfur Dioxide.” *Journal of Electroceramics* 13 (1-3): 733–38.
- Riech, I., M. Acosta, J. L. Peña, and P. Bartolo-Pérez. 2010. “Effects of Working Pressure on Physical Properties of Tungsten-Oxide Thin Films Sputtered from Oxide Target.” *Journal of Vacuum Science & Technology A: Vacuum, Surfaces, and Films* 28 (2). AVS: Science & Technology of Materials, Interfaces, and Processing: 329.
- Romanosky, Robert R., Richard J. Dunst, and Prabir K. Dutta. 2008. “High-Temperature Ceramic Microsensor Development for Combustion Boiler Optimization.”
- Romanosky, Robert R., and Susan M. Maley. 2013. “Harsh Environment Sensor Development for Advanced Energy Systems” 8725: 87250H..
- Roque-Malherbe, Rolando. 2007. *Adsorption and Diffusion in Nanoporous Materials*.
- Rothschild, Avner, Scott J. Litzelman, Harry L. Tuller, Wolfgang Menesklou, Thomas Schneider, and Ellen Ivers-Tiffée. 2005. “Temperature-Independent Resistive Oxygen Sensors Based on SrTi_{1-x}FexO_{3-δ} Solid Solutions.” *Sensors and Actuators B: Chemical* 108 (1-2): 223–30.
- Roy, Rustum, V G Hill, and E F Osborn. 1952. “Polymorphism of Ga₂O₃ and the System Ga₂O₃-H₂O.” *J. Amer. Chem. Soc.* 74 (7): 719–22.
- Rubio, E. J., and C. V. Ramana. 2013a. “Tungsten-Incorporation Induced Red-Shift in the Bandgap of Gallium Oxide Thin Films.” *Applied Physics Letters* 102 (19).
- Sakai, Go, Naoki Matsunaga, Kengo Shimanoe, and Noboru Yamazoe. 2001. “Theory of Gas-Diffusion Controlled Sensitivity for Thin Film Semiconductor Gas Sensor.” *Sensors and Actuators B: Chemical*

80: 125–31.

- Sasaki, Kohei, Akito Kuramata, Takekazu Masui, Encarnación G. Vllora, Kiyoshi Shimamura, Shigenobu Yamakoshi, and E G Villora. 2012. “Device-Quality β -Ga₂O₃ Epitaxial Films Fabricated by Ozone Molecular Beam Epitaxy.” *Applied Physics Express* 5 (3): 035502.
- Sato, Taichi, and Takato Nakamura. 1982. “Thermal Decomposition of Gallium Hydroxides.” *Thermochimica Acta* 53 (3): 281–88.
- Schubert, M., R. Korlacki, S. Knight, T. Hofmann, S. Schöche, V. Darakchieva, E. Janzén, et al. 2015. “Anisotropy, Phonon Modes, and Free Charge Carrier Parameters in Monoclinic β -Gallium Oxide Single Crystals,” 1–18.
- Schwebel, T., M. Fleischer, and H. Meixner. 2000. “Selective, Temperature Compensated O₂ Sensor Based on Ga₂O₃ Thin Films.” *Sensors and Actuators, B: Chemical* 65 (1): 176–80.
- Schwenke, G.K. 2001. “THERMODYNAMICS OF THE HYDROGEN-CARBON-OXYGEN-TUNGSTEN SYSTEM, AS APPLIED TO THE MANUFACTURE OF TUNGSTEN AND TUNGSTEN CARBIDE.” *15th International Plansee Seminar, Eds. G. Kneringer, P. Rodhammer and H. Wildner, Plansee Holding AG, Reutte* 2: 647–61.
- Shan, F. K., G. X. Liu, W. J. Lee, G. H. Lee, I. S. Kim, and B. C. Shin. 2005. “Structural, Electrical, and Optical Properties of Transparent Gallium Oxide Thin Films Grown by Plasma-Enhanced Atomic Layer Deposition.” *Journal of Applied Physics* 98 (2).
- Sharma, Rajnish K, Philip C H Chan, Zhenan Tang, Guizhen Yan, I-ming Hsing, and Johnny K O Sin. 2001. “Investigation of Stability and Reliability of Tin Oxide Thin-film for Integrated Micro-Machined Gas Sensor Devices” 81: 9–16.
- Shim, Hee-Sang, Jeong Won Kim, Yung-Eun Sung, and Won Bae Kim. 2009. “Electrochromic Properties

- of Tungsten Oxide Nanowires Fabricated by Electrospinning Method.” *Solar Energy Materials and Solar Cells* 93 (12): 2062–68. doi:10.1016/j.solmat.2009.02.008.
- Sinha, G., K. Adhikary, and S. Chaudhuri. 2005. “Sol-Gel Derived Phase Pure α -Ga₂O₃ Nanocrystalline Thin Film and Its Optical Properties.” *Journal of Crystal Growth* 276 (1-2): 204–7.
- Spirig, John V., Ramasamy Ramamoorthy, Sheikh A. Akbar, Jules L. Routbort, Dileep Singh, and Prabir K. Dutta. 2007. “High Temperature Zirconia Oxygen Sensor with Sealed Metal/metal Oxide Internal Reference.” *Sensors and Actuators, B: Chemical* 124 (1): 192–201.
- Srinivasan, Anandan, and Masahiro Miyauchi. 2012. “Chemically Stable WO₃ Based Thin-Film for Visible-Light Induced Oxidation and Superhydrophilicity.” *The Journal of Physical Chemistry C* 116 (29). American Chemical Society: 15421–26.
- Suzuki, N., S. Ohira, M. Tanaka, T. Sugawara, K. Nakajima, and T. Shishido. 2007. “Fabrication and Characterization of Transparent Conductive Sn-Doped β -Ga₂O₃ Single Crystal.” *Physica Status Solidi (C) Current Topics in Solid State Physics* 4 (7): 2310–13.
- Thornton, John A. 1974. “Influence of Apparatus Geometry and Deposition Conditions on the Structure and Topography of Thick Sputtered Coatings.” *Journal of Vacuum Science and Technology* 11 (4): 666.
- Tiwari, Atul. 2012. “Nanomechanical Analysis of Hybrid Silicones and Hybrid Epoxy Coatings—A Brief Review.” *Advances in Chemical Engineering and Science* 02 (01): 34–44.
- Trinchi, A., S. Kaciulis, L. Pandolfi, M.K. Ghantasala, Y.X. Li, W. Wlodarski, S. Viticoli, E. Comini, and G. Sberveglieri. 2004. “Characterization of Ga₂O₃ Based MRISiC Hydrogen Gas Sensors.” *Sensors and Actuators B: Chemical* 103 (1-2): 129–35.
- Tsai, Min-Ying, Oliver Bierwagen, Mark E. White, and James S. Speck. 2010. “ β -Ga₂O₃ Growth by

- Plasma-Assisted Molecular Beam Epitaxy.” *Journal of Vacuum Science & Technology A: Vacuum, Surfaces, and Films* 28 (2): 354.
- Umar, Ahmad, Lewis Way, Albert Taranam, Emma Rossinyol, and Miguel Angel Juli. 2010. *Metal Oxide Nanostructures and Their Applications*. Vol. 3.
- Usui, Toshio. 1989. “Gas Polarographic Oxygen Sensor Using an Oxygen/Zirconia Electrolyte.” *J. Electrochem. Soc.* 136 (2): 534.
- Usui, Toshio, Kenji Nuri, Mitsuhiro Nakazawa, and Hiroshi Osanai. 1987. “Output Characteristics of a Gas-Polarographic Oxygen Sensor Using a Zirconia Electrolyte in the Knudsen Diffusion Region.” *Japanese Journal of Applied Physics* 26: L2061–64.
- Van Setten, E., T. M. Gür, D. H A Blank, J. C. Bravman, and M. R. Beasley. 2002. “Miniature Nernstian Oxygen Sensor for Deposition and Growth Environments.” *Review of Scientific Instruments* 73 (1): 156.
- Vargas, M., E. J. Rubio, A. Gutierrez, and C. V. Ramana. 2014. “Spectroscopic Ellipsometry Determination of the Optical Constants of Titanium-Doped WO₃ Films Made by Co-Sputter Deposition.” *Journal of Applied Physics* 115 (13).
- Varhegyi, E. B., I. V. Perczel, J. Gerblinger, M. Fleischer, H. Meixner, and J. Giber. 1994. “Auger and SIMS Study of Segregation and Corrosion Behaviour of Some Semiconducting Oxide Gas-Sensor Materials.” *Sensors and Actuators: B. Chemical* 19 (1-3): 569–72.
- Varley, J. B., J. R. Weber, a. Janotti, and C. G. Van de Walle. 2010. “Oxygen Vacancies and Donor Impurities in β -Ga₂O₃.” *Applied Physics Letters* 97 (14): 142106.
- Vemuri, R S, M H Engelhard, and C V Ramana. 2012. “Correlation between Surface Chemistry, Density, and Band Gap in Nanocrystalline WO₃ Thin Films.” *ACS Applied Materials & Interfaces* 4 (3).

American Chemical Society: 1371–77.

Villora, Encarnación G., Kiyoshi Shimamura, Yukio Yoshikawa, Takekazu Ujiie, and Kazuo Aoki. 2008.

“Electrical Conductivity and Carrier Concentration Control in β -Ga₂O₃ by Si Doping.” *Applied Physics Letters* 92 (20): 29–32.

Wagner, Th., J. Hennemann, C.-D. Kohl, and M. Tiemann. 2011. “Photocatalytic Ozone Sensor Based on

Mesoporous Indium Oxide: Influence of the Relative Humidity on the Sensing Performance.” *Thin Solid Films* 520 (3): 918–21.

Wagner, Thorsten, Stefanie Haffer, Christian Weinberger, Dominik Klaus, and Michael Tiemann. 2013.

“Mesoporous Materials as Gas Sensors.” *Chemical Society Review* 42: 4036–53.

Wang, Chengxiang, Longwei Yin, Luyuan Zhang, Dong Xiang, and Rui Gao. 2010. “Metal Oxide Gas

Sensors: Sensitivity and Influencing Factors.” *Sensors* 10 (3): 2088–2106.

Wasa, Kiyotaka, Makoto Kitabatake, and Hideaki Adachi. 2004. *Thin Film Materials Technology;*

Sputtering of Compound Materials. Sci-Tech News. Vol. 58. Norwich, NY: William Andrew. Xu, Yulong, Xiaohua Zhou, and O Toft Sorensen. 2000. “Oxygen Sensors Based on Semiconducting Metal Oxides - An Overview.pdf,” 4–6.

Yamaga, Mitsuo, Encarnación G. Villora, Kiyoshi Shimamura, Noboru Ichinose, and Makoto Honda. 2003.

“Donor Structure and Electric Transport Mechanism in β - Ga₂O₃.” *Physical Review B* 68 (15). American Physical Society: 155207.

Yamazoe, Noboru. 2005. “Toward Innovations of Gas Sensor Technology.” *Sensors and Actuators, B:*

Chemical 108 (1-2 SPEC. ISS.): 2–14.

Yokogawa. 2008. “Carbon Monoxide Measurement in Coal-Fired Power Boilers.”

Yoshioka, S, H Hayashi, A Kuwabara, F Oba, K Matsunaga, and I Tanaka. 2007. “Structures and Energetics

- of Ga₂O₃ Polymorphs.” *J. Phys.: Condens. Matter* 19 (19): 346211–11.
- Zhang, Yijun, Jinliang Yan, Qingshan Li, Chong Qu, Liying Zhang, and Wanfeng Xie. 2011a. “Optical and Structural Properties of Cu-Doped β -Ga₂O₃ Films.” *Materials Science and Engineering: B* 176 (11). Elsevier B.V.: 846–49.
- Zhang, Yuzhi, Jiaguo Yuan, Jun Le, Lixin Song, and Xingfang Hu. 2009. “Structural and Electrochromic Properties of Tungsten Oxide Prepared by Surfactant-Assisted Process.” *Solar Energy Materials and Solar Cells* 93 (8). Elsevier: 1338–44.
- Zhang, Z. Y., C. H. Jin, X. L. Liang, Q. Chen, and L. M. Peng. 2006. “Current-Voltage Characteristics and Parameter Retrieval of Semiconducting Nanowires.” *Applied Physics Letters* 88 (7): 2004–7..
- Zhuykov, Serge. 2006. ““ In Situ ’ Diagnostics of Solid Electrolyte Sensors Measuring Oxygen Activity in Melts by a Developed Impedance Method.” *Measurement Science and Technology* 17 (6): 1570–78.
- Zinkevich, Matvei, and Fritz Aldinger. 2001. “Thermodynamic Assessment of the Gallium-Oxygen System.” *Journal of the American Ceramic Society* 87 (4): 683–691.

Curriculum Vitae

Ernesto Javier Rubio was born on August 22th, 1988 in Ciudad Juárez, Chihuahua, México. The first son of David Rubio and Sylvia Islava, he graduated from University of Texas at El Paso with a bachelor's degree in Mechanical Engineering. He stayed at University of Texas at El Paso to pursue his master's degree in Mechanical Engineering. During his master's, he worked as a teaching assistant and research assistant in the department of mechanical engineering. He is a member of the cSETR center in the department of Mechanical Engineering. In fall 2012, he graduated with a Master of Science degree in Mechanical Engineering and proceeded further to pursue his Ph.D in the ESE program at UTEP which he joined in spring 2013. He continued working as a research assistant under Dr. Ramana Chintalapalle mentoring. From July 2015 to January 2016 he joined Bombardier Recreational Products as a laboratories supervisor while continuing pursuing his doctoral degree.

Permanent address: Ignacio Mejía 2028,
Colonia Partido Romero
Ciudad Juárez, Chihuahua,
México, 32320

Contact Information: ejrubio@miners.utep.edu

This thesis/dissertation was typed by Ernesto Javier Rubio